Scholars' Mine

Spring 2016

Application of embedded frequency selective surfaces for structural health monitoring

Dustin Franklin Pieper

Follow this and additional works at: https://scholarsmine.mst.edu/masters_theses

Part of the Electromagnetics and Photonics Commons

Department:

Recommended Citation

APPLICATION OF EMBEDDED FREQUENCY SELECTIVE SURFACES FOR

STRUCTURAL HEALTH MONITORING

by

DUSTIN FRANKLIN PIEPER

A THESIS

Presented to the Faculty of the Graduate School of the

MISSOURI UNIVERSITY OF SCIENCE AND TECHNOLOGY

In Partial Fulfillment of the Requirements for the Degree

MASTER OF SCIENCE IN ELECTRICAL ENGINEERING

2016

Approved by

Kristen M. Donnell, Advisor
Reza Zoughi
Ed Kinzel

ABSTRACT

This thesis proposes the use of Frequency Selective Surfaces (FSSs) as an embedded structural health monitoring (SHM) sensor. FSSs are periodic arrays of conductive elements that filter certain frequencies of incident electromagnetic radiation. The behavior of this filter is heavily dependent on the geometry of the FSS and local environment. Therefore, by monitoring how this filtering response changes when the geometric or environmental changes take place, information about those changes may be determined. In previous works, FSS-based sensing has shown promise for sensing normal strain (a stretching or compressing geometrical deformation). This concept is extended in this thesis by investigating the potential of FSSs for sensing shear strain (a twisting deformation) and detection of delamination/disbond (defined as an air gap that develops due a separation between layered dielectrics, and herein referred to as delamination) in layered structures. For normal strain and delamination sensing, monitoring of the FSS's resonant frequency is shown to be a reliable indicator for each phenomena, as verified by full-wave simulation and measurement. For shear strain, simulation results indicate that an FSS may cross-polarize incident radiation when under shear strain. Additionally, FSS was applied as a normal and shear strain sensor within a steel-tube reinforced concrete column, where it was found to provide reliable normal strain detection (as compared to traditional strain sensors), but was not able to detect shear strain. Lastly, in order to improve the design procedure by reducing computation time, an algorithm was developed that rapidly approximates the response of an FSS to delamination through use of conformal mapping and existing frequency response calculations.

ACKNOWLEDGMENTS

TABLE OF CONTENTS

LIST OF ILLUSTRATIONS

LIST OF TABLES

1. INTRODUCTION

1.1. BACKGROUND AND RESEARCH MOTIVATION

A major area of interdisciplinary research focuses on the development of infrastructure than can provide information on its structural integrity, allowing for easier inspection and testing [51]. As such, structural health monitoring (SHM) sensors that can be embedded into and integrated throughout a structure are necessary. Currently, fiber optic sensors are one of the most common embedded SHM sensors, and can sense phenomena such as temperature and normal strain [52]. Other potential sensor technologies involve the use of piezoelectric materials or acoustical nanowire sensors that can be directly integrated into a structure [51], [52]. As an addition to the currently available sensors, this thesis proposes the use of Frequency Selective Surfaces (FSS) as a form of embedded SHM sensors.

In its most basic form, an FSS is a periodic array of conductive elements designed to resonate at a certain frequency. At this resonant frequency, the FSS acts as either a band-pass or a band-stop filter to incident electromagnetic radiation [1]. This filtering behavior occurs due to inductive (L) and capacitive (C) coupling between the elements of the FSS (and hence the FSS acts as an LC filter). This coupling, and thus the filtering behavior of the FSS (referred to as the frequency response), is highly dependent on geometry and local environment. As such, an FSS's frequency response is determined by the dimensions and spacing of the FSS elements, as well as the presence of nearby dielectrics and conductors. This thesis proposes that an FSS's dependence on geometry and environment can be useful for SHM purposes. Previously, [33] and [34] have found that an FSS can be used to sense normal strain (a stretching or compressing deformation) [39]. The use of an FSS for sensing normal strain is extended in this work by examining the sensitivity of different FSS elements to normal strain, as well as measurement verification of FSS's sensitivity to normal strain. Additionally, sensing capabilities are explored for shear strain (defined as a twisting deformation [36]) and delamination/disbond (defined as a separation of bonded or laminated materials within a structure [43] and herein referred to as delamination) detection.

1.2. SUMMARY OF SECTIONS

Section 2 of this thesis introduces the theory and background of FSS operation and design. A brief history of the development and research of FSS design is presented in Section 2.1. Section 2.2 presents the fundamental theory of FSS operation, including analysis of frequency response for various FSS elements and general design practices. Additionally, a variety of common FSS elements used throughout this thesis are presented and discussed. Next, Section 2.3 presents a range of more advanced FSS topics that pertain to practical implementation, including the effects of local dielectrics and conductors, oblique incidence of impinging radiation, and sensing using multiple FSS layers within a single structure.

In Section 3, the use of FSSs for sensing normal and shear strain is examined. In Section 3.1, the effects of normal strain on an FSS's frequency response are investigated. FSSs have previously been found to have potential as a normal strain sensor because an FSS's resonant frequency is a function of its geometry (conductor length, width, etc.) [33], [34]. As such, an FSS's resonant frequency will shift when its conductors are stretched or compressed, as is the case when an FSS is under normal strain. By monitoring changes in the resonant frequency, the normal strain (experienced by the FSS) can be determined. In this investigation, the response of FSS to normal strain is investigated for a variety of FSS elements through full-wave electromagnetic simulation and measurements. Next, in Section 3.2, the effects of shear strain on the FSS's frequency response are studied through full-wave simulation for a series of common FSS elements. These investigations are extended to a practical sensing application in Section 3.3, where the use of FSS as a normal and shear strain sensor is tested in a steel-core reinforced concrete column.

Next, in Section 4, the use of an FSS for delamination detection in a layered dielectric structure is explored. Section 4.1 discusses the effect of local dielectrics on an FSS's frequency response, as well as how a delamination in these dielectrics alters that response. This is examined through a series of simulations and measurements that demonstrate the use of FSSs for delamination sensing. Meanwhile, Section 4.2 presents an analytical approximation method that uses conformal mapping to determine the effective permittivity ($\varepsilon_{r,eff}$) observed by an FSS when embedded within a dielectric

structure. The value of $\varepsilon_{r,eff}$ can be used to relate changes in an FSS's resonant frequency to changes in the surrounding dielectric environment, such as delamination. This approach for determining $\varepsilon_{r,eff}$ is subsequently applied to an algorithm for approximating the frequency response of an FSS when embedded within a layered dielectric structure. Determining $\varepsilon_{r,eff}$ in this way reduces computation time (as compared to full-wave simulation), allowing for expedited analysis of an FSS's response to delamination. Additionally, this can aid the FSS design process by approximating how an FSS's frequency response will be altered when embedded into a dielectric structure.

Finally, Section 5.1 summarizes the work presented in this thesis. Furthermore, Section 5.2 outlines a number of possible extensions of this work. Such extensions include the development of an FSS design methodology for creation of improved FSS SHM sensors, along with the potential of active FSS and optical-wavelength FSS for SHM sensing.

2. AN OVERVIEW OF FSS

This section provides an overview on the background and physical operation of FSSs. To start, a short historical account of FSSs is presented. Then, an in-depth discussion on the functionality and physics inherent to FSSs is provided. This discussion includes a comparison of different FSS element geometries that are relevant to this thesis. Lastly, problems and limitations encountered in real-world application of FSSs are discussed.

2.1. A BRIEF FSS HISTORY

The defining feature of an FSS is its ability to act as a surface with band pass/band stop filtering properties to incident radiation. This is accomplished through a periodic array of conductive elements that inductively and capacitively couple when excited by incident electromagnetic radiation (e.g., a plane wave, a propagating wave with electric and magnetic fields that are orthogonal to each other and the direction of propagation). One of the earliest forms of an FSS was a parabolic reflector grid using an array of resonant dipoles that was designed and patented by Marconi and Franklin in 1919 [1]. However, much of the research into what is now referred to as FSSs didn't gain momentum until the 1960s and 1970s. During this time, the United States Air Force supported classified investigations into FSS development for radar and stealth applications [1], [2]. This research included conductive elements, such as crossed-dipoles and tripoles, which had greater versatility than the single resonant dipoles investigated previously. These new FSS element designs provided better performance including insensitivity to angle of incidence (defined as the angle between a plane wave's direction of propagation and the direction normal to the plane of the FSS) and finer tunability, making FSSs useful for stealth radomes and as multi-band Cassegrain reflector dishes in antenna systems [1], [3]. After becoming declassified in the mid-1970s, research moved towards new methods of FSS design and development for general use. Analysis techniques such as computational modal analysis of resonating elements and circuit model approximations of filter behavior led to a better understanding of the physical characteristics of FSSs [3], [4]. In the 1990s and 2000s, improvements to

computing technology led to the use of numerical solvers, allowing for analysis of more complicated structures that cannot be easily described through analytical means. Today, this work has led to many different FSS designs and applications, including three-dimensional FSS structures [5], active FSS [6], thin-film high-impedance surface absorbers [7], and fractal element FSS designs [8].

2.2. BASIC FSS DESIGN AND ANALYSIS

As stated, the most common form of an FSS is that of a periodic array of conductive elements. Other forms of FSSs include three-dimensional conductive patterns and dielectric-based FSSs (both of which are beyond the scope of this thesis). A number of popular FSS elements, such as dipoles, crosses, loops, and patches, are illustrated in Figure 2.1.
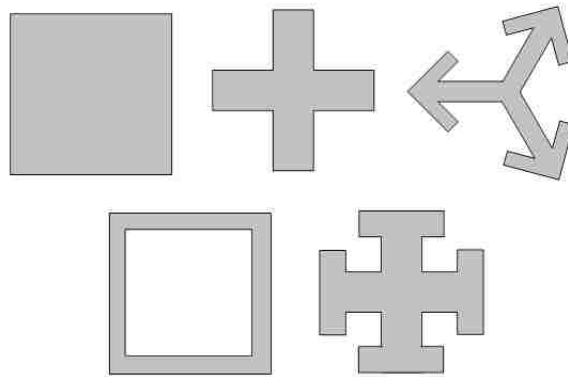
Figure 2.1. Illustration of common FSS elements.

The frequency response of these elements to incident radiation is commonly modeled by an equivalent LC circuit model that corresponds to the mutual inductive and capacitive coupling that occurs between each element [3]. In this way, the FSS can be considered as a frequency dependent impedance. Based on transmission line theory, the impedance mismatch between the FSS LC circuit and surrounding material(s) creates

reflections and transmissions at the FSS interface. The net effect of these reflections and transmissions creates the desired filtering response. Common FSS element designs tend to fall into one or more of three types, described as dipole, loop, or patch type FSSs, or hybridized combinations of the three [1]. Element designs used over the course of this thesis, as well as their accompanying circuit models, are discussed next.

2.2.1. Dipole-Type FSS Elements. The simplest form of an FSS is that of the dipole array, as shown in Figure 2.2, as well as its associated equivalent LC circuit.
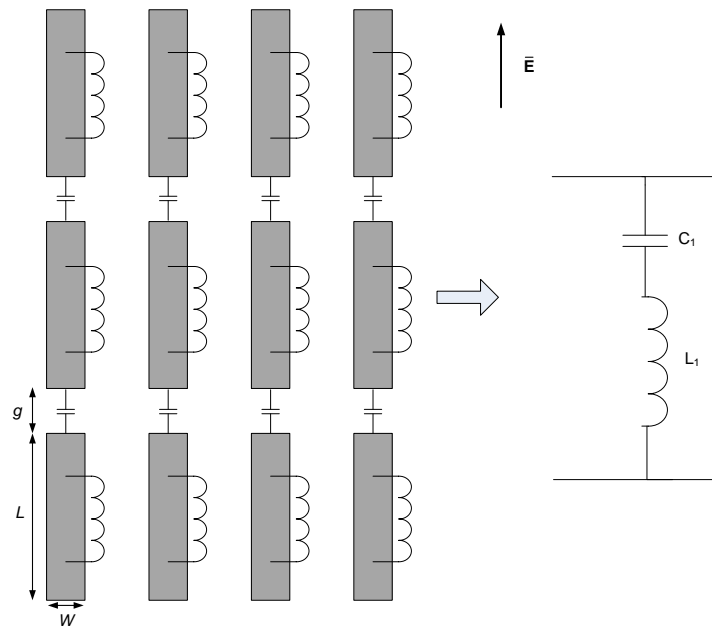
Figure 2.2. Dipole Array FSS with Equivalent LC Circuit

When currents are excited on the FSS by a plane wave polarized along the broad lengths of the dipoles (shown by E in Figure 2.2, with L and W defining the length and width of the conductor), this length acts an inductance (L_1), and the vertical gap between each dipole length (of width g) provides a capacitance (C_1) [1]. The desired frequency response of the FSS can be obtained by tuning L, W, and g to obtain the corresponding L and C values. For the dipole array FSS, the transmission frequency response is that of a

band-stop filter, meaning that signals can transmit through the FSS at any frequency outside of the designated stop band, and signals having frequencies within the stop band are reflected. The center frequency of this stop band (hereto referred to as the resonant frequency) is dictated by the resonant length, L, of the dipole with respect to the operating wavelength, λ. Typically, this resonance occurs when the length of the dipole is roughly equal to half the operating wavelength, $\lambda/2$, [1]. Conversely, in order to obtain a band-pass transmission resonance, a complementary slot-based array can be used. A slot-based FSS is composed of an array of resonant slots cut out of a metal sheet. Unlike conductive dipoles, these slots exhibit a band-pass resonance that occurs for an incident plane wave polarized perpendicularly to the broad length of the slot [1]. A slot is considered complimentary to a dipole when the dimensions of the slot match the dimensions of the dipole, meaning that the slot FSS transmits signals at frequencies where the dipole FSS reflects, and vice-versa. An example of transmission frequency responses for dipoles and slots with parallel oriented incident wave polarizations (denoted by E) is shown in Figure 2.3. This behavior is a consequence of Babinet's principle, and can generally be applied to most other FSS designs, if a complimentary response is needed [1]. This consideration may be inaccurate in the presence of thick dielectric slabs near the FSS, however, due to differences in impedance profiles between the complimentary FSS designs. Since the dipole FSS acts as a short circuit at resonance, and the slot FSS acts as an open circuit, the transmission lines representing the dielectric slabs are thus loaded differently, causing non-complimentary behavior between each FSS [3]. However, for practical use, the dipole FSS is often not used due to its strong dependence on the polarization of an incident plane wave. Should the plane wave not be polarized parallel to the length of the dipoles, the structure's resonance will be reduced. Furthermore, in the case of completely perpendicular polarization (opposite to the polarization depicted by E in Figure 2.3), the structure stops resonating completely [3]. To help alleviate this problem, a second dipole can be added to the structure that is perpendicular to the first dipole. This creates the crossed-dipole FSS (or Cross FSS), shown in Figure 2.4. For this FSS, the presence of the second dipole ensures that the polarization of an incident plane wave can never be completely perpendicular to the length of any one conductor.
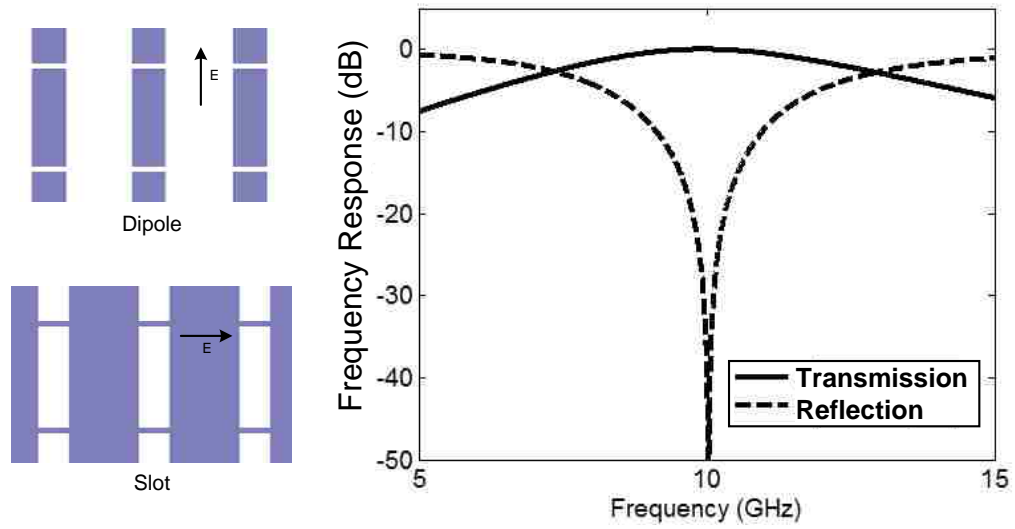
Figure 2.3. Complimentary transmission response of dipole array and slot array.
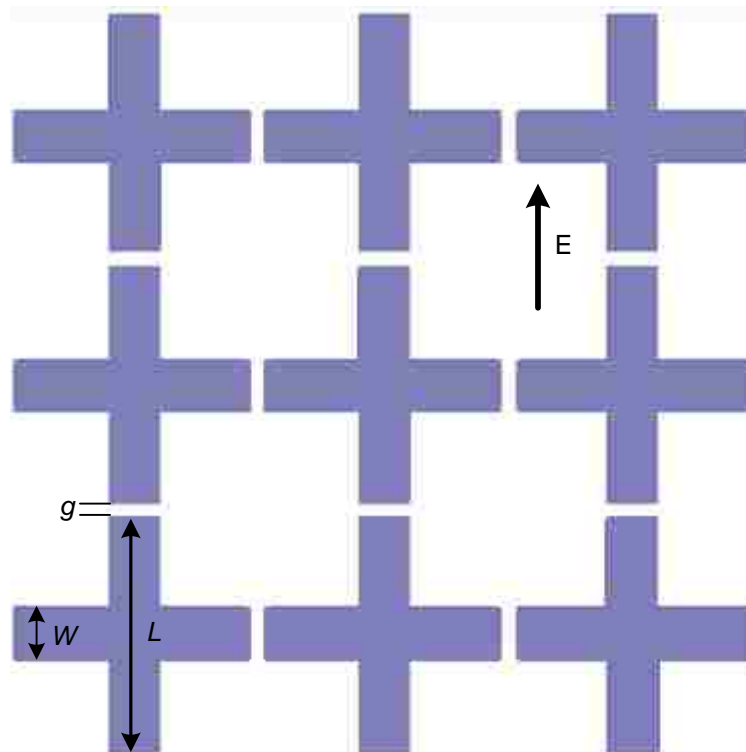
Figure 2.4. The crossed-dipole FSS.

Thus, while the resonance will still be dampened for non-parallel (to either dipole) polarizations, the resonance will not be completely removed. Additionally, this dampening will be less severe than for a single dipole, as both dipoles will still be partially excited for any arbitrary polarization. The addition of the second dipole can have adverse effects, however, in the form of an additional coupling mode that occurs between the perpendicular arms of the cross [3]. While this coupling does not occur when the FSS is excited by a normally incident plane wave, it does pose a problem when the plane wave is incident at certain (off-normal) angles in which the electric field of the plane wave is no longer parallel to the plane of the FSS (i.e., TM incidence). When this occurs, an additional resonance is created that is very close to the main resonance of the FSS [1]. As a result, the shape of the resonance can be significantly modified, thus creating an unintended frequency response. To resolve this problem, an additional set of "end-loading" dipoles can be added to the ends of each arm of the cross in order to better control this unwanted coupling [1]. This helps to move the unwanted resonance to a higher frequency, away from the main resonance. The addition of these end-loading dipoles creates the Jerusalem Cross FSS, shown in Figure 2.5 (a).

In this figure, the parameters of note are the gap width (g), central conductor length (D_1) and width (W_1), and end-loading conductor length (D_2) and width (W_2). Additionally, an example of the frequency response and equivalent circuit model is also shown in Figure 2.5 (b) and (c), respectively. As can be seen in the frequency response (Figure 2.5 (b)), the presence of the new end-loading dipoles adds a second stable transmission resonance (f_2) in addition to the original transmission resonance (f_0), giving this FSS multi-resonant behavior. Furthermore, in between these two transmission resonances there is also an impedance-controlled reflection resonance (f_1), giving additional design flexibility [13]. With this level of complexity, however, more advanced FSS design and analysis methods must be used.

Evaluating the frequency response of any given FSS design can be accomplished through a number of methods. These methods tend to rely on either numerical or analytical approximations, as the coupling behavior in an FSS tends to be too complex for direct evaluation. Numerical approximation methods, such as Method of Moments (MoM) [9], Finite-Difference Time Domain (FDTD) [10],
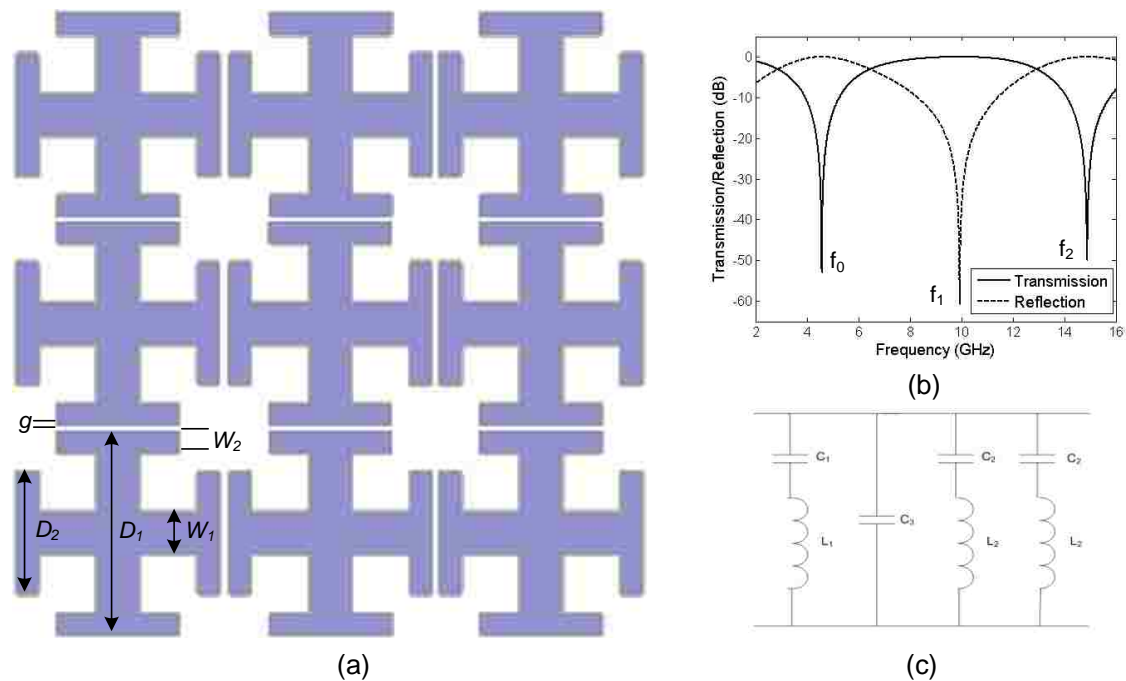
Figure 2.5. The Jerusalem Cross FSS (a), with associated frequency response (b) and equivalent circuit model (c).

and Finite-Element Method (FEM) [11], are often used to solve for the frequency response and field scattering of an FSS. This is accomplished by solving for the response of a single element of the FSS (referred to as a "unit cell") and then enforcing the effect of periodicity using Floquet boundary conditions [55]. These boundaries operate by analyzing the fields incident on a particular side wall of the unit cell (known as a "master" boundary), and then matching those fields on the opposite unit cell side wall (known as a "slave" boundary), with an additional phase term added which accounts for the effect of the incident angle of the impinging plane wave [11]. This method results in improved computation time (compared to modeling the full extent of a finite-sized FSS), but can be inaccurate when applied to FSS structures that don't have infinite (or at least,

effectively infinite) periodicity. Such structures include finite-size FSS (i.e. having a limited number of elements such that edge effects from the outer-most elements can significantly affect the response) and curved FSS structures [9]. However, these issues can often be compensated by doing further simulations of edge cases (i.e., elements on the edge of a finite-size FSS) or assuming locally planar behavior (for curved FSS structures), if possible [24]. The main advantages of numerical based solutions lie in their ability to be applied to any arbitrary FSS design, while also accounting for the effects of incident angle and polarization of an incident plane wave. The drawback of numerical methods, however, is the lengthy computation time required. This can become a problem for FSS design, as design practices using this method generally involve parameter sweeps and optimization techniques to obtain a desired frequency response. While this isn't necessarily a problem when fine-tuning an established design to meet specific criteria, a more expedient solution may be needed when first starting the design process. To help address this, a number of analytical approximation techniques have been developed to act as a starting point for FSS design. These techniques generally approximate FSS behavior as similar to more basic resonant structures that are easier to describe mathematically. In doing so, equations have been developed for a number of common FSS designs which give useful design parameters (such as the reactance of the FSS) based on the dimensions and surrounding geometry of an FSS [13], [16], [17]. This method of approximation often comes at the expense of neglecting the presence of more complicated electromagnetic mechanisms (such as the effects of incident angle or polarization), however, and thus is best suited only for initial design. While the details on this modeling approach are discussed in Chapter 4, the analytical approximations developed for a variety of FSS elements are discussed in this chapter, as they provide insight into how different aspects of the geometry of an FSS contribute to the inductance(s) and capacitance(s) in an FSS's associated equivalent LC circuit.

One such analytical method involves approximating the resonating FSS structure as an infinitely long conductive strip grating in order to obtain the equivalent inductances and capacitances of the FSS. Equations for the reactive and susceptive impedances of a conductive strip grating were originally derived by Marcuvitz, and are presented in [14].

$$X_{TE,TM} = F(p,w,\lambda,\theta) = \left(\frac{p}{\lambda}\right)\cos(\theta)\left[\ln\left(cosec\left(\frac{\pi w}{2p}\right)\right) + G_{TE,TM}(p,w,\lambda,\theta)\right] \qquad (2.1)$$

$$B_{TE,TM} = 4F(p,g,\lambda,\theta) = 4\left(\frac{p}{\lambda}\right)\cos(\theta)\left[\ln\left(cosec\left(\frac{\pi g}{2p}\right)\right) + G_{TE,TM}(p,g,\lambda,\theta)\right] \qquad (2.2)$$

Equation (2.1) describes the (normalized to the impedance of free space) inductive reactance of the strip grating when excited by a plane wave polarized parallel to the length of the strips. Equation (2.2) describes the normalized capacitive susceptance of the strip grating when excited by a plane wave that is polarized perpendicularly to the length of the strips. The variables w and g describe the width of the conductors and the width of the gaps between conductors, respectively, with p being equal to $w + g$. Additionally, λ is the operating wavelength of the incoming plane wave, and θ is the angle of incidence of the plane wave. Lastly, the function $G_{TE,TM}$ is given by the following equation.

$$G_{TE,TM}(p,x,\lambda,\theta) = \frac{1}{2}\frac{(1-\beta^2)^2\left[\left(1-\frac{\beta^4}{4}\right)(A_+ + A_-) + 4\beta^2 A_+ A_-\right]}{\left(1-\frac{\beta^2}{4}\right) + \beta^2\left(1+\frac{\beta^2}{2}-\frac{\beta^4}{8}\right)(A_+ + A_-) + 2\beta^6 A_+ A_-} \qquad (2.3)$$

where $A_{\pm}$ and β are given by (4) and (5).

$$A_{\pm} = \frac{1}{\sqrt{1\pm\frac{2p\sin(\theta)}{\lambda}-\left(\frac{p\cos(\theta)}{\lambda}\right)^2}} - 1 \qquad (2.4)$$

$$\beta = \sin\left(\frac{\pi w}{2p}\right) \qquad (2.5)$$

These equations can then be used to determine the individual capacitances and inductances of an FSS by estimating the lengths of conductor segments as a parallel-polarized strip grating through (2.1) and estimating the gaps between the ends of each conductor segments as a perpendicularly polarized strip grating through (2.2). For the case of the Jerusalem Cross in Figure. 2.5, there are five different circuit elements to be

calculated. The circuit elements L_1 and C_1 account for the first resonance, f_0, and is caused by the resonance of the main center dipole of length D_1. Since the gap, g, between the ends of the dipoles is much smaller than D_1, the inductance of the FSS structure will be nearly identical to that of an infinite strip grating. As such, the equivalent inductance can just be found directly through (1) as being $X_{1\ TE,TM} = F(p, W_1, \lambda)$, where $p = D_1 + g$, and W_1 is the width of the center dipole, as shown in Figure 2.5 [13]. The term θ is not included in the function F for this case, as the effect of incident angle is difficult to account for when these equations are used to describe an FSS. This is due to the FSS acting as both an inductive and capacitive strip grating, meaning that the FSS impedance is affected by both TE and TM incidence angles (meaning that the electric field (E-field) and/or magnetic field (H-field) is no longer perpendicular to the plane of the FSS), which isn't accounted for in Marcuvitz's original equations [22]. However, [22] provides modifications that can be made to Marcuvitz's equations to better account for incident angle (but are beyond this scope of this thesis and as such, are not discussed here). As such, it is assumed that $\theta = 0$ (i.e., normal incidence) whenever the incident angle is not specified. The capacitive term C_1 represents the capacitive coupling that occurs between the end-dipoles (of length D_2) [15]. This is described as a combination of two susceptances, B_g and B_d [13]. B_g is calculated as approximating the horizontal (as depicted in Figure 2.5) end-dipoles as a perpendicularly polarized strip grating of width W_2 and gap spacing g, giving a susceptance of $B_{g\ TE,TM} = 4\frac{D_2}{p}F(p, g, \lambda)$. The $\frac{D_2}{p}$ term is added to account for the fact that the end dipoles can't be approximated as being a continuous infinitely long conductive strip, as D_2 is generally much smaller than p. As such, the capacitance of the end-dipole is described as being only a fraction of the capacitance seen for a strip grating [13]. The susceptance B_d is caused by the additional coupling that occurs between the ends of the vertical end-dipoles, and can be found as $B_{d\ TE,TM} = 4\frac{2W_2+g}{p}F(p, p - D_2, \lambda)$. However, if the length D_2 is much smaller than the overall periodicity, this term can be considered largely negligible due to the large vertical spacing between end-dipoles.

The second resonance of the Jerusalem Cross FSS is created when the end-dipoles themselves resonate. This resonance is described by the circuit elements L_3 and C_3. Two

series combinations of these elements are placed in parallel in the circuit diagram in Figure 2.5 (c) in order to account for the fact that there are two vertical end-caps. The capacitance C_3 is the self-capacitance of the end-dipole, which can't be calculated using (2) [13]. Instead, this value can be found by assuming that the resonant wavelength (λ_3) of the end-dipole is equal to $\lambda_3 = (\frac{D_2}{0.49})$, and then using the relationship $f_2 = \frac{v}{\lambda_3} = \frac{1}{2\pi\sqrt{LC_3}}$. By finding the inductance, L, of a single end-dipole, the capacitance C_3 can be calculated. This inductance is solved using (1),

giving $X_{TE,TM} = 2\pi f_2 L = \frac{D_2}{p} F(p, W_2, \lambda_2)$. While this may seem redundant since f_2 has already been determined through this process, the values of C_3 and L_3 can still provide valuable information about the quality factor of the resonant curve, as well as the interactions of this resonance with the first resonance.

The inductance of each end-dipole, L_3, is comprised of two reactances, X_l and X_m. X_l accounts for the inductance of the two adjacent end-dipole lengths between FSS elements, and is calculated as $X_{l\ TE,TM} = \frac{D_2}{p} F(p, 2W_2 + g, \lambda_2)$. Meanwhile, X_m describes the mutual inductance between the end-dipole and center dipole, and is calculated as $X_{m\ TE,TM} = F(p/2, W_1 + g, \lambda_2)$. Lastly, the capacitance C_2 helps to describe the band-stop region f_1 that occurs between the resonances at f_0 and f_2, and is calculated as the sum of two additional capacitances, C_4 and C_5. C_4 is the self-capacitance of two adjacent end-dipoles, which are treated as a single dipole of width $2W_2+g$. This self-capacitance is solved in the same way as C_3, with the inductive reactance now being given as $X_{TE,TM} = 2\pi f_2 L = \frac{D_2}{p} F(p, 2W_2 + g, \lambda_2)$. Next, the capacitance C_5 accounts for the mutual capacitance that exists between the end-dipoles and the center dipole. This final capacitance is given by $B_{5\ TE,TM} = 4\frac{W_2}{p} F\left(\frac{p}{2}, \frac{p-D_1-g-2W_2}{2}, \lambda_2\right)$. Using this complete circuit model, the response of the FSS can be determined by calculating its equivalent admittance, Y, and this value can be subsequently used to find the reflection coefficient (ρ), calculated as $|\rho|^2 = \frac{Y^2}{Y^2+4}$. Additionally, the transmission coefficient (τ) is given by $|\tau|^2 = 1 - |\rho|^2$ [13]. A comparison of the results given between this method and HFSS simulation [23] is shown in Figure 2.6. For this comparison, the Jerusalem Cross

FSS had dimensions of D_1 = 17 mm, D_2 = 10.3 mm, W_1 = 2.3 mm, W_2 = 1 mm, and g = 0.4 mm, with normal incidence assumed. Additionally, the FSS was assumed to be located in free space (ε_r = 1), with no additional dielectric present.
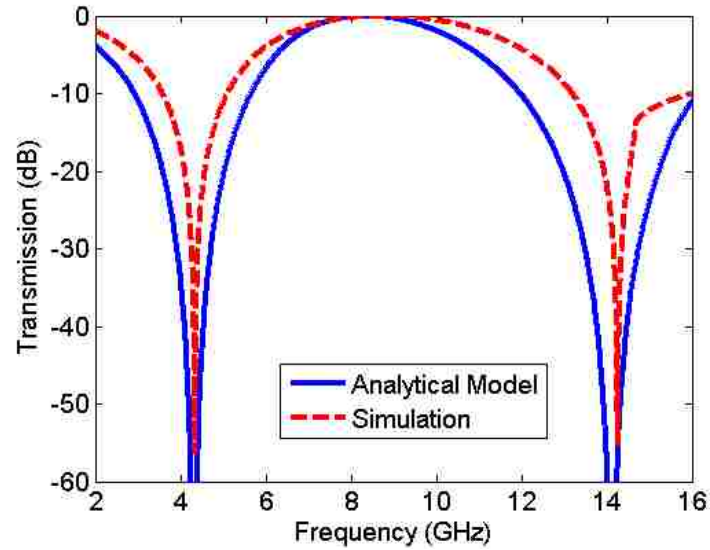
(a)
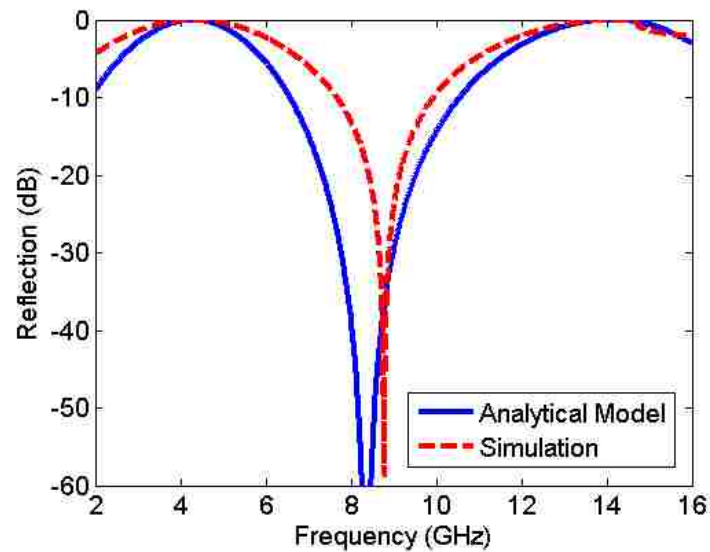
(b)

Figure 2.6. Comparison of HFSS simulation and Marcuvitz analytical model of transmission (a) and reflection (b) responses of the Jerusalem Cross FSS design.

Overall, the results of both methods shown in Figure 2.6 match fairly well. Minor variations in resonant frequency can be seen, however, for the first reflection resonance in Figure 2.6 (a) and second transmission resonance in Figure 2.6 (b), which demonstrate potential inaccuracies in the approximate analytical model. Additionally, there may also be inaccuracies in the response calculated from HFSS. However, the inaccuracies of the HFSS model are likely minor, due to tight tolerances on the adaptive meshing of the model during calculation. Furthermore, the depth and bandwidth of the resonances are different between each case due to the analytical model not accounting for the surface resistance of the FSS. Nonetheless, the analytical method is still fairly close to the simulated results, thus demonstrating its usefulness for initial FSS design work.

The final form of dipole-based FSS designs to be discussed is the tripole design. As the name suggests, a tripole FSS is a design consisting of three arms that are connected at a central point and spaced 120° from each other. The standard and end-loaded tripole variations are both shown in Figure 2.7.

(a)   (b)
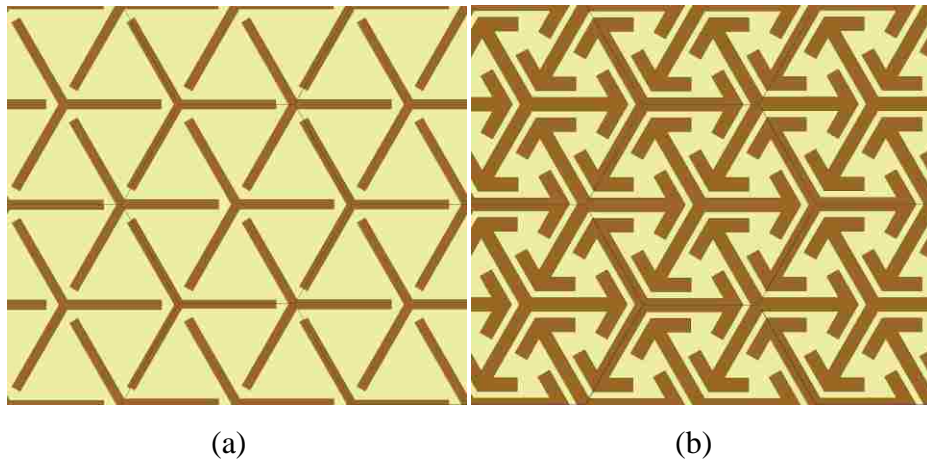
Figure 2.7. The Tripole FSS (a) and Loaded Tripole FSS (b).

The advantage of the tripole style design is the capability to orient the elements in a closely spaced hexagonal grid pattern. This close spacing helps reduce the sensitivity of the FSS to incident angle (which makes the FSS's behavior more consistent in a practical setting, since the angle of incidence may vary) while providing a large operating bandwidth for the transmission resonance [1]. This effect is further improved with the addition of the end-loading conductors seen on the ends of the tripole arms in Figure 2.7 (b). This end-loading helps to reduce the size of the elements due to the added inter-element coupling. The size reduction subsequently leads to an even closer element spacing, resulting in a wider transmission resonance bandwidth and greater insensitivity to incident angle [1].

2.2.2. Loop-Based FSS Elements. The next category of FSS design to be discussed is the loop-based element. As the name suggests, these elements are formed from loops of conductors. Examples of loop shapes include circular rings, square loops, and hexagonal loops, as shown in Figure 2.8. Additionally, dimensions are included for the square loop in Figure 2.8, as this element also has an analytical approximation model that is discussed below. These dimensions are the conductor length (d) and width (s), gap width (g), and element length (p, which is equal to $d + g$).
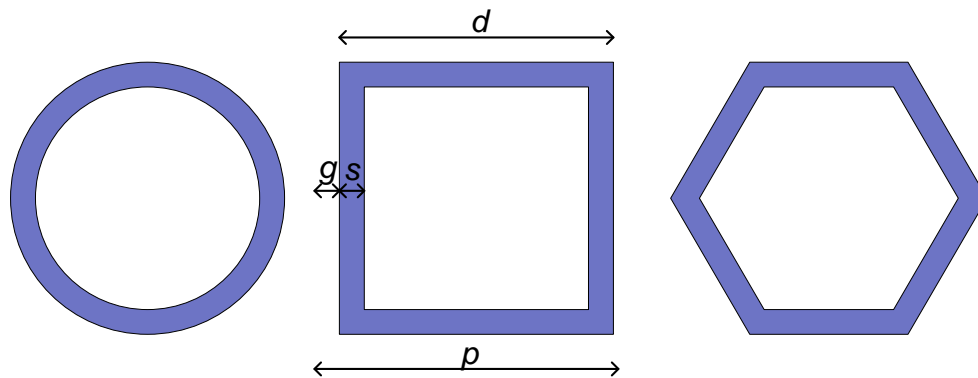
Figure 2.8. Examples of ring, square loop, and hexagonal loop FSSs

The main distinction between these forms of loop elements is how closely the elements can be spaced together. For instance, the circular and hexagonal elements can be spaced closest when in a hexagonal pattern, like the tripole above. The square loop, on the other hand, can only be spaced closest when in a square-grid arrangement. This consideration, as well as conductor width, affects the bandwidth and sensitivity to angle of incidence. Meanwhile, the resonant frequency of the FSS is determined by the circumference of the loop. More specifically, for a general loop FSS, the FSS resonates when the circumference of the loop is approximately equivalent to the operating wavelength [16]. Thus, by varying the conductor width, element spacing, orientation, and circumference, the desired overall frequency response can be acquired.

The frequency response for the square loop FSS can also be determined using analytical equations for initial design work, before relying on the slower full-wave simulations. These equations are similar to those presented above for the Jerusalem Cross, with some minor variations given as follows [16]. The square loop FSS frequency response is modeled by a single stage LC circuit. The inductive reactance, X1, is calculated as $X_{1\,TE,TM} = \frac{d}{p} F(p, 2s, \lambda)$, which corresponds to an inductance, given as L_1 [16]. Here, d corresponds to the lengths of each side of the loop, s corresponds to the width of the conductor, and p is the unit cell length, equal to $p = d + g$, where g is the width of the gap between elements, as shown above in Figure 2.8. Furthermore, the function F corresponds to the function presented above in equation (2.1). Note that the parameter w found in equation (2.1) (which corresponds to the strip grating conductor width) is represented here as being equal to $2s$. The reason for this is that the currents excited in the FSS occur only along the segments that are parallel to the incident E-field, which in this case corresponds to two of the four sides [4]. Since each of these segments are close to other segments (of neighboring elements, separated only by a narrow gap, g), the strip grating approximation is applied by assuming that these neighboring segments operate inductively as one single conductor segment of width $2s$, which are spaced apart from each other by the length of the unit cell. Lastly, a modifier of d/p is applied to the total inductance to account for the fact that these segments are not infinitely long, as was done for the Jerusalem Cross. Next, the susceptance, B_1, which corresponds to a

capacitance, given as C_1, is calculated as $B_{1\,TE,TM} = 4\frac{d}{p}F(p, g, \lambda)$. Given these equations, the frequency response can be calculated from the resultant impedance, the result of which is compared with HFSS simulation in Figure 2.9. For this comparison, the square loop was designed to have parameters of $d = 10$ mm, $s = 2$ mm, $g = 2$ mm, and $p = 12$ mm.
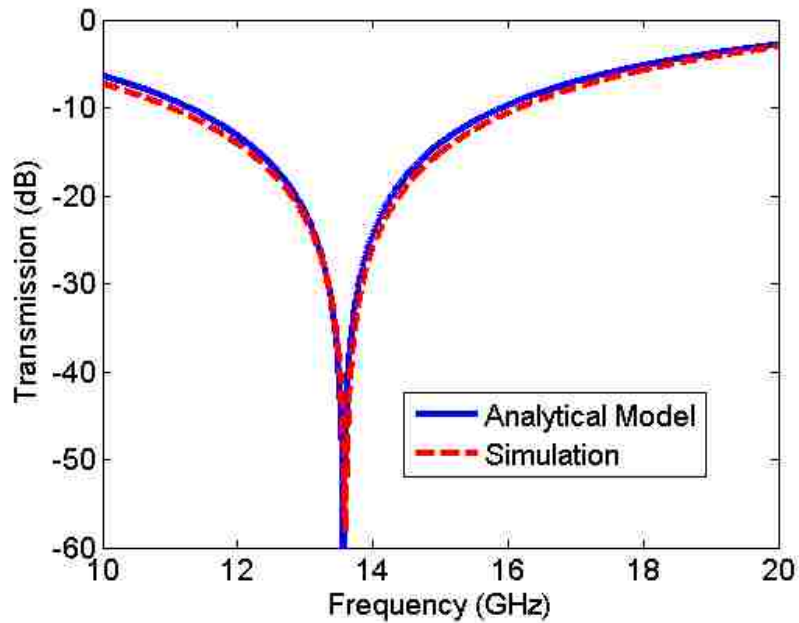
Figure 2.9. Comparison of HFSS simulation and Marcuvitz analytical model for the transmission response of Square Loop FSS.

As shown in Figure 2.9, the simulation and analytical model results match well. This again indicates the usefulness of analytical equations for FSS design due to its low computational requirements (when compared to full-wave simulation).

One unique advantage of the loop-type elements is the ability to incorporate higher frequency resonant structures into the FSS design. This is accomplished by adding additional rings into the interior of the initial outer ring. Since the resonant

frequency of these structures is related to the circumference of the rings, these interior rings add additional resonances to the frequency response [17], [18]. Examples of double and triple square loop FSSs are shown in Figure 2.10. Dimensions are included for double square loop for the analytical model below, and include the outer conductor length (d_1) and width (s_2), outer gap width (g_1), inner conductor length (d_2) and width (s_2), inner gap width (g_2) and element length (p, which is equal to d_1+g_1)
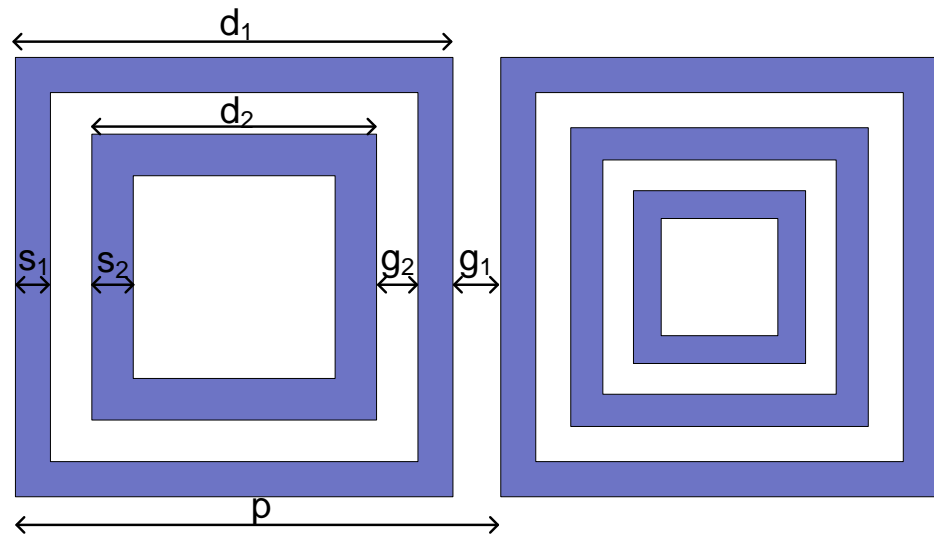
Figure 2.10. Double square loop (left) and triple square loop (right).

For the double square loop FSS design, the inductance of the inner square loop operates similarly to that of the single square loop, but its capacitance is affected by the outer loop. Meanwhile, the capacitance of the outer loop is reduced from that of the single loop design, and the reactance of the outer loop is affected by an additional inductance created by the width of the inner conductor loop, as is shown in the following

equivalent circuit approximation equations [17]. The equivalent circuit for the double square loop FSS is composed of two series LC circuits in parallel with each other (which corresponds to the double-resonant nature of the FSS). The value of L_1 for the first resonance is calculated as a parallel combination of two other inductances that correspond to the inductances created by the conductor lengths of both the inner and outer loop, given here as L_i and L_o, respectively. These inductances are calculated as $L_i = F(p, s_2, \lambda)$ and $L_o = F(p, s_1, \lambda)$. The total reactance for L_1 can then be calculated as $X_{1TE,TM} = \frac{2d_1}{p}\frac{L_iL_o}{L_i+L_o}$, where d_1 is the side-length of the outer loop, p is the unit cell length $p=d_1+g_1$, g_1 is the gap between neighboring outer square loops, and s_1 and s_2 are the widths of the outer and inner square loops, respectively.

The value for L_2 for the double square loop is calculated in a manner similar to L_2 of the single loop above, with the associated reactance for L_2 calculated as $X_{2TE,TM} = \frac{d_2}{p}F(p, 2s_2, \lambda)$, where d_2 is the side-length of the inner loop. Next, the susceptances corresponding to C_1 and C_2 are calculated based on the values of two separate capacitances, C_i and C_o, which are related to the inner and outer conductor rings, respectively. The capacitance C_i is calculated as $C_i = 4F(p, g_2, \lambda)$ (with g_2 being the gap between each square loop) and C_o is calculated as $C_o = 4F(p, g_1, \lambda)$. From these, the susceptance for C_1 is calculated as $B_{1TE,TM} = 0.75\frac{d_1}{p}C_o$ and the susceptance for C_2 is calculated as $B_{2TE,TM} = \frac{d_2}{p}\frac{C_oC_i}{C_o+C_i}$. The resulting frequency response of this circuit-based analytical model is compared to simulation results in Figure 2.11. For this comparison, the dimensions of the double square loop were set as $d_1 = 4.8$ mm, $w_1 = g_1 = w_2 = 0.2$ mm, $d_2 = 3.5$ mm, $g_2 = 0.45$ mm, and $p = 5$ mm.

Overall, the results obtained by HFSS and the circuit approximation model equations have comparable resonant behavior. More specifically, the resonant frequencies from both methods differ by approximately 1 GHz. Although not exact, these circuit approximations can still be useful for an initial estimate of an FSS's frequency response when first developing an FSS. The loop concept can also be applied to other FSS types, creating hybrid elements, such as the Cross Loop FSS shown in Figure 2.12.
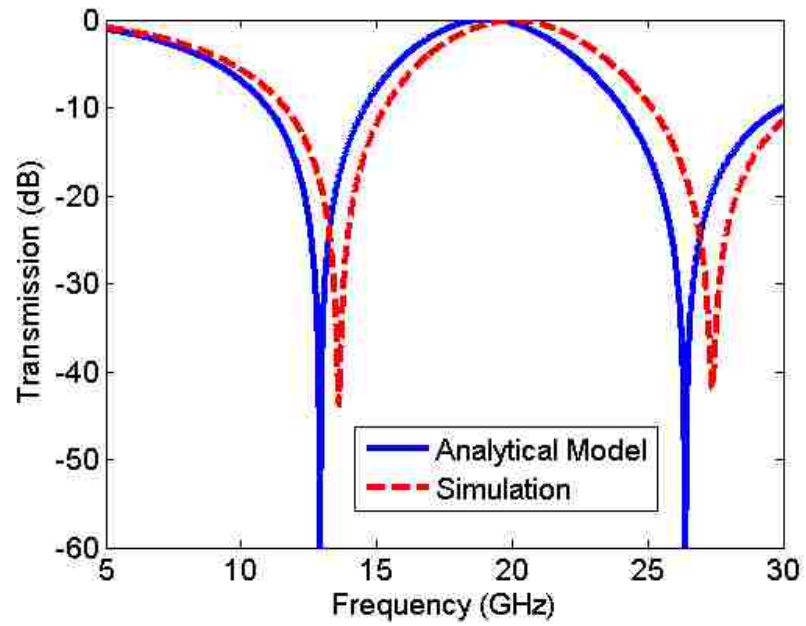
Figure 2.11. Comparison of HFSS simulation and Marcuvitz model for the transmission response of Double Square Loop FSS.
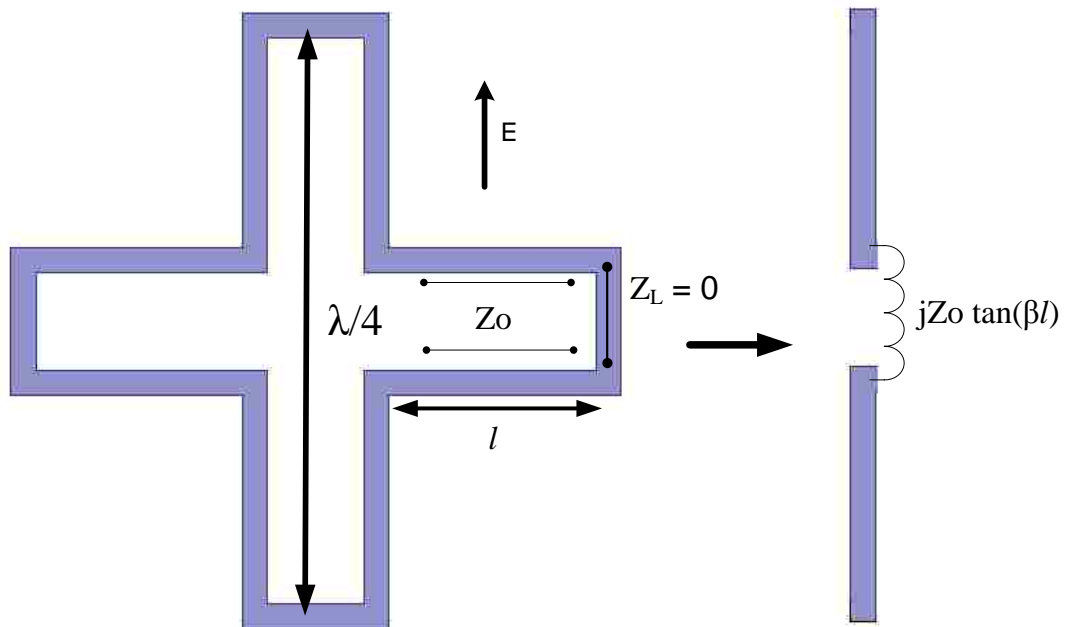
Figure 2.12. The Cross Loop FSS.

The main advantage given by this hybridized design is that the overall element size can be reduced. This is possible because the arms that aren't parallel to the E-field of the incoming wave instead act as an inductive impedance. This impedance occurs due to the arms acting as a two-wire transmission line loaded with a short (of load impedance $Z_L = 0\Omega$) at the end. This gives a reactive response based on the length of the arms, l, as well as the effective impedance of the two-wire transmission line, given as Z_o. If the lengths of all four arms are assumed the same, then at resonance, the length l will be equal to $\lambda/8$, giving an inductive response [1]. This inductance essentially makes up for the inductance lost by the reduction in the length of the element, thus allowing the element to be made smaller while still operating at a fixed frequency. Another advantage given by this design is that the bandwidth of the resonance can be easily controlled by changing the impedance, Z_0, of the two-wire transmission line [1]. This can be changed by tuning both the conductor width of the element, as well as the interior spacing between each line, thus giving a number of design parameters that can be adjusted without affecting resonant frequency, making the Cross Loop FSS a highly versatile design. Naturally, many other hybridized designs can also be created by combining elements of different FSS designs. However, this is beyond the scope of this thesis and is not discussed here.

2.3. PRACTICAL DESIGN CONCERNS

While the shape and dimensions of an FSS element plays the greatest role in determining the frequency response of the FSS, the overall response is also affected by other factors. For example, practical concerns, such as the presence of a supporting dielectric layer (upon which an FSS may be etched), or the incident angle of an impinging plane wave can cause the resonant frequency to drift or be dampened. Other environmental concerns, such as the presence of a ground plane near the FSS or curvature of the FSS, can more drastically alter the frequency response. As a result, these structure-dependent concerns must be evaluated to understand how an FSS will behave in a real-world system. As such, it may be possible to design an FSS in order to counteract or even take advantage of these effects. Thus, the mechanisms behind these environmental and practical effects will now be discussed.

2.3.1. Effects of Supporting Dielectrics on Frequency Response. One common concern when implementing an FSS in a structure is how the structure itself will affect the FSS response. Such a structure can include the dielectric substrate that the FSS is printed on, any dielectric structural materials that surround the FSS, and the presence of conductors (which will be discussed in a separate section). The presence of dielectric layers around an FSS can affect the frequency response in two ways. First, a dielectric near the FSS will directly increase the capacitance of the FSS [19]. The increase in capacitance caused by this dielectric loading will then reduce the resonant frequency of the FSS, while also changing the depth and bandwidth of the resonance. The resonance bandwidth is changed because the capacitance is affected by the permittivity of the material, but the inductance is not. Conversely, if the material is magnetic (not typical for an FSS substrate), then the inductance will also increase (as well as the capacitance, depending on the material's permittivity). Additionally, the degree to which the capacitance of the FSS is increased is related to the thickness of the dielectric, as well as its proximity to the FSS. If a dielectric layer completely surrounds an FSS on both sides, and is thicker than approximately 0.4p (where p is the length of the unit cell), then the capacitance is multiplied by the relative permittivity, ε_r, of the material [2]. However, if the material is very thin compared to the dimensions of the FSS, or if there are multiple materials surrounding the FSS, then the change in capacitance won't be purely related to the permittivity (ε_r) of any one material. Instead, the capacitance of the FSS is shifted by a modified permittivity that is referred to as the effective (relative) permittivity, $\varepsilon_{r,eff}$ [19]. For example, if different materials of appropriate thickness (such that all capacitive coupling from the FSS occurs within them) are present on each side of the FSS, then the value of $\varepsilon_{r,eff}$ is calculated as an average between the permittivity of the materials on either side of the FSS. In the case of a thick dielectric present on one side of the FSS only, the value of $\varepsilon_{r,eff}$ will be the average of the permittivity of the material and of free space, which leads to $\varepsilon_{r,eff} = \frac{\varepsilon_r + 1}{2}$ [20]. However, for the case of a very thin dielectric near the FSS, the calculation of $\varepsilon_{r,eff}$ becomes more difficult since the value of $\varepsilon_{r,eff}$ does not change linearly with the thickness of the dielectric. The reason for this is that the majority of the electric field coupling in the FSS occurs directly at the surface of the FSS, and falls off non-linearly with distance from the FSS [19]. Furthermore, the complexity

of calculating $\varepsilon_{\mathrm{r},eff}$ is further increased if multiple layers of thin dielectrics are present. The treatment of this problem as it relates to FSS design is discussed later in Section 4. The presence of a multi-layer dielectric can also have a passive effect on the frequency response when measuring an FSS. That is to say, a layered dielectric structure alone will also lead to additional resonant behavior due to the presence of reflections at interfaces between different dielectrics [19]. If this additional resonant response occurs near the operating frequency of the FSS, FSS measurement may become more difficult, as the presence of these dielectric resonance(s) may potentially hide the resonance of the FSS. Depending on the characteristics and requirements of the structure in which the FSS is embedded, this issue can be counteracted in a number of ways. First, if a portion of the structure does not have an FSS present, this portion can be used to isolate the response of the structure itself. With this data, the response of the structure can be removed from the overall frequency response (including the FSS response), thus yielding the effect of the FSS alone. Alternatively, if needed, the use of an active FSS can be employed. This form of FSS can essentially be designed to have its resonance switched on or off using, for example, PIN diodes properly connected throughout the surface of the FSS [6]. By modulating between the on and off states of the FSS resonance, the resonance of the FSS can be resolved from other resonances in a structure.

   2.3.2. Incident Angle. In an ideal system, an FSS will be excited by normally incident radiation. However, in a real-world application, the propagation direction may not be known or controllable. As such, an FSS may need to be designed to operate under a wide range of incidence angles. However, the effect of incident angle on FSS operation is often complicated, making it difficult to calculate the FSS response through analytical means. As such, when incident angle is a concern, full-wave simulation will generally be required in order to understand how the frequency response of the FSS will be affected. However, most basic FSS elements have a similar response to incident angle. In general, incident angle will affect the frequency response of an FSS in two ways, depending on whether the mode of incidence is as a TE or TM wave. A visual representation of these modes is shown in Figure 2.13. Blue arrows indicate E-field direction for each incidence definitions, while green arrows indicate the magnetic field (H-field). Meanwhile, black

arrows indicate direction of propagation (DOP), while θ and φ indicate angle of TE and TM incidence, respectively.
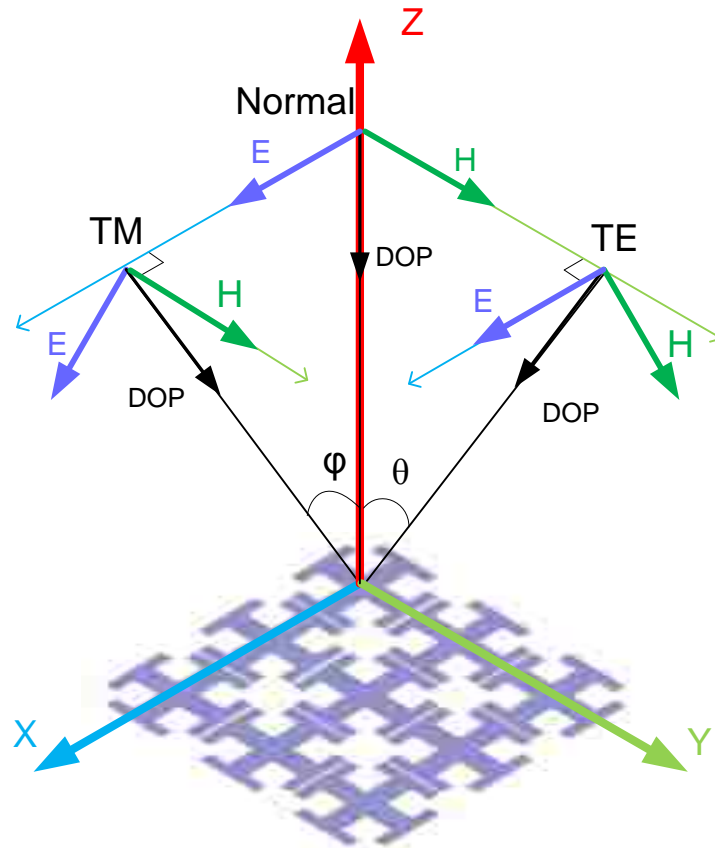
Figure 2.13. Illustration of TE and TM incidence.

For a TM incident wave, the incident angle of the incoming plane wave causes a portion of the electric field to be normal to the plane of the FSS, with the magnetic field remaining completely parallel to the plane of the FSS. As a result, the resonance of the FSS tends to become dampened, with stronger dampening occurring for higher angles of incidence. This happens due to the occurrence of larger phase differences between

adjacent elements [3]. For TE incidence, the magnetic field has a vector component that is normal to the plane of the FSS, while the electric field remains parallel to the plane of the FSS. When this type of incidence occurs, the resonant frequency of the FSS will generally be shifted, usually without noticeably affecting resonant bandwidth. This occurs because incident angle-induced phase differences occurring along the parallel-polarized length of the FSS will cause the FSS to behave as though it were longer, thus shifting the frequency of the FSS [21]. Lastly, if the electric and magnetic fields of an obliquely incident plane wave both have some component normal to the plane of the FSS, a combination of TE and TM mode effects will occur, changing the frequency and depth of resonance. As such, since these effects may alter the expected frequency response of the FSS, a number of corrective measures may be needed.

For most cases, two common design practices can be implemented to mitigate the effects of incident angle on the resonant response of an FSS. First, when designing the FSS, it is often considered good practice to orient the elements of the FSS to ensure a minimal (or reduced) element spacing [1]. By doing this, the distance between elements can be minimized, thus reducing the effect of phase difference between elements caused by incident angle. Naturally, some elements are easier to arrange closely than others, and are considered more desirable to use should incident angle be a consideration. A few of these elements, as discussed in section 2.2, include the various loop type elements [21]. Other hybridized elements (such as the Jerusalem Cross) can also provide a greater insensitivity to incident angle. The second method that can be used to reduce the effects of incident angle involves strategic use of dielectric layers that can surround the FSS [3]. If a dielectric layer is placed between the FSS and the incident plane wave source, the incident angle seen by the FSS will be reduced due to Snell's Law [19]. That is to say, at the interface between the dielectric layer and the surrounding environment (generally assumed to be air), the incident plane wave will be refracted closer to the plane of the FSS due to the permittivity of the dielectric, reducing the incident angle.

Generally, it is ideal for the thickness of the supporting dielectric to be a multiple of $\lambda/4$ in order to reduce the effect of its impedance and corresponding reflections through quarter-wave transformation [1]. However, it may not always be possible to control the dimensions of the support structure surrounding the FSS, meaning that the

dielectric structure may cause additional resonances in the frequency response. As such, the effects of both the presence of the material and the incident angle will need to be accounted for in this case. Lastly, the use of a dielectric for incident angle compensation is generally more effective for TE incidence, rather than for TM incidence. This is due to the effectiveness of the dielectric being reduced for TM incidence as the angle of incidence approaches the Brewster Angle, where the interface between the dielectric and air no longer reflects. In this case, the $\lambda/4$ dielectric thickness specification becomes a requirement [21].

  2.3.2.1 Curved FSS. Another concern for the implementation of an FSS in a practical system occurs when the FSS needs to be conformed to a curved structure. Examples of applications where an FSS may be curved include sub-reflector antenna dishes and stealth radome structures [24]. When an FSS is curved, a number of changes in the FSS's frequency response can occur, depending on the nature of the curvature. Geometrically speaking, there are two forms of curvature to take into account [27]. First, there is the singly-curved FSS, which conforms to the shape of a cylinder. Secondly, there is the doubly-curved FSS, which is conformed to a spherically or conically rounded surface, such as a nose cone on an aircraft. Naturally, the effect of double-curvature on the frequency response is more severe than that of the single-curvature. In either case, however, the overall effects of curvature are similar. In general, a curved FSS will have an altered resonant response from an equivalent planar FSS. This occurs due to a reduction of impedance in the FSS resulting from changes in FSS coupling caused by the curvature. In addition, the effect of curvature causes there to be a different incident angle amongst the elements of the FSS, causing differences in both phase and magnitude for each of the elements over the FSS surface [25]. This is exacerbated further by the fact that the curvature will also cause the plane wave to reach some portions of the FSS before others, adding another degree of variation in phase difference over the FSS [25]. Another concern with a curved FSS is the possibility of coupling between non-adjacent elements, as the geometry of the curvature causes the distance between non-adjacent elements to become shorter [24]. As a result, the currents excited on the elements of the FSS may be significantly altered [25]. Simulations may also be difficult when designing a curved FSS, as periodic unit cells can no longer be used in standard simulators, since the

curvature breaks the periodicity of the FSS. As a result, in order to obtain an accurate simulated frequency response, the entire structure of the curved FSS may have to be simulated. Thus, simulations may take an extensive amount of time or be impossible due to computational limitations [26]. As such, it may be necessary to utilize planar approximations (as long as the curvature is not extreme and the effects of phase and incident angle can be accounted for [26]). Another strategy may be to use well-established FSS element designs that respond well to curvature (such as the circular ring [27]), such that the simulated planar response provides enough design validation to support the building and testing of a curved FSS.

2.3.2.2 Effect of conductors on FSS. The final structural consideration to be discussed is the presence of a conductive ground plane or additional FSS layers on the response of an FSS. When an FSS is embedded into a structure with a ground plane, a transmission response is no longer possible. Instead, the grounded FSS acts as an absorber, giving a reflection resonance at a prescribed frequency. This absorbing behavior occurs due to the FSS acting as a high-impedance surface (HIS), essentially acting as a matched load at resonance, with energy being absorbed by the resistivity of the FSS and through the loss in the dielectric substrate [7]. When the ground plane is considered "far" from the FSS (such that there is no coupling between them), an additional parallel inductance is created by the conductor-backed dielectric, acting as a transmission-line impedance [28]. To control the resonant response of the FSS, this additional inductance must be compensated for by using a highly capacitive FSS element, such as a patch. Additionally, since the impedance of the FSS isn't directly affected by the ground plane, the effect of the ground plane on the overall frequency response can be accounted for with transmission line theory, assuming the impedance of the FSS is known [28]. This is done by treating the ground plane as a shorted load at the end of a transmission line separating the ground plane and FSS. However, when the ground plane is located closer to the FSS, the FSS will begin to couple to the ground plane. In doing so, the capacitance of the FSS will increase, while the inductance decreases [27]. This is caused by the reduction of the gap between FSS and ground restricting the magnetic field (H-field) coupling around the FSS while increasing E-field coupling between the FSS and ground. In this arrangement, the use of highly capacitive elements will no longer be

needed to account for the higher inductance. Instead, traditional dipole and loop elements can be used [27]. The disadvantage of this arrangement, however, is that the complexity of the FSS now requires the use of simulation for design work, as no simple analytical model for a ground plane coupled FSS is readily available. Despite this minor design issue, HIS FSS designs have proven invaluable for use as thin absorbers in embedded antenna and stealth applications [1], [3].

If a second FSS should be present in a structure, the above behaviors become more complicated. Naturally, when two separate FSS layers are far from each other, the overall response can again be determined using transmission line theory, with each FSS acting as an individual reactive impedance separated by dielectric layers that act as transmission line segments [30]. However, when these FSS layers are moved near each other, they begin to couple. This coupling is much more complicated than that of the ground plane since the coupling is highly dependent on the different FSS geometries. As such, there is a fair degree of difficulty in predicting the resultant FSS responses outside of numerical simulation [30]. Due to this significant complexity, this type of FSS configuration won't be discussed in detail here, and will instead be left for future investigations. Instead, only non-coupling multi-layer FSS's will be used for the purposes of this thesis.

2.4. CONCLUSION

In this section, FSS history, theory, and operation were presented. Several examples of common FSS elements were used to highlight the geometrical dependence of the FSS's resonant filtering behavior. Additionally, a variety of FSS frequency response calculation methods were discussed, including full-wave simulation and analytical approximations. Finally, a number of issues for practical implementation of FSS were considered, such as the effects of incident angle, FSS curvature, and the presence of dielectrics and conductors local to the FSS.

In summary, the reflection/transmission response of an FSS is affected not only by the geometry of the conductors of the FSS, but also by the nature of the structure in which the FSS is embedded. For any given FSS, incident energy is either reflected or transmitted over certain frequencies due to inductances and capacitances generated

between elements of the FSS. These inductances and capacitance values are determined by the dimensions of the FSS geometry, such as conductor length and width and gap width. Additionally, the frequency response of the FSS can be altered by nearby dielectrics and conductors, incident plane wave orientation, and FSS curvature. By observing how the response of an FSS is affected by these geometrical considerations, correlations (such as the effect of geometry on resonant frequency or resonant band-shape) can be drawn, linking geometrical effects to the resultant frequency response. Thus, if the geometry of an FSS embedded in a structure is deformed due to stresses in that structure, the nature of these geometrical deformations may be determined from the resultant change in frequency response. Based on this observation, FSSs may find application for structural health monitoring purposes by taking advantage of their geometrical dependencies. From this perspective, the potential applications of FSSs as embedded sensors are investigated through the rest of this thesis.

3. APPLICATIONS OF FSS FOR NORMAL STRAIN AND SHEAR STRAIN SENSING

In this section, the effects of normal and shear strain deformation are investigated for a variety of common FSS designs. Since the frequency response of an FSS is heavily geometry dependent, deformation of this geometry will alter the frequency response. As such, by understanding how the frequency response of a given FSS is modified by geometry-altering deformations, it may be possible to use FSS's as both surface-mounted and embedded structural health monitoring (SHM) sensors. That is, if an FSS is installed on a structure that undergoes mechanical stress, both the structure and the embedded FSS will be similarly deformed. Thus, the changes in the frequency response of the FSS brought on by this deformation (and subsequently the normal and/or shear strain) can be monitored remotely by interrogating the FSS using an external measurement system. Thus, since the mechanical state of the structure can be remotely interrogated using FSS-based sensors, the structure can be considered a "smart structure" that has inherent SHM capabilities [35].

The use of an FSS as an SHM sensor was first applied for normal strain detection in [31], [32], [33], and [34]. With this work in mind, the measurement of normal strain with FSS's is discussed in Section 3.1. Meanwhile, Section 3.2 focuses on utilizing FSS's to characterize shear strain. Finally, Section 3.3 discusses the application of FSSs to SHM of steel-tube reinforced concrete columns.

3.1. EFFECTS OF STRAIN ON FSS RESPONSE

The first type of deformation to be discussed is that of normal strain. Normal strain is defined here as being a stretching or compressing deformation of a material caused by an applied force. Normal strain is quantified as a unitless vector having a magnitude and direction [39]. The magnitude of the normal strain is defined as a ratio of the length of the stretched/compressed structure in relation to the original, non-strained structure. For example, a bar that has increased to 1.5 times its original length is said to have 0.5 normal strain. Furthermore, the polarity of this normal strain value indicates whether tension or compression is taking place, with tension (i.e., an increase in length) resulting in positive normal strain and compression (i.e., a decrease in length) resulting in

negative normal strain. Additionally, the normal strain also has a directional component associated with it, describing the vector (direction) along which the normal strain is taking place [32].

In Section 2, it is stated that the resonant frequency of an FSS is primarily dependent on the conductor lengths within the FSS. That is, as the length of a conductive element increases or decreases, the resonant frequency of this conductor respectively decreases or increases due to the relation between operating wavelength (λ) and conductor length. Therefore, it is expected that a similar shift in resonant frequency will occur if the length of this conductor were altered by normal strain [31]. Whether the FSS dimensions are either lengthened or shortened depends on the polarity of the normal strain (i.e., tension or compression). Furthermore, the direction of the normal strain vector dictates what aspects of the FSS's geometry are deformed, which has subsequent ramifications on the frequency response. For this investigation, it is assumed that all normal strain occurs parallel to the plane of the FSS. This is because normal strains oriented orthogonal to the plane of the FSS produce no noticeable effect on the geometry of the FSS (and related frequency response), and thus are not considered.

The effect of normal strain on the resonant response of an FSS can also be described from a circuit element perspective by modeling the FSS as a band-pass or band-stop RLC filter circuit (composed of resistors, capacitors, and inductors which represent the coupling and surface resistance of the FSS). In an RLC filter circuit, the resonant frequency (f_0) is calculated as $f_0 = 1/(2\pi LC)$, where L and C are the inductance and capacitance of the circuit. Meanwhile, the resistance, R, of the filter determines the depth of the filter's resonance. When an FSS undergoes normal strain, the L and C values of the FSS are altered. For instance, as the length of an FSS's conductor increases, the associated L also increases. Conversely, as the distance between conductors is increased, C decreases due to a reduction in electric field coupling. Meanwhile, the surface resistance of the FSS remains effectively unaltered by normal strain, barring minor changes due to an increase in the conductor surface area (not considered in this investigation). Taken together, these changes in L and C collectively alter the resonant frequency, while the depth of the FSS's resonance remains unchanged due to the unaltered R. To illustrate this, an example of a crossed-dipole FSS under

normal strain is shown in Figure 3.1 (a). Additionally, the simulated (using HFSS [23]) transmission responses for different values of normal strain are given in Figure 3.1 (b), while the resonant frequency of this FSS is plotted as a function of normal strain in Figure 3.1 (c). The polarization of the incident plane wave is assumed parallel to the direction of normal strain, as indicated by the vector labeled 'E' in Figure 3.1 (a), unless otherwise specified.

(a)   (b)

(c)
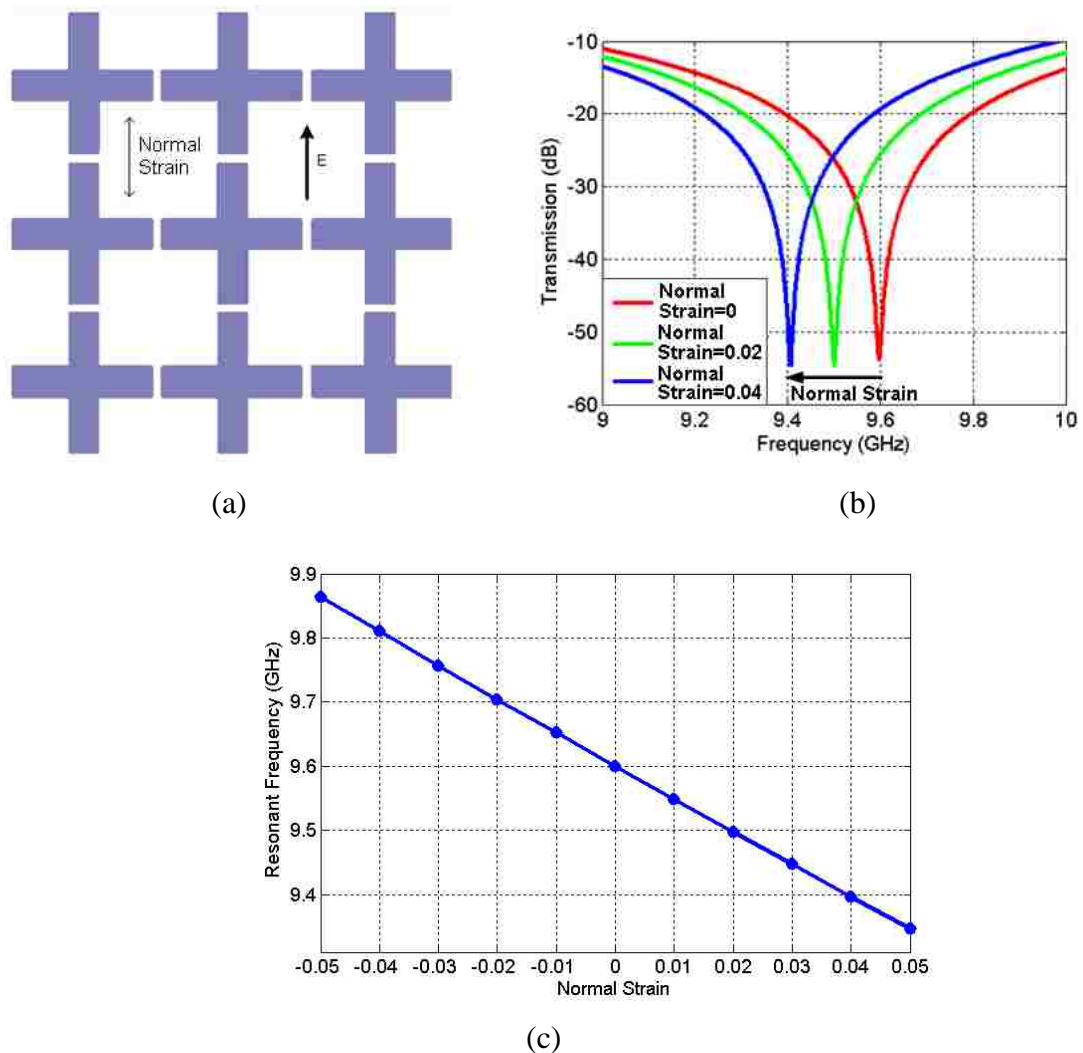
Figure 3.1. Crossed-dipole FSS's geometry (a), its transmission response as a function of normal strain (b), and its resonant frequency as a function of normal strain.

In Figure 3.1 (b), the FSS's resonant frequency is shown to decrease proportionally with normal strain, with the resonant depth remaining relatively undisturbed. Furthermore, the frequency shift follows a linear relationship with the normal strain, as shown in Figure 3.1 (c). This occurs because the resonant wavelength (λ) is linearly related to the length of the dipoles in the Crossed-dipole FSS, which resonates for a dipole length equal to $\lambda/2$. However, this linearity may not always be true for all element types. The sensitivity of an FSS's resonant frequency to normal strain can be quantified by considering its gauge factor, ς, which relates normal strain to change in resonant frequency, and is calculated using Equation 3.1 [35].

$$\varsigma = \frac{\Delta f}{f_0 * \Delta s} \tag{3.1}$$

Here, Δf is the change in resonant frequency for a given change in normal strain, Δs [35]. Furthermore, this value is normalized by the FSS's un-deformed resonant frequency (f_0) so that the sensitivity of FSSs with different resonant frequencies to normal strain can be compared directly. For the FSS of Figure. 3.1, ς was calculated as 0.51, based on the resonant frequency shift determined using full-wave simulation. Naturally, since different FSS designs have different dependences between geometric dimensions and resonant wavelengths, each FSS will have its own value of ς. As such, the normalized ς values (calculated through simulation) for a variety of FSSs (shown in Figure 3.2) are presented in Table 3.1. Note that grounded FSS's are defined here as having a ground plane 0.127 mm below the FSS.

Based on Table 3.1, dipole-type FSSs (such as the Crossed-dipole, Jerusalem Cross, and Tripole FSSs) have similar ς values. Meanwhile, the square loop element has a smaller ς, making it less sensitive to normal strain and therefore potentially unsuitable for strain sensing purposes. Additionally, grounded FSSs have a higher ς than their ungrounded counterparts, making the addition of a ground plane advantageous if it can be included in a structure. It should be noted that ς for these FSS elements is only representative of these specific elements, and therefore may vary if the dimensions of the element are changed. As such, to investigate the effect of FSS dimensions on ς, a simulation was conducted in which the conductor length, conductor width, and gap width

of a crossed-dipole FSS were each varied over a range of normal strains. The resulting ς is reported below in Table 3.2.
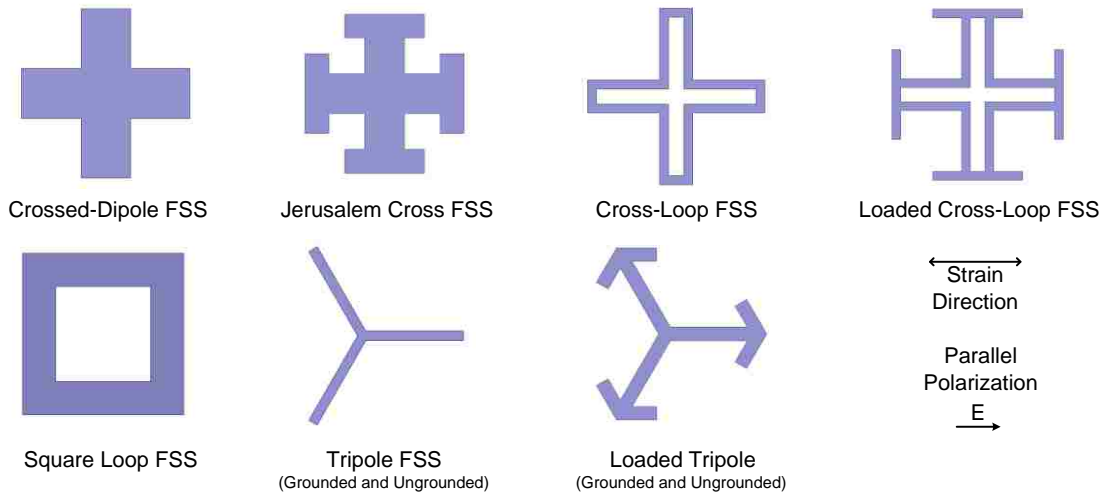
Figure 3.2. Examples of FSS elements used for strain analysis in Table 3.1.

Table 3.1. Gauge factors for common FSS elements.

FSS Elements	Gauge factor (ς)
Crossed-Dipole	0.53
Jerusalem Cross	0.54
Square Loop	0.18
Tripole	0.68
Grounded Tripole	0.74
Loaded Tripole	0.56
Grounded Loaded Tripole	0.7
Cross Loop	0.57
Loaded Cross Loop	0.52

Table 3.2. Gauge factors of Crossed-Dipole FSS for different element dimensions.

Parameter Studied	Gap Width	Conductor Length	Conductor Width	Gauge factor
Gap Width	3.5 mm	17 mm	5 mm	0.51
	4.5 mm	17 mm	5 mm	0.5
	5.5 mm	17 mm	5 mm	0.49
Conductor Length	4.5 mm	15 mm	5 mm	0.46
	4.5 mm	17 mm	6 mm	0.5
	4.5 mm	19 mm	7 mm	0.55
Conductor Width	4.5 mm	17 mm	3 mm	0.36
	4.5 mm	18 mm	5 mm	0.5
	4.5 mm	19 mm	7 mm	0.67

For the crossed-dipole element, ς doesn't change significantly with gap width or conductor length. Conductor width, however, has a more substantial effect on ς (meaning that a given normal strain will cause a greater shift in resonant frequency), with ς increasing as conductor width decreases. When conductor width decreases, the inductance of the FSS is increased, while the FSS's capacitance decreases, all while having a minimal effect on resonant frequency (since $f_0 = 1/(2\pi LC)$). This implies that decreasing inductance (while increasing capacitance to maintain the same resonant frequency) increases sensitivity to normal strain (as described by ς). As such, conductor width could be used to tune (improve) ς of a given element if desired.

For all cases presented thus far, the polarization of the incident plane wave was parallel to the direction of normal strain. However, when the incident plane wave is not polarized parallel to the direction of normal strain, the effect of normal strain on the FSS resonance is altered. The reason for this can be explained by principles of FSS operation discussed previously in Section 2. Recall that for a given FSS, the currents induced in that FSS only occur along conductor lengths that are parallel to the electric field of the exciting plane wave [3]. For example, when a crossed-dipole FSS is illuminated by a

normally incident plane wave polarized along one of the two dipole-lengths, only that dipole will have induced current, while the other dipole essentially remains unexcited. The consequence of this is that the geometry of the unexcited dipole does not contribute to the frequency response of the FSS, meaning that the cross FSS essentially operates as a single dipole FSS for this polarization. This selective behavior also applies to an FSS that has undergone normal strain. If the direction of normal strain is perpendicular to the polarization of the interrogating plane wave, this normal strain will not affect the frequency response of the FSS. An example of the polarization dependence on the frequency response of a strained crossed-dipole FSS is shown in Figure 3.3. In this figure, simulation results are presented for the crossed-dipole FSS under normal strain that is aligned parallel (co-polar) (a) and perpendicular (cross-polar) (b) to the incident plane wave polarization.

(a)   (b)
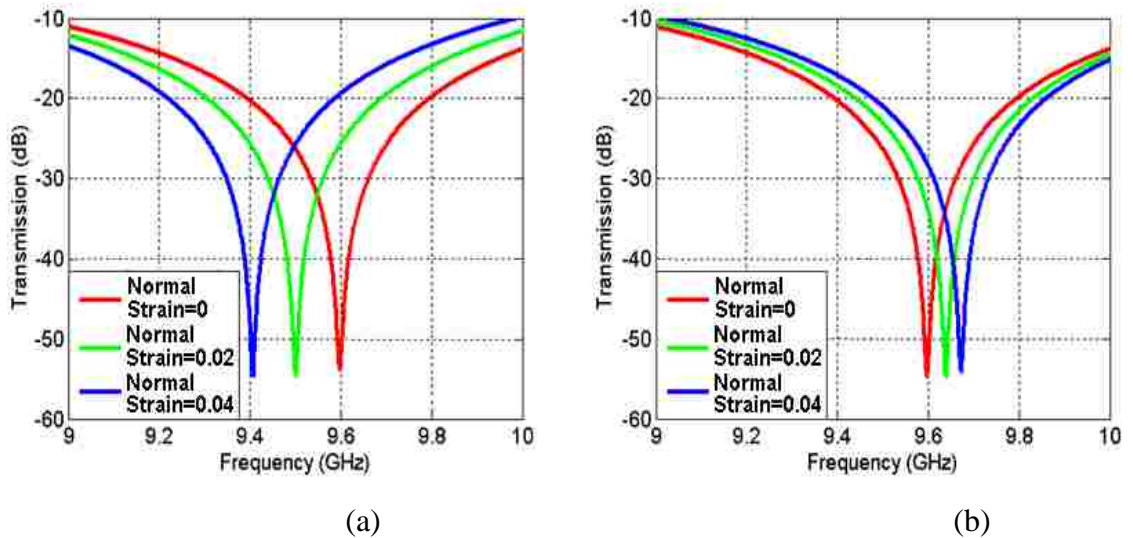
Figure 3.3. Frequency response of the crossed-dipole FSS undergoing co-polar (a) and cross-polar (b) normal strain.

By comparing Figure 3.3 (a) and (b), it is seen that cross-polar normal strain alters the resonant frequency less than co-polar normal strain. This occurs because the conductor lengths deformed by normal strain are not the conductor lengths determining the frequency response (i.e., excited by the incident plane wave). Instead, the strain will only alter the width of the excited conductor, which has a minimal effect on resonant frequency. As such, the effect of normal strain on resonant frequency is dependent on the polarization of the incident plane wave. Additionally, the resonant frequency is increased for cross-polar normal strain, rather than decreased. This occurs because the only FSS geometry that is being changed (in the direction of polarization) for the cross-polar case is the conductor width, which has a minimal impact on resonant frequency. More specifically, an increase in conductor width increases the capacitance of the FSS, while decreasing the inductance, altering the resonant frequency ($f_0 = 1/(2\pi LC)$). However, the impact of conductor width on resonant frequency is relatively minor when compared to the effects of conductor length and gap width since the L and C values are altered inversely when conductor width is changed , thus making the shift in resonant frequency less significant. Instead, a change in conductor width will have a greater effect on the FSS's ς, as indicated in Table 3.2. As such, this change in ς due to cross-polar normal strain may lead to consequences in measuring normal strain when an FSS has normal strain along both axes (a concern that may need to be addressed in a practical system). For the purpose of normal strain sensing, this polarization dependent response is actually advantageous. By rotating the polarization of the interrogating wave, the direction of an unknown normal strain can be determined remotely. This is possible because the normal strain direction corresponds directly with the polarization angle at which the maximum frequency shift occurs. Alternatively, instead of rotating the polarization, a structure could be analyzed using two orthogonally polarized antennas, with normal strain direction determined through vector decomposition. That is, although a normal strain may not be parallel to the polarization of either antenna, the net effect of normal strain in those two polarization directions can be used to determine the vector direction. However, this approach assumes there is only one normal strain affecting the structure. This will generally not be the case, though, as most normal strains will often have an additional orthogonally oriented inverse normal strain associated with them [39]. For instance, if a

material under tension in a given direction, it will tend to contract in the direction perpendicular to the tension. The ratio between the amount of contracting that occurs for a given amount of tension (or vice-versa) is a material property referred to as Poisson's ratio [39]. This value is highly material dependent and must be taken into account during normal strain measurements. As such, the use of a rotating linearly polarized source may be needed to determine all present normal strains, as vector decomposition would fail in this case.

In order to verify the simulated FSS normal strain behaviors discussed above, measurements were made on an FSS that had undergone normal strain. The FSS design used for this investigation was the grounded tripole FSS illustrated in Figure 3.4, with relevant dimensions labeled and specified below. L is the central conductor length, W the central conductor width, g is the gap width, and d is the end dipole length.
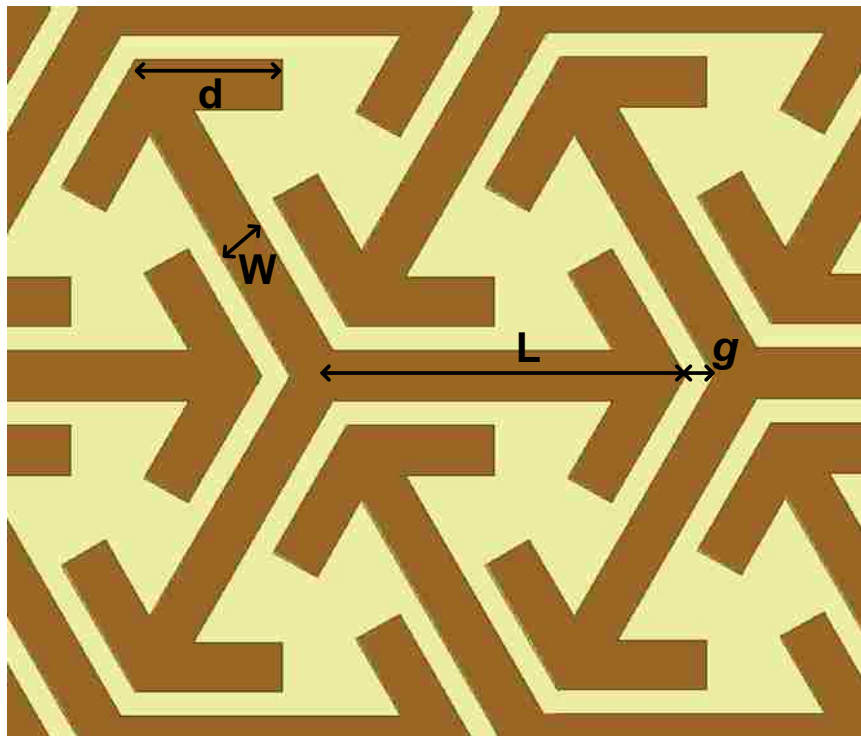
Figure 3.4. Grounded Tripole FSS with relevant dimensions.

The dimensions of this tripole are $L = 3.75$ mm, $g = 0.3$ mm, $W = 0.5$ mm, and $d = 1.5$ mm, with a Roger's RT/Duroid 5880 dielectric substrate of 0.127 mm thickness having a relative permittivity (ε_r) of $\varepsilon_r = 2.2$ and loss tangent of 0.0009. This FSS was designed to have a reflection resonance occurring at 10 GHz. The frequency response of this FSS was measured using a calibrated HP 8510C Vector Network Analyzer (VNA) in both normal strained and unstrained states. Normal straining of the FSS was accomplished by plastically deforming the FSS sample using a universal testing machine (UTC) [35]. Normal strain measurements were conducted on the deformed sample after it had been removed from the UTC to avoid the possibility of the UTC physically interfering with the measurement results. This could be done because the UTC plastically deformed the sample, meaning that the FSS retained some degree of normal strain deformation after having been deformed by the UTC. The amount of this normal strain remaining on the FSS was subsequently measured using calipers, which measured that normal strains of 0, 0.006, and 0.015 had been applied. The frequency response of this structure was subsequently measured using the test setup shown in Figure 3.5.
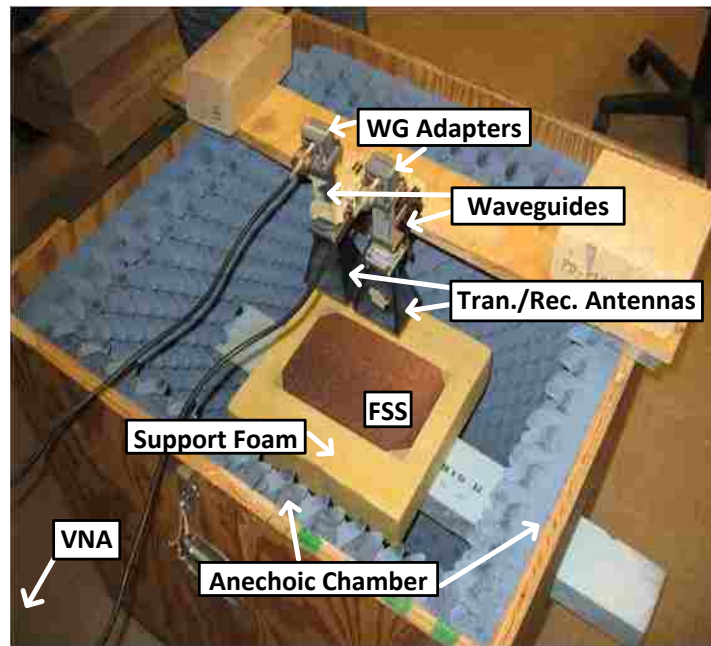
Figure 3.5. Grounded Loaded Tripole frequency response measurement setup.

In this test setup, the FSS was measured with a dual horn antenna system operating in the X-band frequency range (8.2-12.4 GHz). Additionally, the FSS was placed in an anechoic chamber to reduce reflections from the surrounding environment. In this chamber, the reflection response (frequency response of the reflected signal) was measured by suspending two horn antennas collinearly, spaced 7 mm apart. Two antennas were used so that both co-polarization and cross-polarization could be investigated. In this arrangement, the excitation signal is transmitted by one horn, reflected from the FSS, and received in the other horn. One issue with this arrangement is that the transmission path between the transmitting antenna, FSS, and receiving antenna creates approximately 10° of incidence angle with the FSS surface, which affects the frequency response. As was discussed in Section 2, off-normal incidence can result in changes in the FSS's resonant depth, as well as minor changes in resonant frequency. However, a 10° incident angle is assumed to be small enough such that its affect is minimal. Additionally, since this incident angle doesn't change between measurement sets, its effect on resonant frequency is consistent through all measurements. Co-polarized interrogation was measured by orienting the polarizations of the horn antennas in parallel, thus ensuring that the transmitted/received electric fields of the two antennas were aligned parallel to each other. Meanwhile, cross-polarized reflection was measured by rotating one of the antennas 90°, causing the radiated electric fields from each antenna to be oriented perpendicularly. Ordinarily, no signal would be transmitted between the antennas in such an arrangement due to the polarization mismatch. However, there will be transmission if the FSS surface changes the polarization of the reflected wave, which may occur when the FSS is deformed in some way (i.e., shear strain). This topic is discussed further in Section 3.2.

Practical measurement concerns include unintended coupling between horn antennas, as well as the effects of the local environment on the measured frequency response. For the test setup shown in Figure 3.5, the FSS sample was measured in a small semi-anechoic chamber in order to reduce environmental reflections. Additionally, the FSS was supported in the chamber by a set of foam blocks with a permittivity similar to free space, meaning that the foam blocks only nominally affect the interrogating signal. In addition to the frequency response measurements of the FSS ($S21_{FSS}$),

additional measurements of the background system were taken to account for scattering losses and unintended coupling between the interrogating antennas. Scattering loss was accounted for by measuring the test setup with a conductive plate in place of the FSS (labeled as $S21_{conductor}$), accounting for losses caused by the interrogating signal not being reflected towards the receiving antenna. Additionally, a measurement of the test setup was taken with the antennas radiating into an empty anechoic chamber. This measurement (labeled as $S21_{air}$) isolated any unintended coupling that occurred between the antennas, as all other interrogating signals would be absorbed by the chamber. From these, the normalized FSS response, $S21_{norm}$, was determined using Equation (3.2), allowing the FSS's resonance to be isolated from all other aspects of the measured frequency response.

$$S21_{norm} = \frac{S21_{FSS} - S21_{air}}{S21_{conductor} - S21_{air}} \tag{3.2}$$

Using this normalization procedure, the frequency responses for the grounded tripole FSS were measured for normal strains of 0, 0.006, and 0.015. The results of these measurements are presented in Figure 3.6 for normal strains oriented parallel and perpendicular to the incident polarization.

For the normal strains oriented parallel to the polarization of the incident wave, the resonance of the FSS is reduced from 9.9 GHz in the un-deformed state to 9.86 GHz for 0.015 normal strain, giving ς of 0.249. This ς is less than half the value calculated through simulation of this structure, which produced a ς of 0.76. Unexpectedly, a similar change in resonant frequency occurred for the perpendicularly polarized measurement. While some positive displacement is expected due to Poisson's ratio (as discussed above), the degree of compressive strain is generally expected to be a fraction of the expansive normal strain applied. Additionally, the resonances of the normal strained sample appear to be much deeper than for the un-deformed sample, which is not expected from simulation. One possible explanation for these discrepancies may be that the normal strain was not applied uniformly over the FSS, meaning that a normal strain

distribution may be contributing to the frequency response of the FSS (rather than one specific value). Furthermore, ς of the FSS may have been affected during the deformation process due to cross-polarized normal strain arising, as described by Poisson's Ratio. This would have altered the width the FSS's conductors, leading to unexpected changes in resonant frequency for either polarization, as well as changes in ς, as shown in Table 3.2. As such, additional FSS samples and measurements may be necessary to fully investigate how the Poisson's ratio of a sample affects normal strain detection. Unfortunately, however, additional grounded loaded tripole FSS samples were unavailable for normal strain testing at the time of this investigation. Finally, cross-polarized transmission data is not presented, as all measured cross-polarized transmissions were below the noise floor of the system (~ -90 dB). Altogether, however, the results shown here support the use of FSS for strain sensing.
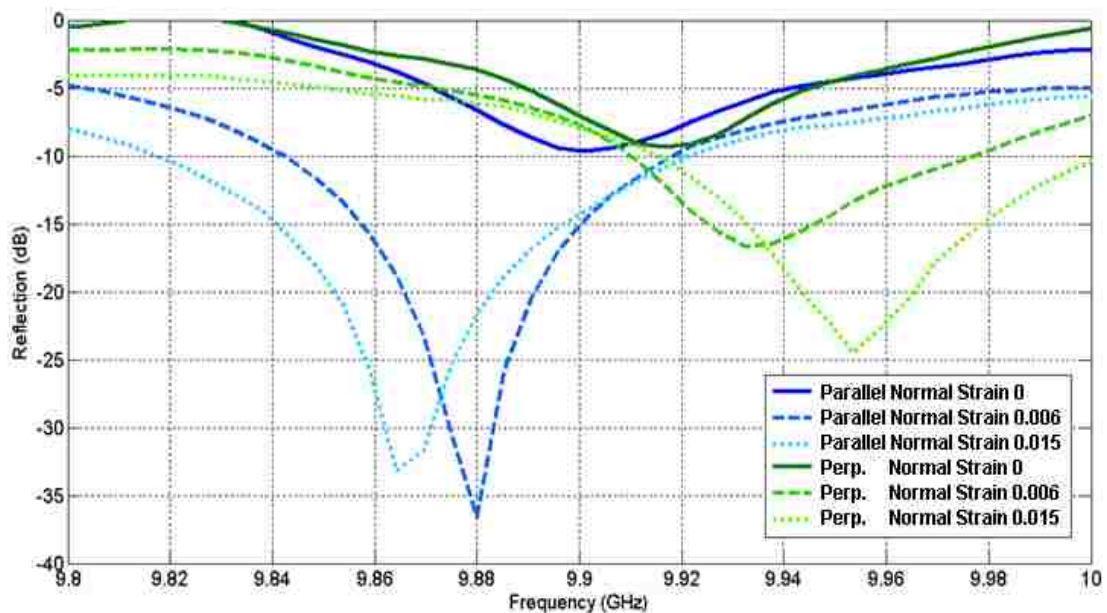
Figure 3.6. Parallel and perpendicularly oriented measurement results of Grounded Loaded Tripole FSS under normal strain.

Next, the effects of the angle between the interrogating wave polarization and normal strain direction (referred to as the polarization angle) were investigated. To accomplish this, a second series of measurements were taken to investigate how the FSS resonance changed as a function of polarization angle. This polarization dependency was measured by rotating the FSS and keeping the measurement antennas stationary. Measurements were taken for 10° increments of rotation until a full 360° rotation was achieved. The antennas were arranged similarly to the test setup in Figure 3.5 above, only without the semi-anechoic chamber. The two antennas used were spaced 8.5 mm apart, at a height of 30 cm from the FSS surface. These measurements were normalized using the above procedure given in equation (3.2), but without the $S21_{air}$ measurement. This was done because the $S21_{air}$ measurement couldn't be taken without significant changes to the static system. Thus, direct coupling between the two antennas may have caused some minor errors in the measurements. However, these errors would have been consistent throughout the measurements, so these measurements would still be comparable. The shift in resonant frequency as a function of polarization angle for each variation of normal strain on the FSS (0, 0.006, and 0.015) is shown in Figure 3.7. Here, 0° polarization angle corresponds to a polarization that is perpendicular to the direction of normal strain.
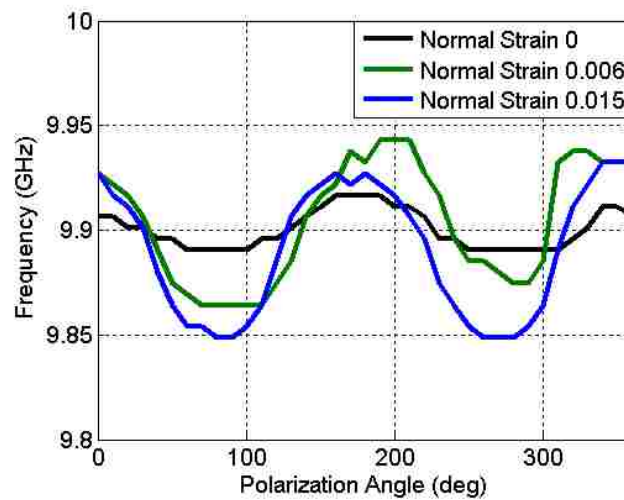
Figure 3.7. Resonant frequency of strained Grounded Loaded Tripole as a function of polarization angle.

According to these results, the resonant frequency of the FSS is directly dependent on polarization angle when the FSS has undergone normal strain, as corroborated by previous measurements and simulation (shown above in Figure 3.6). Additionally, the resonant frequency is consistently reduced for increasing parallel polarized normal strain (90° and 270°), corresponding to the measurements taken in Figure 3.6. However, the perpendicularly polarized normal strain measurements (0°, 180°, and 360°) behave more erratically, with the 0.006 normal strain case increasing the resonant frequency more than the 0.015 normal strain case did at the 180° rotation measurement. This may be due to inaccuracies in measurement or the effects of Poisson's ratio (as discussed above).

3.2. EFFECTS OF SHEAR STRAIN ON FSS RESPONSE

Like normal strain, shear strain is another form of mechanical deformation. Structurally, shear strain is defined as a twisting deformation on a structure caused by rotational force [36]. The geometrical effect of shear strain on a structure can be described using a coordinate translation at each point. For a structure geometry that is mapped to a 2-D Cartesian plane (that is, each point of the structure has an associated X and Y coordinate), this translation can be described by the equations $X_{new} = X + Y * S_{xy}$ and $Y_{new} = Y + X * S_{xy}$ [35]. Here, X and Y are the coordinates at some specified point on the geometry, X_{new} and Y_{new} are the new coordinates for the point after the structure has undergone shear strain, and S_{xy} is the dimensionless magnitude of the shear strain. Unlike the normal strains mentioned in Section 3.1, shear strain doesn't have a specified directional vector. Instead, shear strain is defined only by S_{xy}, with larger S_{xy} values indicating greater shear strain. An illustration of the effect of shear strain on FSS geometry is shown in Figure 3.8 for the loaded tripole.

To understand how an FSS can be used to detect shear strain, the response of an FSS to shear strain must first be characterized. To begin, a simulation was conducted to find the reflection response of the grounded loaded tripole shown in Figure 3.8. This reflection response is given in Figure 3.9 for both co-polarization (a) and cross-polarization (b) responses.
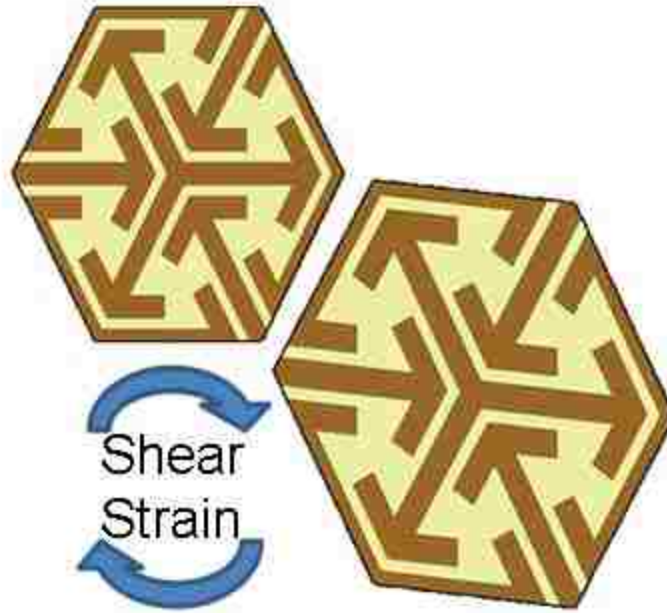
Figure 3.8. Illustration of original (top left) and sheared (bottom right) loaded tripole.

From Figure 3.9, several observations can be noted regarding the effect of shear strain on the response of the FSS. First, shear strain has a negligible effect on the FSS's resonant frequency for both co-polarization and cross-polarization. This is due to a lack of geometrical change (conductor lengths and gap widths) of the FSS as a result of the shear strain, meaning that the FSS's impedance remains unchanged (which determines the resonant frequency). This result may be beneficial for FSS sensing applications, as the effects of shear strain may be differentiated from the effects of normal strain for an FSS undergoing multiple deformations. That is, since shear strain doesn't significantly affect the co-polarized resonant frequency, any shifts in resonant frequency would likely only be due to normal strain. However, shear strain does reduce the depth of the co-polarized resonance for this FSS, and causes the resonance to split around the resonant frequency for 0.03 (and greater) shear strain. Similar resonance peak splitting behavior is seen for the cross-polarization response at 0.03 shear strain, shown in Figure 3.9 (b).
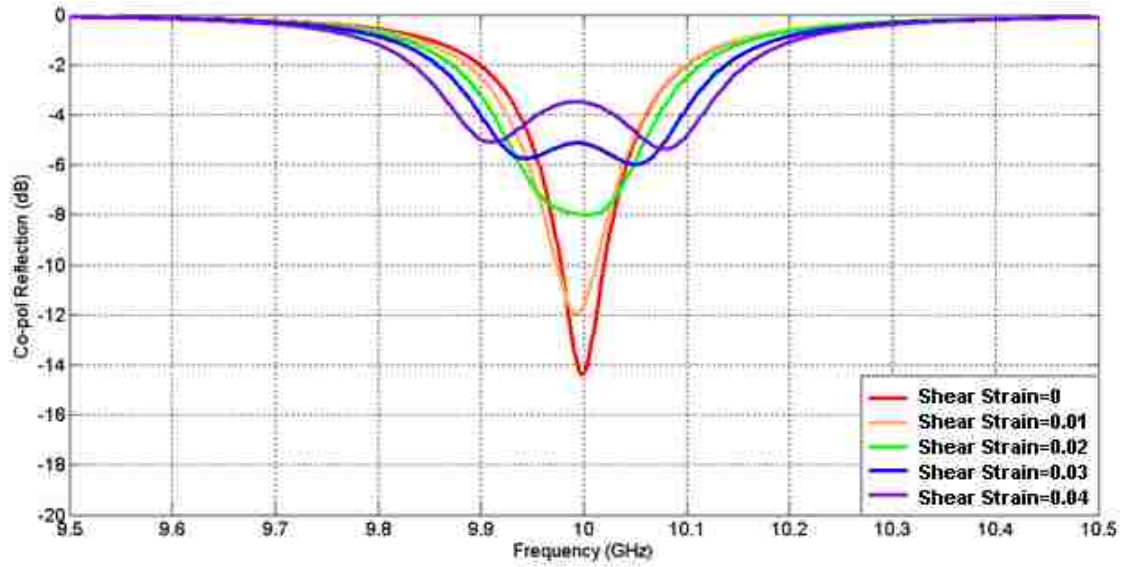
(a)
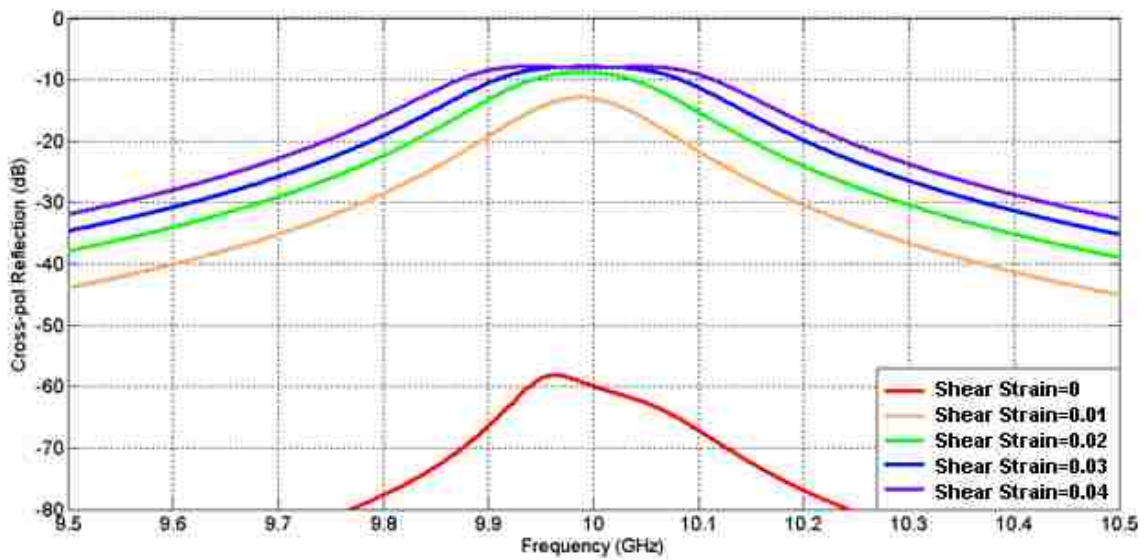
(b)

Figure 3.9. Co-polarization (a) and cross-polarization (b) reflection response of Grounded Loaded Tripole as a function of shear strain.

According to these observations, when an FSS undergoes shear strain deformation, the FSS begins to reflect radiation at its resonant frequency that is cross-polarized with respect to that of the incident radiation, with the level of cross-polarized

radiation increasing with increasing shear strain. The reason for this increase is due a reduction in the symmetry of the FSS as a result of the shear strain deformation. This loss of symmetry results in the generation of currents that are directed perpendicularly to the direction of the incident electric field. Normally, when current is generated on an un-deformed FSS by an incident plane wave, the perpendicular currents will cancel each other out due to element symmetry around the axis of the electric field. However, when this symmetry is broken, these currents flow freely, resulting in the cross-polarized radiation seen in Figure 3.9. Examples of these cross-polarized surface currents for grounded tripole FSSs without shear strain and with 0.05 shear strain are shown in Figure 3.10 (a) and (b) respectively.

As can be seen in the sample without shear strain (Figure 3.10a), any currents that are polarized perpendicularly (that is, those directed vertically in the figure) to the incident electric field (directed horizontally in the figure) have a similar mirrored current around the horizontal axis of the FSS. As such, any radiation from these currents effectively cancels out. However, once shearing occurs, a high degree of vertical, perpendicularly polarized current is generated along with the horizontal, parallel-polarized current found in co-polarized operation. For the grounded tripole examined here, these vertical currents can be observed for the 0.05 shear strain represented in Figure 3.10. This effect can also be seen in the cross-polarized frequency response shown in Figure 3.9 (b), where the cross-polarization resonant peak begins to flatten out and broaden at -10 dB. While the magnitude of cross-polarization does not increase any further at the resonant frequency, the overall response is still increasing in magnitude across the spectrum, causing the peak to flatten out at the observed -10 dB limit. This resultant flat-toped peak can be considered as analogous to a clipped signal and likely occurs due to energy conservation between the parallel and perpendicular surface currents, as well as inherent resistive losses in the FSS. This peak value of the cross-polarized signal may be a limiting factor for detecting larger shear strains. As such, some elements (such as the grounded-loaded tripole examined here) may be too sensitive to shear strain for practical usage, depending on the sensing requirements for a given application.
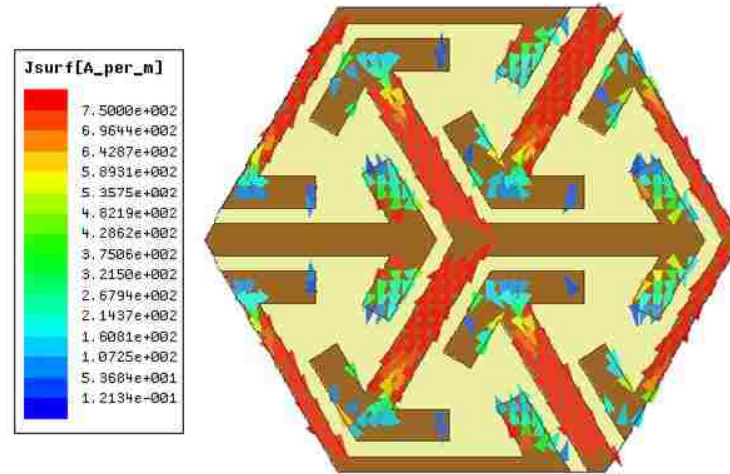
(a)
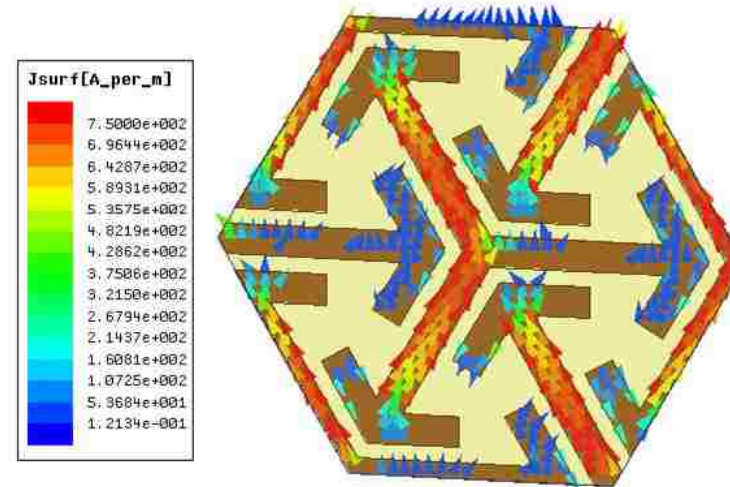
(b)

Figure 3.10. Simulated surface currents on Grounded Loaded Tripole FSS without shear strain (a) and with shear strain (b).

To analyze how element shape determines sensitivity to shear strain, the response of a variety of FSS designs (shown below in Figure 3.11) to shear strain were simulated. Note that grounded FSS's are defined here as having a ground plane 0.127 mm below the FSS, and that all FSS elements shown are assumed un-grounded unless otherwise

specified. Since the magnitude of the cross-polarization peak doesn't change linearly with shear strain, a single shear modulus cannot be determined (as was done above for normal strain in Equation 3.1). Instead, the magnitude of cross-polarization for each element is shown as a function of shear strain (S_{xy}) in Figure 3.12. Specifically, each cross-polarization magnitude response is taken from the maximum cross-polarization response for each element. This generally occurs at or near the co-polar resonant frequency of the FSS, meaning that in practical applications, only this frequency will have to be measured.

Overall, it appears that grounded FSS elements generally have a stronger cross-polarization response than the equivalent ungrounded FSS designs, even when un-deformed. This behavior can act as both a benefit and a drawback, depending on the desired sensing requirements. On one hand, this higher cross-polarization level (>-20 dB) makes it relatively easy to detect in measurement, which may be a concern for practical implementations of FSS sensors in high loss or electrically noisy environments. Additionally, higher cross-polarization levels can allow simpler and more affordable measurement equipment to be used, rather than a VNA. On the other hand, by having a higher baseline of cross-polarization (i.e. zero shear strain response), the cross-polarization caused by shear strain quickly reaches its highest limit, as was seen for the grounded loaded tripole FSS. While this can be useful for detection of shear strain, it limits the ability of the FSS to characterize the shear strain through cross-polarization magnitude measurements alone. As such, the bandwidth (defined as the range of frequencies between the points that are -3dB from the peak) of the cross-polarized resonant peak will also be needed for characterization of larger shear strains. Furthermore, it may not always be practical to implement a conductive sheet in a structure to act as a ground plane for an associated FSS (particularly for embedded sensing applications). As such, development of a non-grounded FSS element that gives high cross-polarization levels when un-shear strained (without reaching the observed maximum limit too quickly) would be beneficial. Of the elements observed, the element that best fits these criteria is the loaded cross-loop design, shown in Figure 3.11. The co-polarized and cross-polarized responses of this element are displayed in Figure 3.13 (a) and (b), respectively.

Crossed-Dipole FSS   Jerusalem Cross FSS   Cross-Loop FSS   Loaded Cross-Loop FSS

Square Loop FSS   Tripole FSS (Grounded and Ungrounded)   Loaded Tripole (Grounded and Ungrounded)
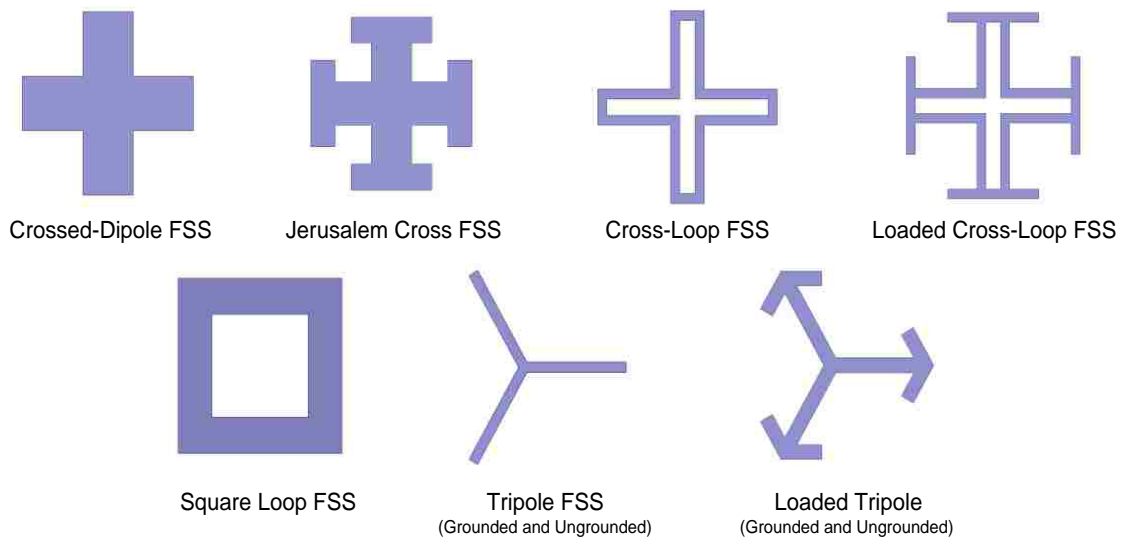
Figure 3.11. FSS elements investigated in Figure 3.12.
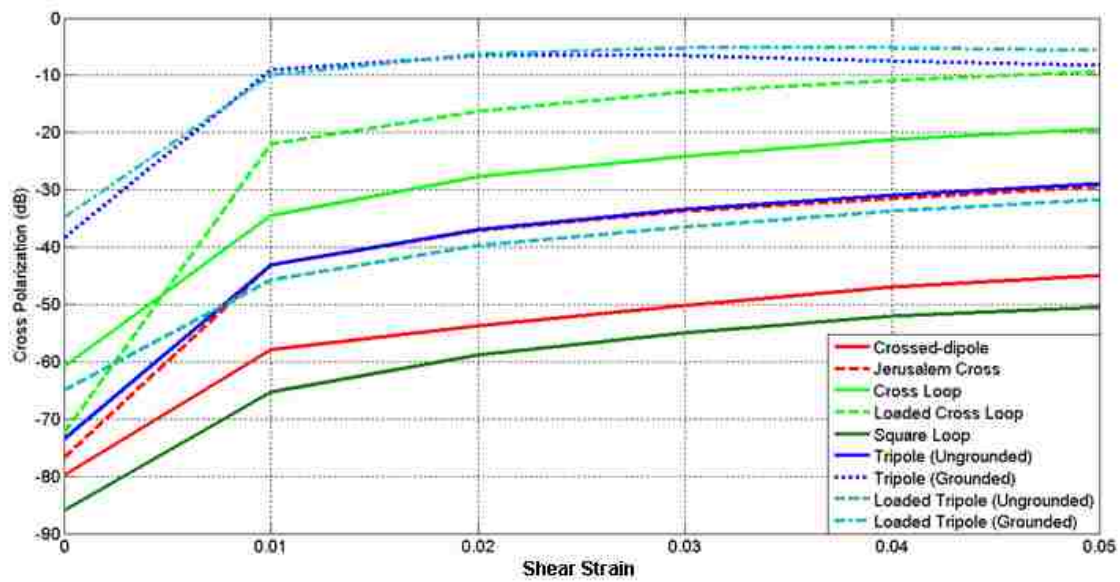
Figure 3.12. Simulated reflection response magnitude of cross-polarization plotted as a function of shear strain for FSS elements of Figure 3.11.
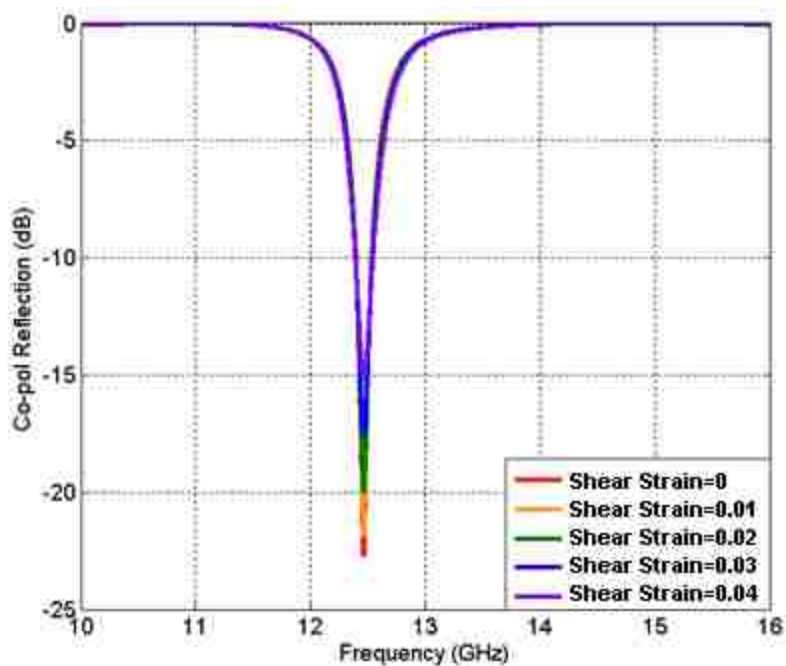
(a)
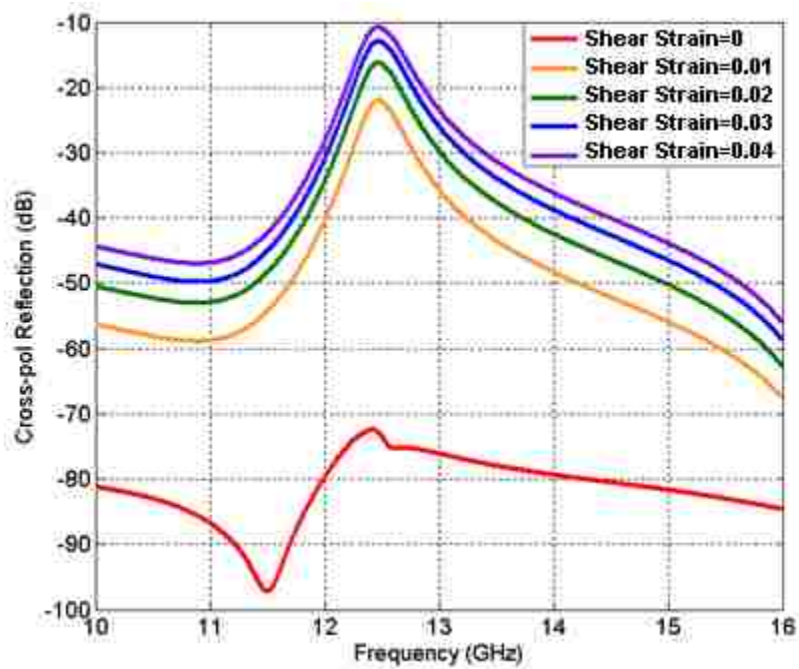
(b)

Figure 3.13. Simulated Co-polarized (a) and cross-polarized (b) frequency response for a Loaded Cross Loop FSS under shear strain.

Based on the results of Figure. 3.13, a number of advantages are observed. First, unlike the ground-backed loaded tripole FSS design response seen in Figure 3.9, the loaded cross loop FSS has a co-polarized reflection response that is essentially unaffected by shear strain. This means that the effects of normal strain and shear strain can be easily distinguished for this FSS, allowing this FSS to be used to sense both deformations simultaneously. Second, this FSS design has a higher cross-polarization level for shear strain than other, non-grounded FSS designs, and is comparable to cross-polarization levels seen for the grounded FSS designs investigated. As such, after ~0.01 shear strain, this peak will be relatively easy to detect in a practical measurement (in which electrical noise or environmental reflections might obscure the FSS response), while also not requiring the presence of a ground plane. As a result, the loaded cross-loop FSS appears to be an excellent candidate for normal strain and shear strain sensing purposes.

3.3. APPLICATION OF FSS FOR STRAIN/SHEAR/BUCKLING DETECTION IN STEEL-TUBE REINFORCED CONCRETE COLUMNS

Thus far, all investigations into the response of FSS to deformations have either been through simulation or controlled lab experiment. To further extend the work, measurements were conducted using a grounded crossed-dipole and square loop FSS that were embedded into a set of steel-tube reinforced concrete columns. These elements were chosen for their straightforward design principles, ease of in-house production, angle insensitivity, and for their strong SHM performance, as shown in the previous sections. Meanwhile, the columns used in this test represent a novel advancement in concrete support structures, and take the form of a hollow, steel-tube core, around which the concrete column is poured [38]. This hollow-steel core acts to reinforce the concrete column, giving it structural stability that is comparable to a solid concrete column, but with reduced weight. Additionally, a fiber-reinforced plastic (FRP) layer surrounds the concrete column, acting as a casing during the pouring of the concrete column, as well as providing a layer of protection from environmental exposure [38]. A cross sectional view of the column structure is shown in Figure 3.14.
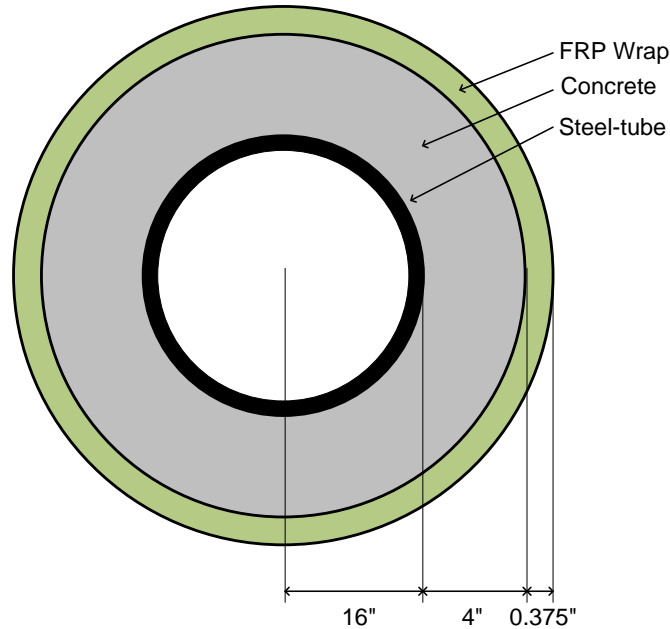
Figure 3.14. Cross-section of concrete column.

To validate the structural integrity of these columns, two structural loading tests were conducted; a lateral displacement test and a torsion test. The lateral displacement test consisted of a vertically oriented concrete column that underwent horizontal displacement at the top of the column. This displacement caused the steel-tube core of the column to undergo significant vertical normal strains (and resultant buckling when the column failed mechanically) due to interactions between the column and the static concrete footing that acts as the column base [38]. Here, buckling is defined as a severe bending of the steel-core due to compressive normal strain. This buckling can weaken the steel, and can thus lead to possible structure failure if not detected. An illustration of the lateral displacement test is shown in Figure 3.15.

The most significant normal strains and subsequent buckling occur near the bottom of the steel-tube core, at the interface between the column and the footing, and located in the direction of lateral displacement. As such, the base of the steel-tube was chosen as the location to apply the FSS sensor, which for this test was the grounded

square loop FSS, which was found in simulation to be the more sensitive of the two FSSs to normal strain. Meanwhile, the torsion test consisted of a vertical concrete column that underwent a twisting force at the top of the column. This twisting force was applied using two linear actuators moving in opposite directions on either side of the column. This twisting caused shear strain to occur along the base of the column due to interactions between the twisted column and static footing. By applying an FSS to the steel column in this region, shear strain can deform the FSS, causing the FSS to cross-polarize incident radiation. The grounded crossed-dipole FSS was chosen for this test, as simulation showed that it was more sensitive to shear strain than the grounded square-loop FSS.
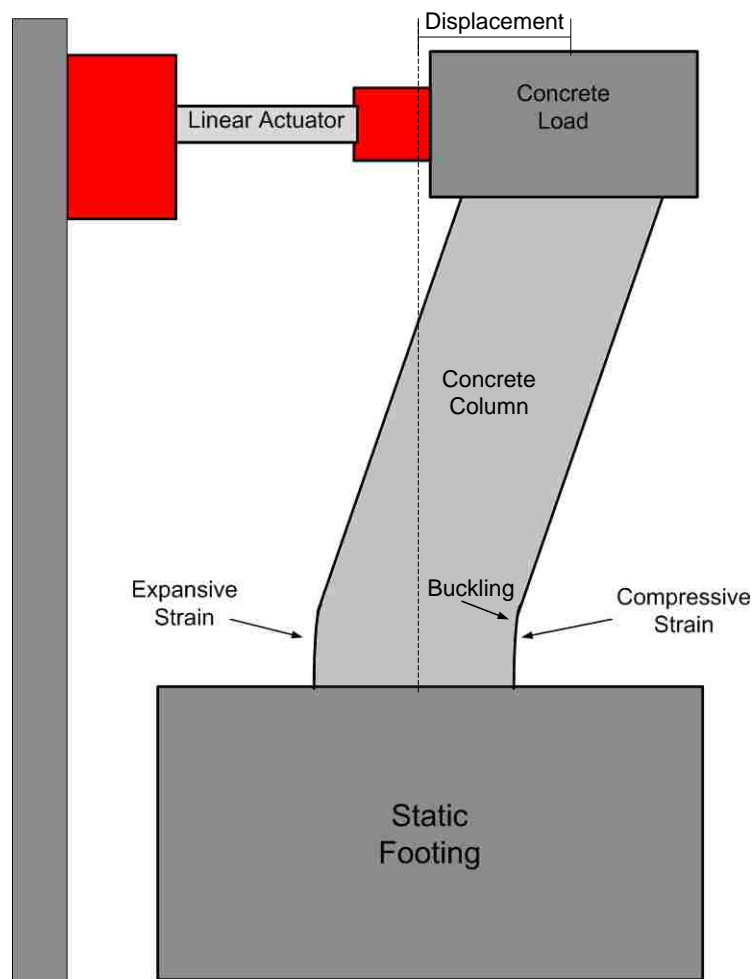
Figure 3.15. Diagram of linear displacement test.

For the purposes of embedding FSS sensors into the above concrete columns, a number of practical considerations had to be made in the FSS design process. Such considerations included the effects of conforming the FSS to the column's curvature, as well as compensation for the effects of loss and internal reflections that occurred within the geometry of the column. The effects of curvature were accounted for by choosing FSS elements that are insensitive to incident angle, with this insensitivity verified by simulation of a curved FSS. As for material considerations, radiation at microwave frequencies experiences significant power loss in concrete due to the concrete's water content (i.e. dielectric loss), making it difficult for interrogating signals to penetrate through the concrete. Additionally, course aggregates in the concrete can cause unintended scattering of incident signal. This results in a reduction in power reflected from the FSS, making these resonances harder to detect. This loss was partially accounted for by designing the FSSs to operate in the S-band (2.6-3.95 GHz), as lower frequencies experience less dielectric loss. Signal reflections within the concrete structure were another concern, as the thickness of the concrete layer was comparable to the wavelength of the interrogating signal. The combined reflections from dielectric boundaries in a layered structure can lead to alterations in the structure's frequency response, such as the creation of resonances based on the thickness of the dielectric layers. As such, the concrete structure may have (inherent) resonant behavior that would mask the FSS resonance [54]. In order to reduce these reflections, a pair of dielectric-filled horn antennas were designed and built for interrogation of the concrete columns. By using a dielectric-filled horn, the impedance of the horn would better match the concrete column, reducing reflections and increasing the power incident on the FSS. Additionally, the apertures of these horns were curved to conform directly onto the columns, as an air gap would be otherwise present for a flat aperture. These horns were manufactured by 3-D printing a dielectric material ($\varepsilon_r = \sim 3$, and nominal loss factor) into the shape of the desired horn and wrapping the dielectric in conductive tape. A photograph of one of the horn antennas is shown in Figure 3.16.

Figure 3.16. Filled horn antenna for measuring FSS embedded in concrete column.

The grounded crossed-dipole and grounded square loop FSS designs used for this investigation were simulated before being built and tested in the lab. Both FSSs were etched onto a thin film of conductor backed Roger's 3006 PCB material having a thickness of 0.25 mm, ε_r of 6.15, and the loss tangent of 0.0015. The frequency response of each sample was measured when flat and when conformed over a curved surface (similar to that of the column) to ensure that the curvature does not adversely affect the FSS's frequency response. Images of the completed grounded crossed-dipole and grounded square loop FSS samples are shown in Figure 3.17 (a) and (b), respectively. Additionally, the measured reflection responses for both the cross FSS and square loop FSS are given in Figure 3.18 (a) and (b), respectively, for both flat and curved contours.

(a)

(b)

Figure 3.17. Grounded crossed-dipole FSS (a) and grounded square loop FSS (b) samples.
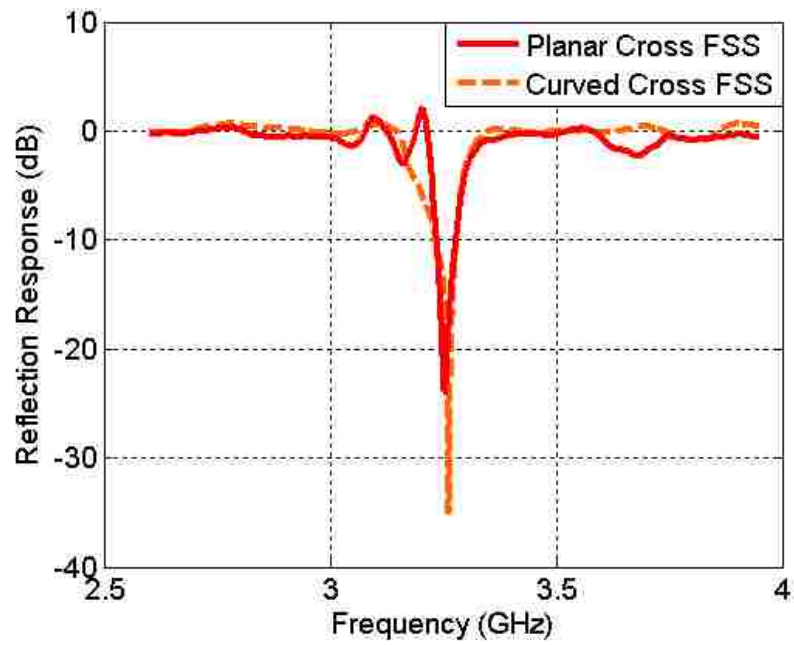
(a)
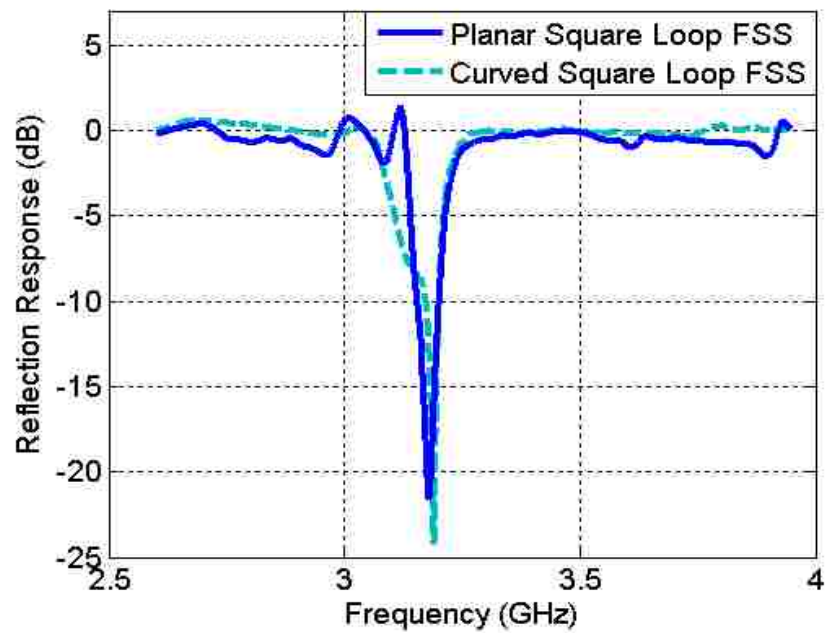
(b)

Figure 3.18. Reflection responses of grounded cross FSS (a) and grounded square loop FSS (b) in planar and curved states.

From the results shown in Figure 3.18, the FSSs were found to have distinguishable resonances at 3.248 GHz (for the grounded crossed-dipole FSS) and 3.174 GHz (for the grounded square loop FSS). Once constructed, the FSS samples were attached to the steel-tube cores of the test columns. The method of attaching the FSS samples was of critical importance, as a poor adhesion could have lead to detachment during deformation. Furthermore, depending on how the FSS was adhered to the structure, deformations on the steel-core potentially may not translate completely to the FSS, thus reducing the sensitivity and effectiveness of the FSS for normal/shear strain sensing. For the purposes of this test, the FSS samples were adhered to the steel-core using 3M Hi-Strength 90 Spray Adhesive. This adhesive was chosen for its high strength and large surface-area applicability. The locations of the FSS samples applied to the steel-tube cores are shown in Figure 3.19.

Figure 3.19. FSS samples applied to steel-tube cores.

For each measurement setup, the dielectric-filled horns were attached to the concrete columns over the locations of the FSS samples. For the lateral displacement test (grounded square-loop FSS sensor), the two horns were oriented to provide a co-polarized frequency response between the horns, as this test was intended to measure normal strain in the FSS. Conversely, for the torsion test (crossed-dipole FSS sensor), the horns were oriented to provide a cross-polarized frequency response to measure shear strain in the embedded FSS. In each test, an external 30 dB amplifier was added to the transmitting port to amplify the interrogating signal to counteract losses (mentioned above) in the concrete column. This system was measured using at S-band (2.6-3.95 GHz) using a calibrated Agilent 8753 VNA.

During the lateral displacement test, the top of the column was displaced positively and negatively, relative to the hydraulic actuator that applied the displacement. This displacement deformed the FSS with both negative (compression) and positive (tension) normal strain. Displacements were applied gradually (in cycles) over the course of the test, in such a way so that the actuator applied increasing displacement with each cycle. During each cycle, the column was positively displaced by a certain amount, and then negatively displaced by the same amount. This was repeated twice for each displacement. The total displacement ranged from 0.05 inches for the first cycles to 15.3 inches of displacement in the final cycles. Measurements of the FSS response were conducted at the positive and negative apexes (maximums) of displacement for the first repetition of each cycle. By observing the difference in resonant frequency between the strained and un-strained FSS for each displacement, the associated strain could be found by dividing the frequency difference by the gauge factor of the FSS (calculated by Equation 3.1 as $\varsigma = \frac{\Delta f}{f_0 * \Delta s}$) [35]. The value of ς for the grounded square loop FSS used in this test was determined through simulation to be 0.43. Based on this value, the measured normal strain for the first cycle of each displacement is shown in Figure 3.20.

For negative displacement, normal strain is relatively small until approximately -3 inches of displacement, at which point the normal strain magnitude increases with displacement magnitude before reaching a plateau at about 0.05 normal strain. Similar behavior is seen for positive displacement, with significant normal strain only occurring after about 6 inches of displacement. After this point, the magnitude of normal strain

increases linearly with displacement until it reaches a value of approximately -0.025 at 13 inches of displacement. These normal strain values are compared to those measured by traditional strain gauges in Figure 3.21 as a verification of the FSS's performance. Two sets of strain gauge data are plotted, corresponding to data taken at the apexes of the two cycles for each displacement. The strain gauge measurements are only reported for displacements between -4 to 4 inches, due to limitations in the strain gauges.
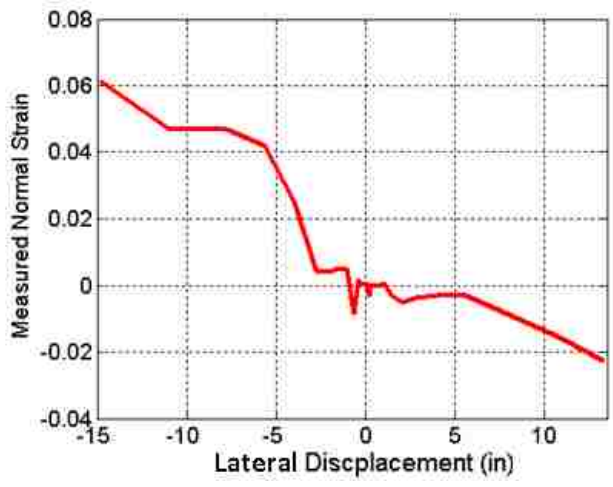
Figure 3.20. Normal strain measured from FSS as a function of displacement.
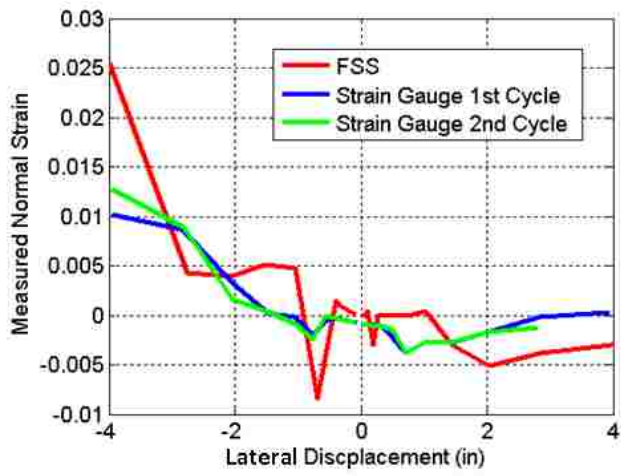
Figure 3.21. Comparison of normal strain data from FSS and strain gauge sensors.

Overall, there is good agreement between the FSS and strain gauge, with minor aberrations in the FSS data set occurring for displacements around zero. These aberrations may be a result of the measurement not taking place at exactly at the apex of each displacement cycle due to the non-instantaneous measurement time of the VNA, as well as human error in timing the measurement with the apex of the strain cycle. This would have the most significant effect for small displacement cycles, as these cycles occurred more quickly in the testing process than the larger displacement cycles. Additionally, for the larger displacement values, normal strains measured by the FSS are larger in magnitude than those measured by the strain gauges. This may be due to the simulated gauge factor not exactly matching that of the physical FSS sample. A similar behavior was observed for the FSS measurements shown in Figure 3.6 of Section 3.1, which could indicate that a more reliable gauge factor determination method may be needed that takes the effects of Poisson's Ratio into account.

For the torsion test, a testing procedure similar to the linear displacement test was conducted. In this test, torsion was applied to the column through a set of linear actuators connected to the top of the column. Torsion was applied in cycles, with the column first being twisted clockwise and then counter-clockwise for each cycle. Furthermore, the magnitude of this twisting increased with each additional cycle. Measurements of the cross-polarized FSS response were taken at the apex of each cycle, with the goal of detecting increases in cross-polarization due to torsion-applied shear strain of the FSS. Unfortunately, however, no change was detected in the cross-polarized response over the course of the test. This may indicate that shear strain was not applied to the FSS as expected, meaning that cross-polarization would not have occurred. This could be due to the column not deforming as expected, or due to shear strain not correctly transferring to the FSS. Alternatively, the returning signal may have been below the noise floor (~ -70dB) of the VNA. In either case, the ability of an FSS to detect shear strain was not verified in this investigation, and therefore requires additional investigations including improved test and measurement procedures.

3.4. CONCLUSION

Over the course of this section, the use of FSS for detecting deformations in a structure was discussed. In Section 3.1 and 3.2, the effects of normal strain and shear strain on the frequency response of an FSS were examined through both simulation and measurement of deformed FSS samples. In Section 3.1, it was found that the resonant frequency of an FSS shifts when under normal strain due to normal strain changing the length of the FSS element and altering the resonant wavelength. Additionally, it was shown that this resonant shift was also a function of the polarization of the interrogating wave with respect to the direction of normal strain. Specifically, the effect of normal strain on resonant frequency was greatest when the incident wave polarization and normal strain direction were parallel. Based on these observations, FSSs were shown to have potential to sense both normal strain magnitude and normal strain direction. To verify these observations, an FSS sample that had been subjected to normal strain was measured for different polarizations. Although overall trends matched expectations (resonant frequency shifting as a function of normal strain), the magnitude of this shift was less than was seen through simulation. Additionally, for incident wave polarizations oriented normal to the direction of normal strain, resonant frequency shifts were greater than expected. Ultimately, these results indicate potential limitations for normal strain sensing (possibly due to the effects of Poisson's Ratio) that may require future investigations, as well as the need for a secondary method of measuring normal strain such as commercial strain gauges for comparison.

For the case of shear strain in Section 3.2, simulations indicated that shear strain causes an FSS to cross-polarize incident radiation due to the FSS losing geometrical symmetry. The magnitude of this cross-polarization was found to increase with shear strain, resulting in a potential method for detecting shear strain. The sensitivity of a number of FSS elements to shear strain was analyzed for sensing purposes. This study indicated that while grounded FSS designs caused the highest level of cross-polarization for a given shear strain, the cross-polarization would quickly reach an observed maximum value, meaning that cross-polarization magnitude would cease to increase for higher shear strains. Of the non-grounded elements, the loaded cross-loop FSS was found to provide the most sensitive response to shear strain, giving the highest magnitude

of cross-polarization of the non-grounded elements examined while also avoiding a maximum limit for the simulated shear strain values. Unfortunately, for the case of shear strain, laboratory measurements were not conducted due to the difficulty in applying shear strain to the available FSS sample. As such, future work will need to be undertaken to conduct such a measurements, thus providing validation of simulated results.

Finally, in Section 3.3, FSS samples were embedded into a set of concrete columns to act as normal strain and shear strain sensors during lateral displacement and torsion tests of these columns. This project provided examples of difficulties that might be encountered for FSS sensing in practical structures. For the structures used in this project, one such difficulty regarded the high signal loss of the concrete, as this loss heavily dampened the interrogating signal, making detection of the FSS problematic. This loss was counteracted by using an amplifier on the interrogating signal, as well as reducing the noise floor of the VNA used during measurement (at the cost of longer acquisition times). Another difficulty was due to the thickness of the concrete columns causing additional resonances in the measured frequency response due to reflections at dielectric interfaces within the layered dielectric structure of the column, masking the resonance of the FSS. This was (partially) counteracted by using dielectric-filled horn antennas to measure the FSS, as these horns would reduce reflections by matching the impedance of the columns. Finally, the curvature of the columns meant that the FSS samples used for this project had to be designed with such curvature in mind. For the lateral displacement test, a shift in resonant frequency was observed for applied normal strain, as expected from results found in Section 3.1. Furthermore, the normal strain measured by the FSS matched well with traditional strain gauges that were also embedded in the column. However, for the torsion tests, no cross-polarization was detected for over the course of the test. This may have been due to shear strain not being applied to the FSS, or due to shear strains not causing the FSS to cross-polarize incident radiation as expected. As such, future work will need to include additional investigations into the effects of shear strain on FSS samples, likely under more controlled circumstances to ensure that the FSS samples have shear strain applied as expected.

4. APPLICATIONS OF FSS FOR DELAMINATION/DISBOND SENSING

In Section 3, it was shown that geometrical deformation of an FSS affects the FSS's frequency response. Conversely, by (remotely) monitoring the FSS's frequency response, the presence of a deformation may be determined. Further, as discussed in Section 2, an FSS's frequency response is also affected by materials (e.g., dielectrics) surrounding the FSS, providing another potential sensing application. In this section, this material dependency is utilized for detection of separations (i.e., delaminations and disbonds) between layers of a layered dielectric structure.

4.1. FSS RESPONSE TO DELAMINATION WITHIN A STRUCTURE

The formation of delaminations and disbonds in a layered dielectric structure may lead to structural failure, giving rise to the need for delamination/disbond detection. A delamination is defined as a separation that occurs in a laminated material, such as a composite structure [43]. Alternatively, a disbond is defined as a form of delamination composed of a separation between two separate materials that had previously been bonded together. In either case, this separation creates an air gap in the structure that can lead to structural failure. Therefore, the ability to sense the presence of delaminations/disbonds is critical for assessing structural integrity. Current delamination/disbond sensing techniques include ultrasound [42], thermography [40], and microwave interrogation [41]. In addition to these methods, FSSs may also be used for delamination/disbond detection by taking advantage of their sensitivity to dielectric materials in the vicinity of the FSS [54].

As discussed in Section 2.2, the frequency response of an FSS is sensitive to the presence of surrounding materials including (mechanically supportive) dielectric substrate layers. This occurs due to the dielectric material altering the capacitive coupling that occurs between elements of the FSS, thus changing the FSS's resonant frequency. Normally, when integrating an FSS into a layered dielectric structure, the design of the FSS (element spacing, etc.) must be adjusted to account for this additional capacitance. Thus, the FSS is "tuned" to provide a specific response for a particular dielectric structure. However, should the dielectric structure change due to the presence

of a delamination in the structure, the FSS capacitance will be reduced. When this occurs, the resonant response of the FSS is changed as well.

4.1.1. Simulation Results. To investigate how the FSS resonance is affected by delamination, a full-wave simulation in HFSS [23] was conducted for a crossed-dipole FSS embedded between two planar dielectric sheets having a permittivity of 3.3, loss tangent of 0.004, and thickness, t, of 1.524 mm. The delaminated structure and embedded crossed-dipole FSS used for this simulation are shown in Figure. 4.1 (a) and (b), respectively. Meanwhile, the resultant frequency response for three different delamination distances are shown in Figure. 4.2.

(a) (b)
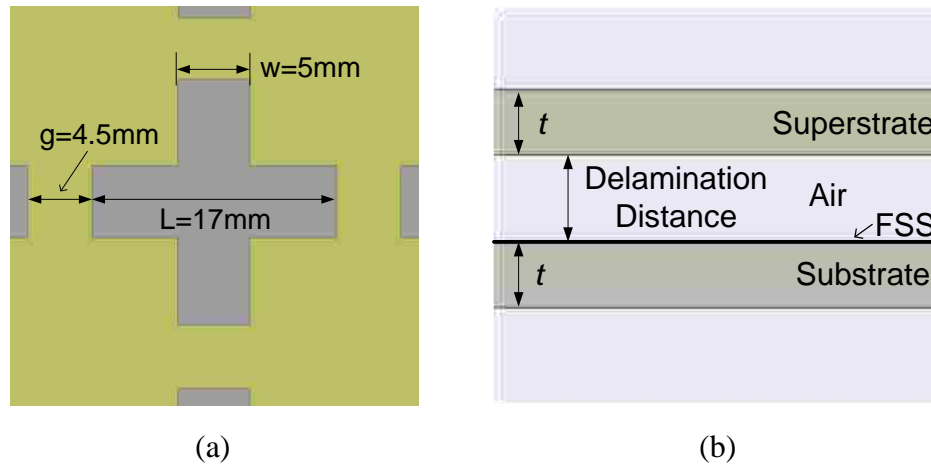
Figure 4.1. Crossed-dipole FSS (a) embedded into a delaminated structure (b).
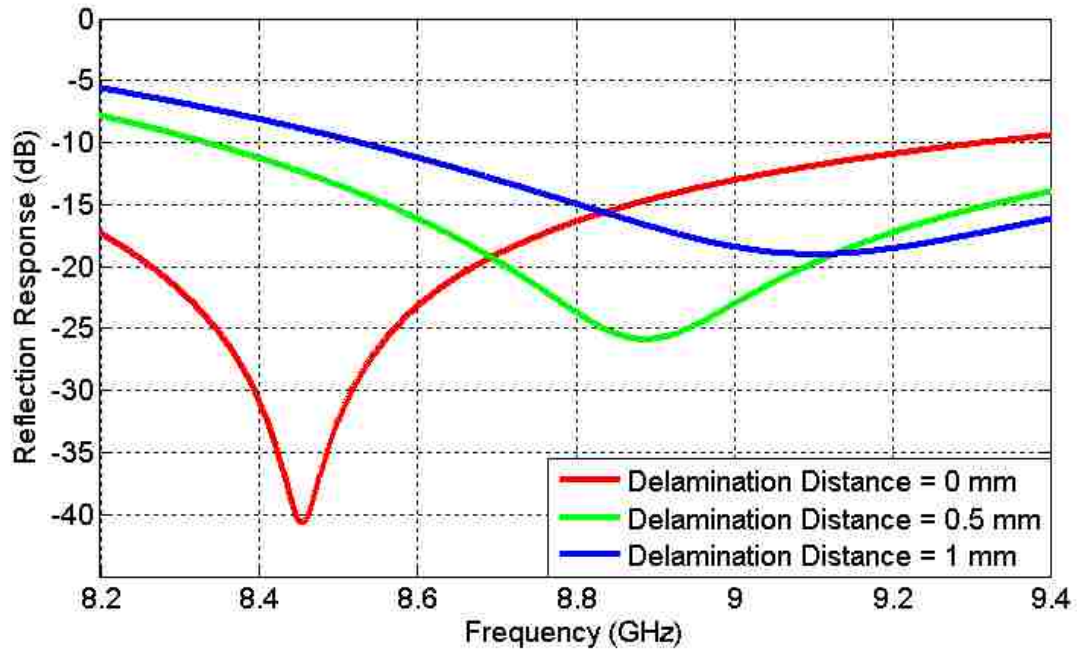
Figure 4.2. Reflection response of the embedded crossed-dipole FSS of Figure 4.1 for three delamination distances.

From these results, a number of observations can be made. First, Figure 4.2 shows that both the resonant frequency and resonant depth of the FSS response are altered when a delamination is present. The resonant frequency (f_0) shifts because it is inversely proportional to both the FSS capacitance (C) and inductance (L), calculated as

$$f_0 = 1/(2\pi LC) \tag{4.1}$$

Since the FSS's capacitance decreases as the delamination distance increases while the inductance remains constant, the resonant frequency increases accordingly. Furthermore, the resonant depth changes due to the reflections generated as a result of the additional interfaces (dielectric-air and air-dielectric) caused by the delamination within the structure. These additional reflections coherently add to the total received signal, potentially causing a change in the depth of the resonance (in this case, the depth was

reduced). As such, by monitoring both parameters, one can acquire two sets of data from which delamination information (such as severity and location) may be obtained. Additionally, the sensitivity of both resonant frequency and resonant depth to delamination can help differentiate the effects of delamination from other structural deformations of sensing interest, such as normal strain, which only affects resonant frequency. In other words, in a system where both normal strain and delamination may occur, a significant change in both resonant frequency and depth may indicate the presence of delamination, whereas observing only a shift in resonant frequency may be indicative of normal strain alone. As a result, a single FSS can conceivably be used to separately detect both normal strain and delamination (as well as shear strain, potentially, since shear strain doesn't typically affect the co-polarized frequency response, as discussed in Section 3.2). This gives a single FSS the potential to act as a comprehensive distributed structural health monitoring sensor. One limitation with this method is that it may be difficult to separately quantify normal strain and delamination if both are present. However, the presence of a delamination can often be considered a major structural failure [43]. As such, normal strain assessment may no longer be important in this case, since the structure has already reached a critical failure state due to the delamination. That being said, by better characterizing how delaminations affect an FSS's frequency response, it may still be possible to separately quantify these two phenomena. To this end, the resonant frequency and resonant depth of the FSS-integrated layered structure from Figure 4.1 are shown as a function of delamination distance in Figure 4.3 (a) and (b), respectively.

From Figure 4.3, it is seen that for thin delaminations (less than 2 mm), the resonant frequency monotonically increases as the delamination distance increases. Additionally, for very thin delaminations (less than 0.2 mm), the increase in resonant frequency occurs more rapidly than for the slightly larger delaminations (0.3 mm - 2 mm). This is because the capacitive electric field coupling of the FSS is concentrated close to the FSS surface. As such, changes in a dielectric that occur farther from an FSS have less of an effect on the resonance, since less of the electric field coupling is present in that region. This behavior is further discussed later in this section.
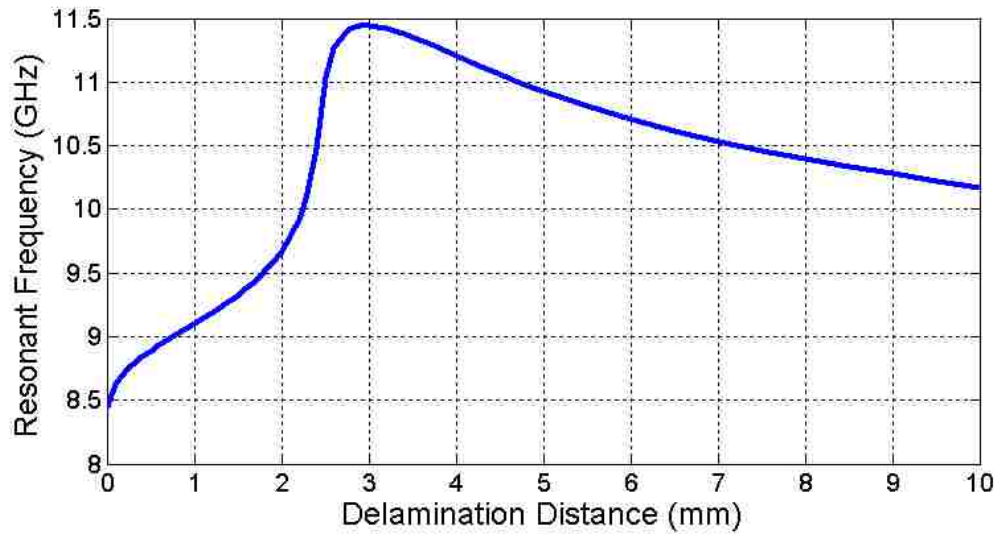
(a)
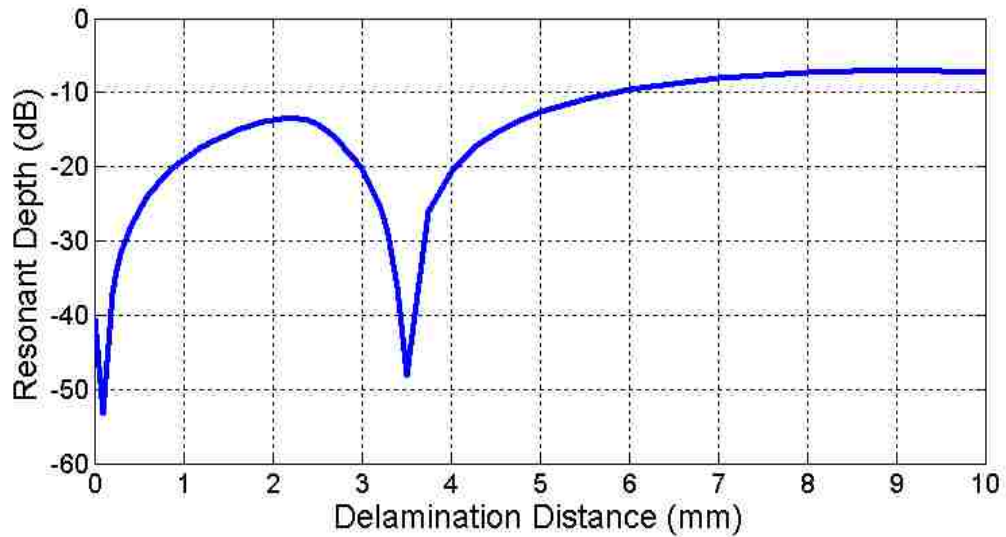
(b)

Figure 4.3. Resonant frequency (a) and resonant depth (b) of the embedded crossed-dipole FSS shown in Figure. 4.1 as a function of delamination distance.

The results of Figure 4.3 (b) show a similar trend for the relationship between resonant depth and thin delaminations. For instance, when a delamination is very thin

(less than 0.1 mm) the resonance becomes slightly deeper. This is likely due to the newly formed air gap changing the overall structure (effective) impedance to be closer to that of the surrounding environment (in this case, free space) and therefore reducing reflections at the resonant frequency. Next, as the delamination distance increases, the resonance becomes heavily dampened due to additional reflections in the structure (introduced by the new interfaces created by the delamination), with the reflection resonance becoming most shallow at ~2.5 mm of delamination. For the 2 mm - 5 mm delamination range, however, the trends in resonant frequency and depth become reversed. After reaching a peak value in resonant frequency of 11.5 GHz at 3 mm of delamination, the resonant frequency reduces to 11 GHz at 5 mm of delamination. Additionally, the observed reflection resonance quickly deepens again at 3.5 mm of delamination, reaching a depth of -50 dB, before eventually returning to a shallower level as delamination distance continues to become larger. This is likely due to a resonant frequency (inherent to the delaminated dielectric structure) that is near the resonant frequency of the FSS. To illustrate this, the resonant frequencies of the dielectric structure itself (without an embedded FSS) are shown with respect to delamination distance in Figure 4.4.
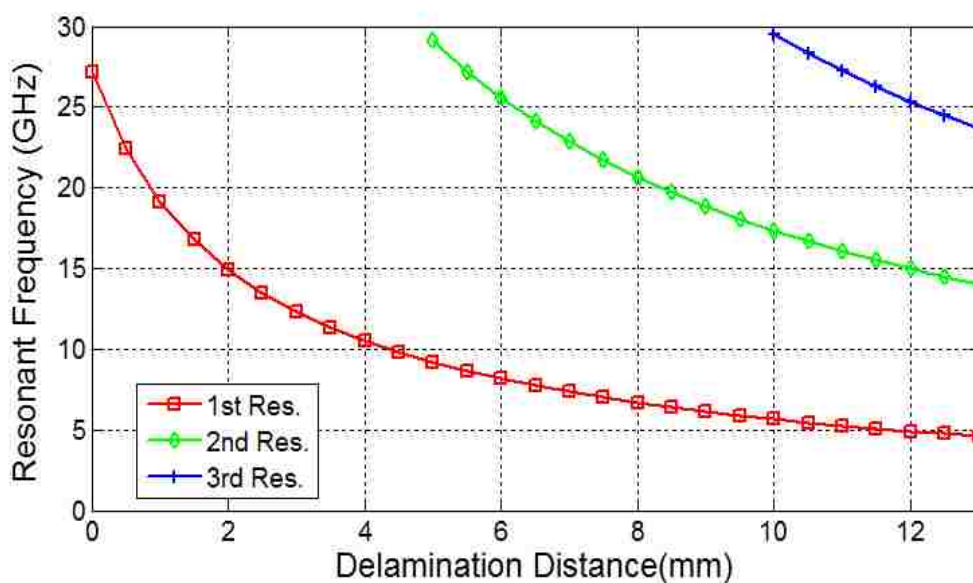
Figure 4.4. First three resonances of dielectric structure given in Figure 4.1 (b) as a function of delamination distance.

From the results of Figure 4.4, it can be seen that at approximately 2.5 mm of delamination, the first resonance of the dielectric structure begins to approach the resonance of the FSS. Since the FSS resonance is most shallow at this point, the dielectric resonance dominates the overall reflection response. Qualitatively speaking, since the dielectric resonance is stronger, the overall resonant frequency is weighted by this resonance. Furthermore, the deeper resonance for 2.5 mm of delamination in Figure 4.3 (b) occurs approximately where the dielectric resonance overlaps the overall resonance, causing the resonance to reach its deepest point. However, as the structure's resonance continues to decrease in frequency for increasing delamination, the structural and FSS resonances no longer overlap. As such, the overall resonance is dampened again as the delamination distance continues to increase.

Another aspect to consider is the influence of delamination location on the FSS response. Thus far, the delaminations have occurred at the interface of the FSS. Since an FSS is more sensitive to dielectric changes that occur locally, delaminations occurring at other locations within a structure may have a reduced effect on the FSS response. To investigate this, full-wave simulations were conducted for the structures shown in Figure 4.5 (a) and (b), referred to as the "Near" delamination case (at the location of the FSS) and "Adjacent to" delamination case (at the next dielectric interface (1.524 mm) from the FSS), respectively. The FSS design used here is identical to the FSS in Figure 4.1 (a). Additionally, the dielectric layers used have the same parameters as those found in Figure 4.1 (b).

The resonant frequency and resonant depth of the FSS as a function of delamination distance are shown in Figure 4.6 (a) and (b), respectively, for the "Near" and "Adjacent to" delamination cases. Additionally, the resonant frequency of the standalone dielectric structure (without an embedded FSS being present) is also included in Figure 4.6 (a).

(a)   (b)
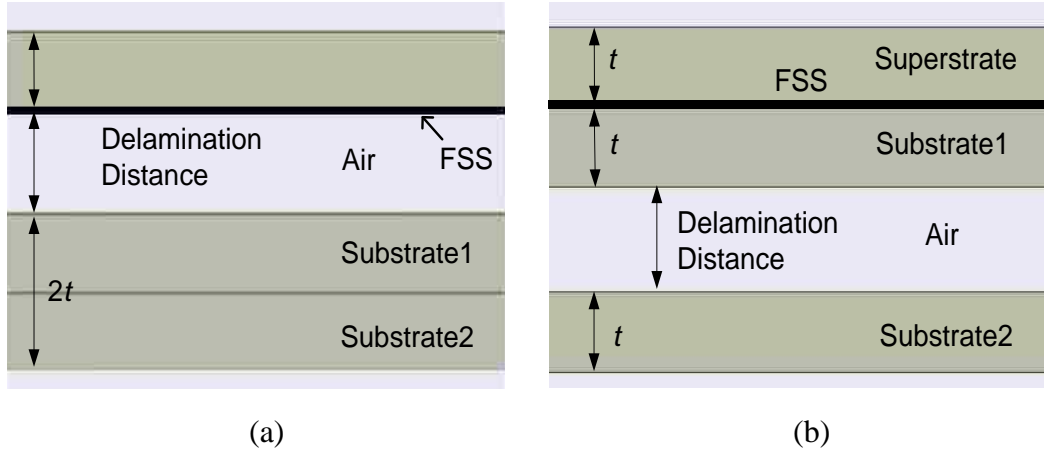
Figure 4.5. Dielectric structures for "Near" delamination (a) and "Adjacent to"
delamination (b) cases.
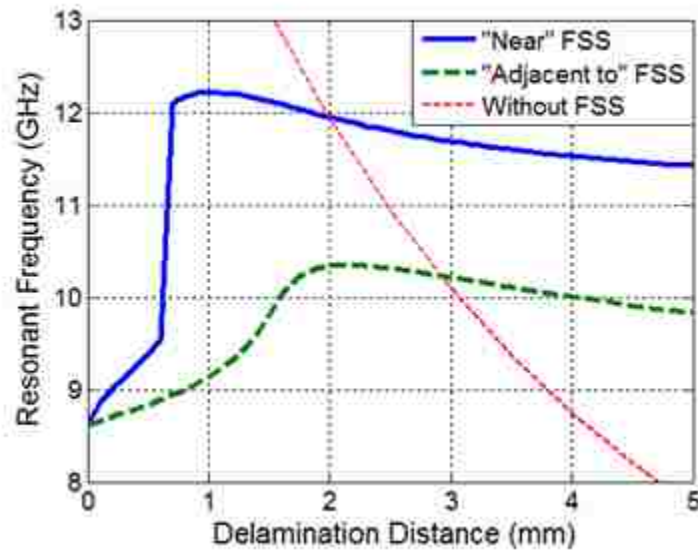
(a)

Figure 4.6. Resonant frequency (a) and resonant depth (b) of the crossed-dipole
FSS in Figure 4.1 as a function of delamination distance for the "Near" and "Adjacent to"
delamination cases illustrated in Figure 4.5.
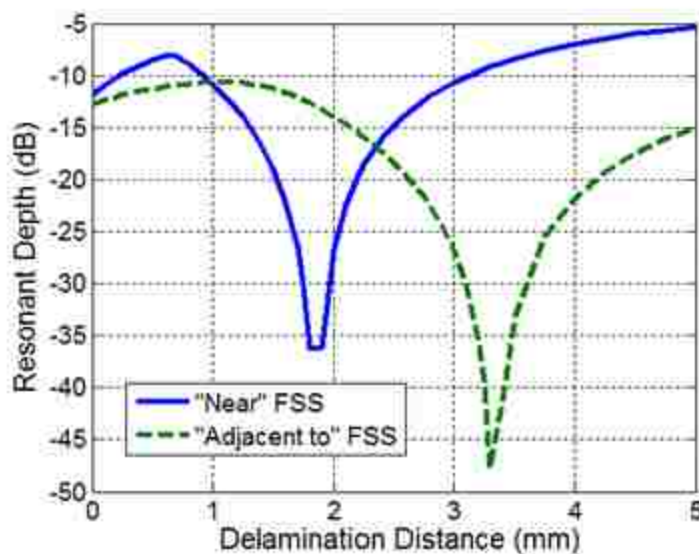
(b)

Figure 4.6. Resonant frequency (a) and resonant depth (b) of the crossed-dipole FSS in Figure 4.1 as a function of delamination distance for the "Near" and "Adjacent to" delamination cases illustrated in Figure 4.5. (cont.)

Overall, similar trends to what was seen in Figure 4.3 (in regards to a delamination occurring at the FSS location, albeit in different dielectric structures) are also seen here in Figure 4.6, with the FSS resonance initially dampening while shifting upward in frequency, before eventually interacting with the resonance of the delaminated dielectric structure (red line in Figure 4.6). However, the resonant frequency is less affected for the "Adjacent to" case than for the "Near" delamination case. This is attributed to the "Adjacent to" delamination case having less of an effect on the FSS's capacitance than the "Near" delamination case, since capacitive coupling occurs close to the FSS. Additionally, since the resonant frequency doesn't shift as much for the "Adjacent to" case as for the "Near" case, a thicker delamination (and thus lower resonant frequency for the dielectric structure) is required before the dielectric structure and FSS resonances overlap and interact, which occurs for this case at approximately 3 mm of delamination.

For delamination sensing purposes, these observations imply that a single FSS may only be able to sense delaminations within its local area. Delaminations occurring farther away have a reduced impact on the frequency response of the FSS. For larger dielectric structures, this may be a problem, as a single FSS may not be able to adequately monitor the entire structure. As such, the use of multiple FSSs embedded throughout the structure may be required for complete sensing coverage. However, in order to include multiple FSS layers in a structure, a number of design considerations must be included [30]. First, to differentiate the resonances of the different FSS layers, the resonant frequencies of each layer must be spaced far enough apart in frequency to avoid unwanted interactions between resonances. As a result, the response of each individual FSS can be separately monitored. Conversely, however, the resonances must be close enough together to all fit within the operating frequency band (potentially requiring a wideband interrogation system). As a result, there may be a limit to how many resonances can be used to monitor a structure. Finally, the spacing between FSS layers in the structure must be carefully chosen. For instance, if the FSS layers are spaced too far apart, there may be "blind spots" in the dielectric structure where a delamination won't be detected due to its distance from the FSS layers. Alternatively, if the FSS layers are too close together, the layers may electrically couple and affect/change their intended response [30].

With the above observations in mind, a full-wave simulation was conducted to investigate how multiple FSSs embedded within a dielectric structure respond to delaminations occurring between different layers of the structure. For this investigation, two FSSs were embedded in the structures shown in Figure 4.8 (a-e), where each structure represents a different delamination location (referred to as Delams 1-5). The crossed-dipole FSS shown in Figure 4.1 was used for the first FSS layer, while the cross-loop FSS design shown in Figure 4.7 was used for the second FSS layer. The transmission response resonant frequencies for each FSS are given in Figure 4.9 for each delamination as a function of delamination distance. The transmission response was considered here in order to take advantage of the two transmission resonances of the cross-loop FSS. The lowest and highest resonant frequencies, 3.6 GHz and 8.5 GHz for no delamination (delamination distance of zero in Figure 4.9) correspond to the cross-

loop FSS, while the middle resonance, 6 GHz for no delamination, corresponds to the crossed-dipole FSS. Meanwhile, the transmission response resonant depths of each FSS resonance are given in Figure 4.10 as a function of delamination distance for each delamination scenario of Figure 4.8.
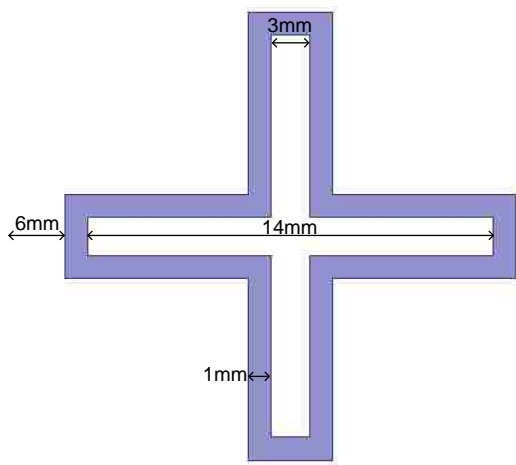
Figure 4.7. Cross Loop FSS used in multi-layer FSS structure for delamination analysis in Figure 4.8.
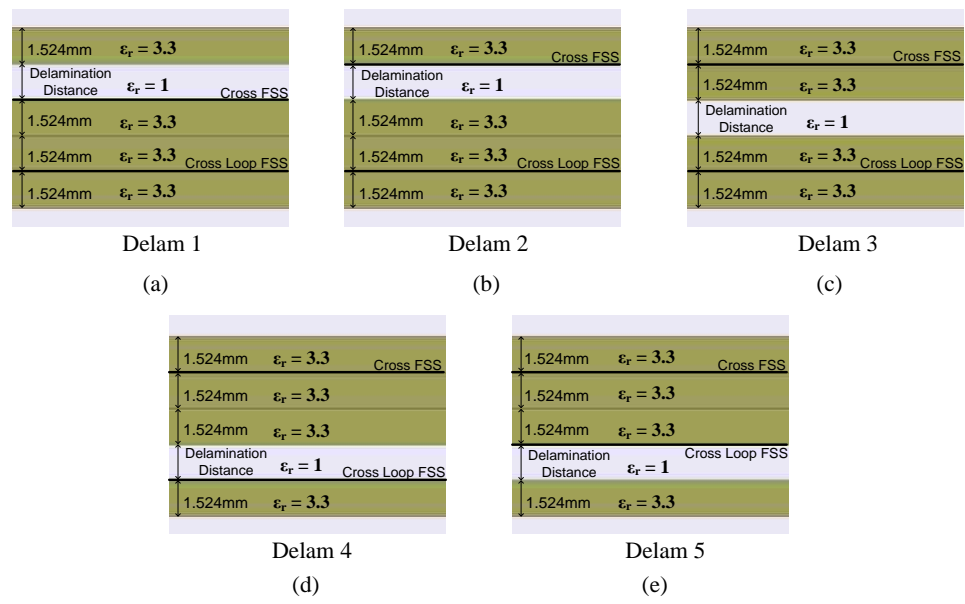
Figure 4.8. Simulated delaminated dielectric structures, referred to as Delams 1-5.
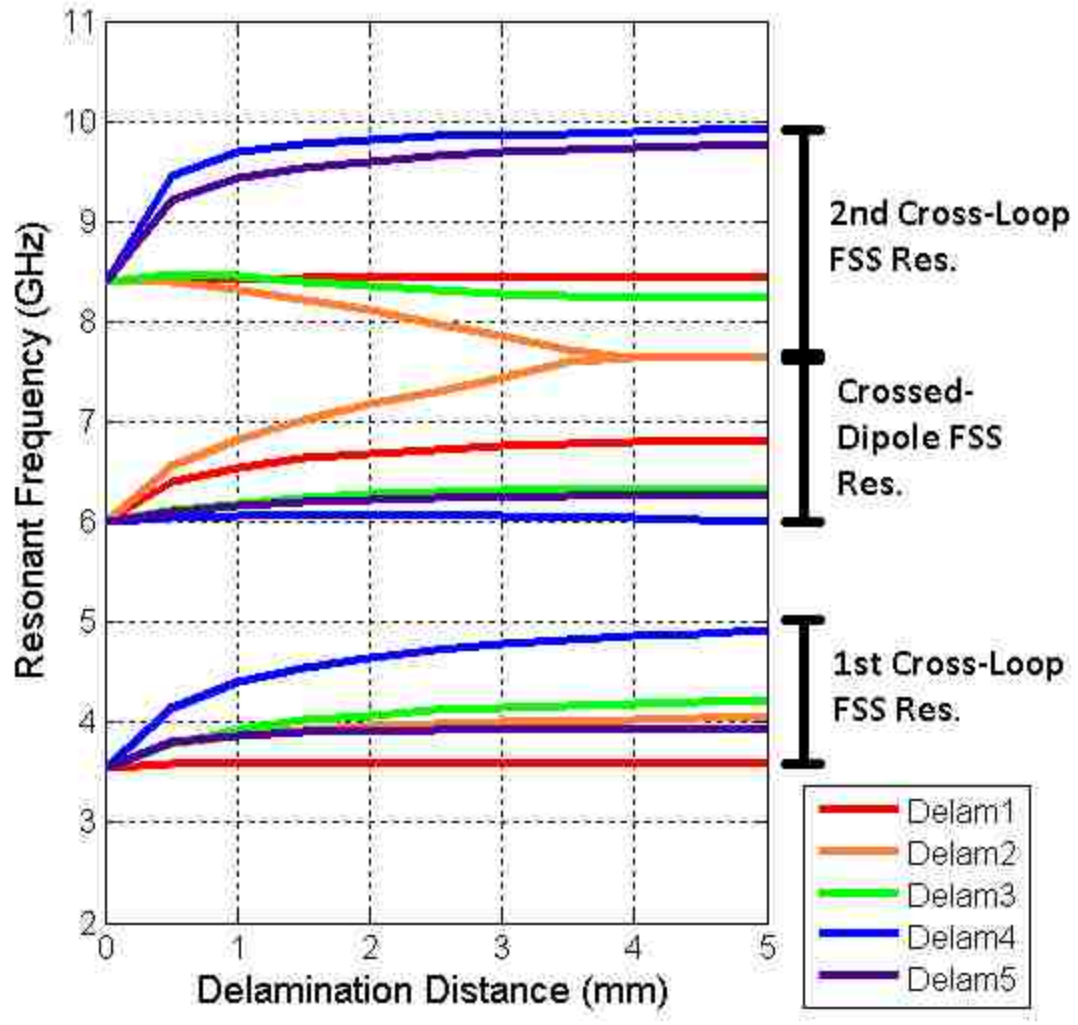
Figure 4.9. Simulated resonant frequencies as a function of delamination distance for Delams 1-5 shown in Figure 4.8. The top and bottom resonances correspond to the cross-loop FSS, while the middle resonance corresponds to the crossed-dipole FSS.
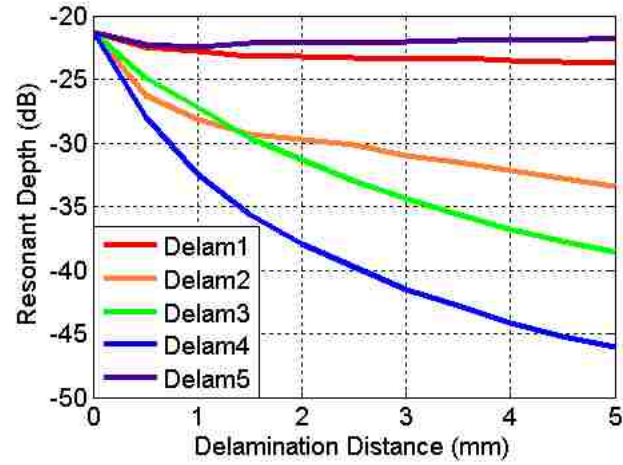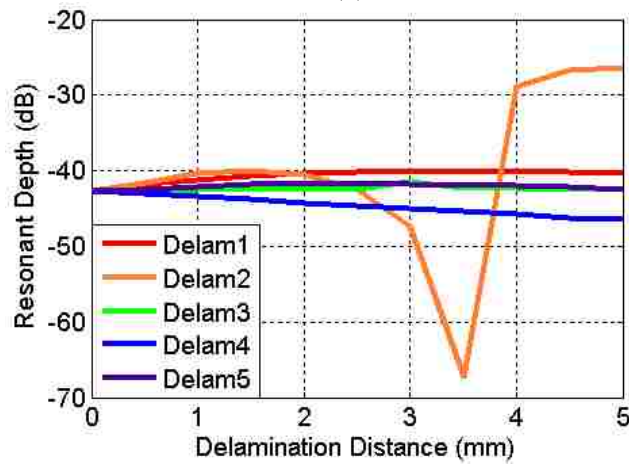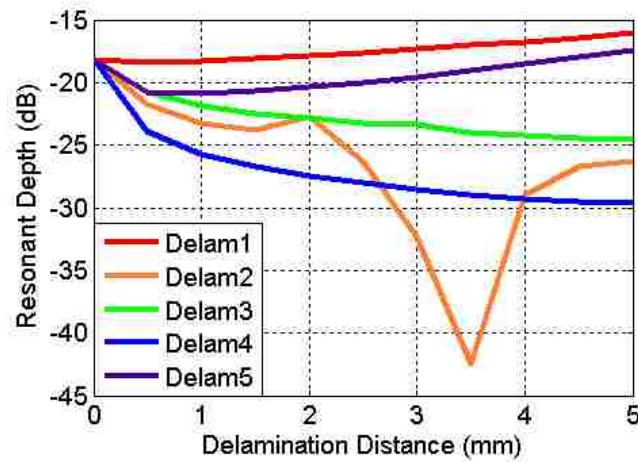
Figure 4.10. Simulated values of resonant depth as a function of delamination distance for Delams 1-5 (Figure 4.8). (a) and (c) correspond to the cross-loop FSS and (b) corresponds to the crossed-dipole FSS

Based on these simulations, Delams 1-5 affect each FSS resonance differently. For Delam 1 in Figure 4.8 (a), the resonance of the crossed-dipole FSS shifts by about 1 GHz, while the resonances of the cross-loop FSS are less affected, shifting by less than 0.1 GHz. This behavior verifies that an FSS is only sensitive to local delaminations, as only the crossed-dipole FSS resonance is significantly affected by Delam 1. The crossed-dipole FSS resonance also shifts in resonant frequency for Delam 2 (shown in Figure 4.8 (b)), shifting by 1.6 GHz over the delamination distance observed. This shift in resonant frequency is greater than what was seen for Delam 1, despite both delaminations being in the same proximity to the crossed-dipole FSS. This increase in delamination sensitivity is also observed in the second resonance of the cross-loop FSS, which exhibits a much larger frequency shift than was seen for Delam 1. This increase in sensitivity for both resonances may be due to additional electric field coupling between the FSS structures that is weakened by the presence of the delamination, reducing the capacitance of both FSSs. Furthermore, the crossed-dipole and second cross-loop FSS resonances begin to overlap after 3.5 mm of delamination distance, creating a single resonance. For practical purposes, such an overlap may be undesirable, as this makes it difficult to independently track the resonance of each FSS. However, 3.5 mm of delamination would likely have already caused the structure to fail, meaning that delamination sensing would no longer be a concern. As such, knowing the maximum required delamination distance for a given structure is important when choosing the multi-layer FSSs' resonance spacing in the overall frequency response. Additionally, this combination of resonances causes a substantial increase in resonant depth at 3.5 mm of delamination distance, before subsequently reducing as the delamination continues to widen. For all other delaminations, the resonant depth does not include the erratic changes seen for Delam 2, as these delamination cases don't cause resonance overlap. For Delam 3, shown in Figure 4.8 (c), all three resonances exhibit a similar frequency shift. This similarity in frequency shift between resonances occurs because Delam 3 is spaced directly between the two FSS layers, thereby affecting each FSS in a similar way. Next, for Delam 4 in Figure 4.8 (d), the cross-loop FSS resonances are each altered by ~1.5 GHz over the observed delamination distances, while the crossed-dipole FSS resonance is largely unaffected. Much like the resonant responses to Delam 1 and Delam 2, this behavior is a

result of the close proximity of Delam 4 to the cross-loop FSS, again demonstrating the local sensitivity of an FSS to delamination. Lastly, similar behavior is also seen for Delam 5 in Figure 4.8 (e), albeit with less shifting in the cross-loop resonances. This behavior mirrors the difference in delamination response seen between Figure 4.8 (a) and (b), where the delaminations occurring between the two FSS layers cause a more significant impact on the frequency response than delaminations occurring between the FSSs and the outermost dielectric layers. One final observation is that unlike for the reflection response in Figure 4.4, the transmission response doesn't feature a dielectric structure resonance. A selection of transmission responses for the delaminated structures of Figure 4.8 (without FSSs) are shown in Figure 4.11.
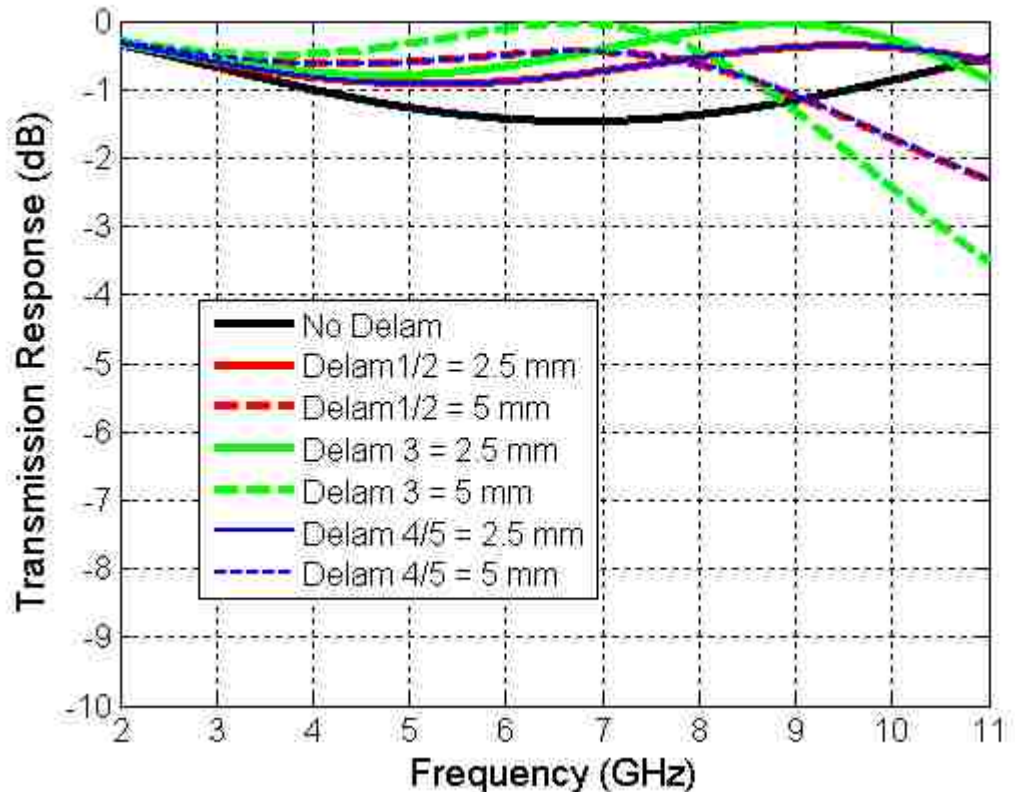
Figure 4.11. Transmission responses for the structures shown in Figure 4.8, without embedded FSSs.

As Figure 4.11 indicates, the transmission responses for the delaminated structures in Figure 4.8 don't vary significantly over the observed frequency spectrum, (the largest variation is less than 4 dB for the 5 mm Delam 3 case). As a result, instead of being altered by structural resonances, the resonant depths of each FSS resonance change smoothly with delamination distance, as seen in Figure 4.3 (b). This is beneficial from a sensing point-of-view, as the presence of a delamination is the only aspect that causes a change in resonant response. Additionally, measuring the transmission response may prove advantageous should structural resonances mask the FSS resonances in the reflection response. However, transmission measurements may be impractical in some real world sensing cases, as both sides of a structure (required for transmission measurements) may be inaccessible. Overall, based on these preliminary results, the use of multiple FSS layers for delamination detection appears quite promising, as this method can provide remote, non-contact delamination monitoring for an entire structure, while also providing information on delamination location.

4.1.2. Measurement Results. To verify the ability of embedded FSSs to detect the presence of delaminations, a series of measurements were conducted on layered dielectric samples with embedded FSSs. The FSSs used for these measurements were the crossed-dipole FSS shown in Figure 4.1, and the cross-loop FSS shown in Figure 4.7. These samples were constructed through chemical etching of 8"x11" copper-clad Rogers RO4053 PCB boards (1.524 mm thick, permittivity of 3.3 and loss tangent of 0.004), as was used in simulation. Although these FSS samples are not infinite in extent (as is assumed in simulation), all but the outermost FSS elements will contribute to an FSS response that is similar to the ideal (infinite dimensions) case, as most coupling only occurs with directly adjacent elements. Furthermore, the size of the FSS sample was larger than the interrogating beam, thus avoiding significant edge effects. The copper cladding was removed from two additional Rogers RO4053 boards to serve as additional dielectric layers. The FSSs and dielectric layers were arranged in 5-layer stackups corresponding to the arrangements seen in Figure 4.1 (b), Figure 4.5, and Figure 4.8 (a-e). To replicate delaminations, 0.5 mm spacers were placed between the appropriate dielectric layers, creating an air gap with a controlled thickness. The frequency responses of each of the stackups were measured using two horn antennas connected to two ports of

a calibrated 8510C Vector Network Analyzer (VNA). During measurement, each stackup was placed in a semi-anechoic chamber to reduce environmental noise. For each delamination case, several sets of measurements were conducted to mitigate possible variations in the measurement setup, as well as to demonstrate reproducibility of the results. First, the reflection responses were measured for the stackups in Figure 4.1 (b) and Figure 4.5 (a), representing the "Near" delamination case of the cross FSS. In this measurement, two X-band (8.2-12.4 GHz) horn antennas were place collinearly on one side of the FSS, with both horns emitting radiation in the direction of the FSS, with each receiving the reflected signal of the other. With this setup, four sets of measurements were collected for each delamination distance. The mean of the measured resonant frequency and depth are shown in Figure 4.12 (a) and (b), with error bars indicating the standard deviation. The corresponding results from the simulations given in Figure 4.3 and Figure 4.6 are also included for comparison. Meanwhile, the transmission responses were measured for the dielectric structures in Figure 4.8 (a-e), representing the "multi-layer" FSS delamination cases. Since the multi-layer FSS featured resonances spread over a large frequency range (from 3-9 GHz), a pair of wideband (0.75-20 GHz) ridged horn antennas were used for this measurement. To measure transmission through the FSS, these horn antennas were located on opposite sides of the FSS. For these delamination cases, three measured data sets were collected. The resulting mean and standard deviation are provided as a function of delamination distance and compared to simulation for each delamination case (Delam 1-5) in Figure 4.13-Figure 4.17, respectively. In these figures, Res. 1 and Res. 3 refer to the lower frequency and upper frequency resonances of the cross-loop FSS (respectively), and Res. 2 refers to the crossed-dipole FSS resonance. Figure 4.13-Figure 4.17 (a) shows the results of resonant frequency for Res. 1-3 as a function of delamination distance, while Figure 4.13-Figure 4.17 (b)-(d) gives the resonant depths of Res. 1-3, respectively. Simulation results are also included in these figures for comparison.
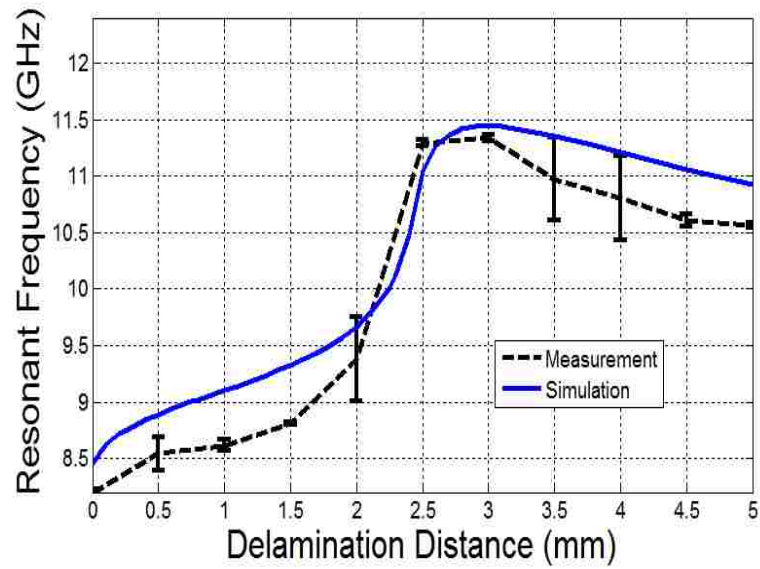
(a)
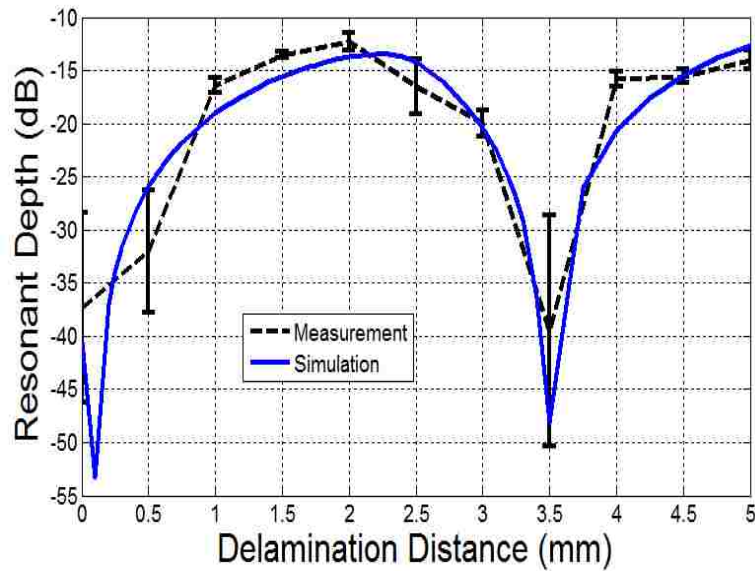
(b)

Figure 4.12. Comparison of measurement and simulation of resonant frequency (a) and resonant depth (b) of the crossed-dipole FSS as a function of delamination distance for "Near" delamination shown in Figure 4.1.
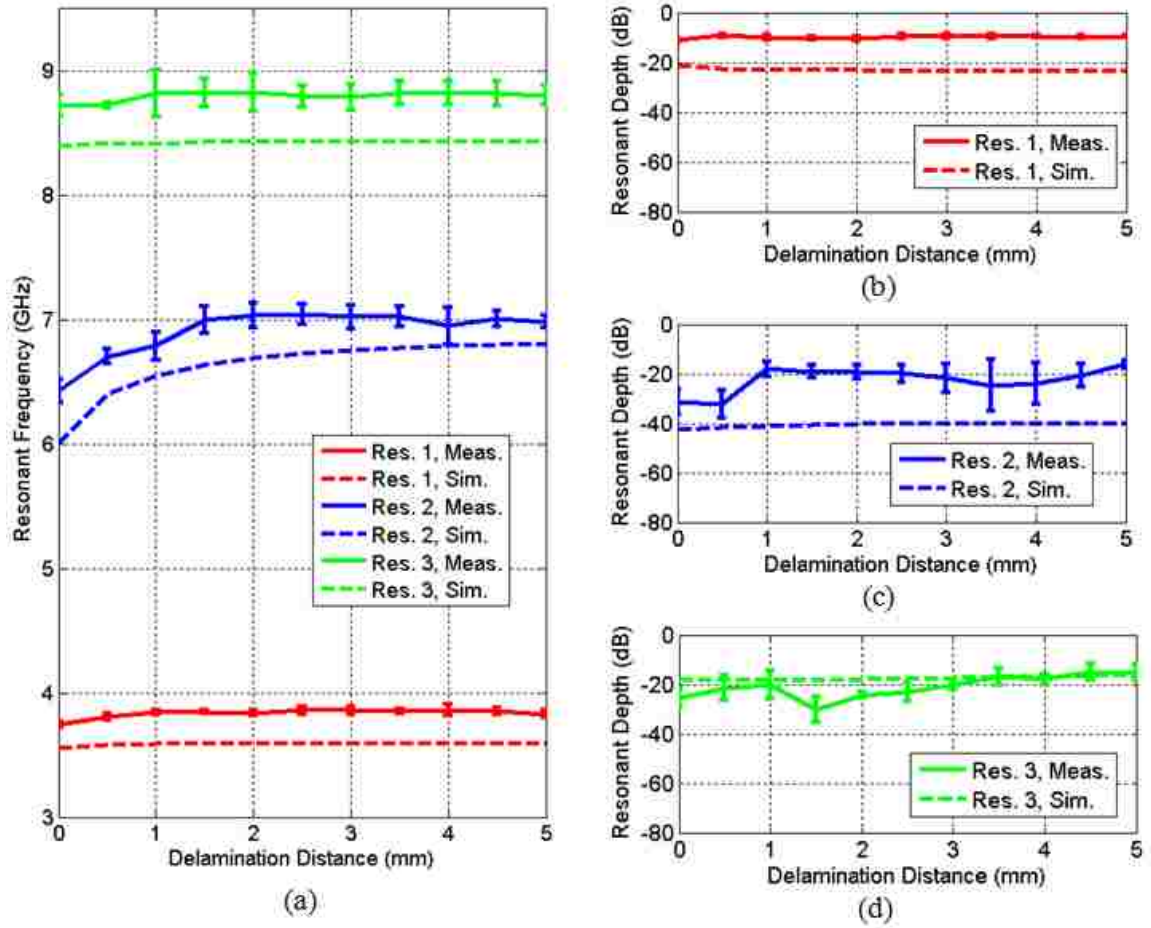
Figure 4.13. Measurement of resonant frequency (a) and resonant depth (b-d) of a multi-layer FSS-integrated stackup as a function of delamination distance for Delam 1 (Figure. 4.7 (a)).
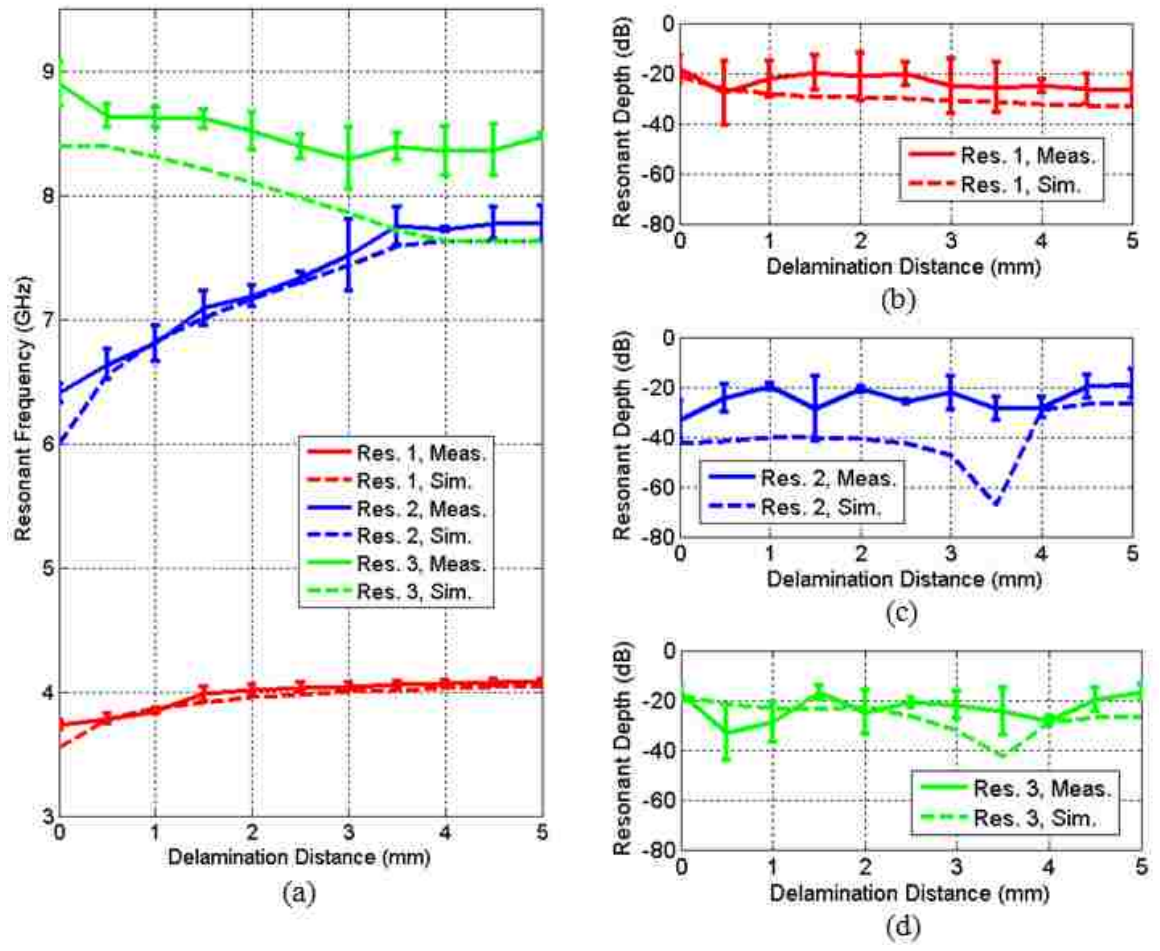
Figure 4.14. Measurement of resonant frequency (a) and resonant depth (b-d) of a multi-layer FSS-integrated stackup as a function of delamination distance for Delam 2 (Figure. 4.7 (b)).
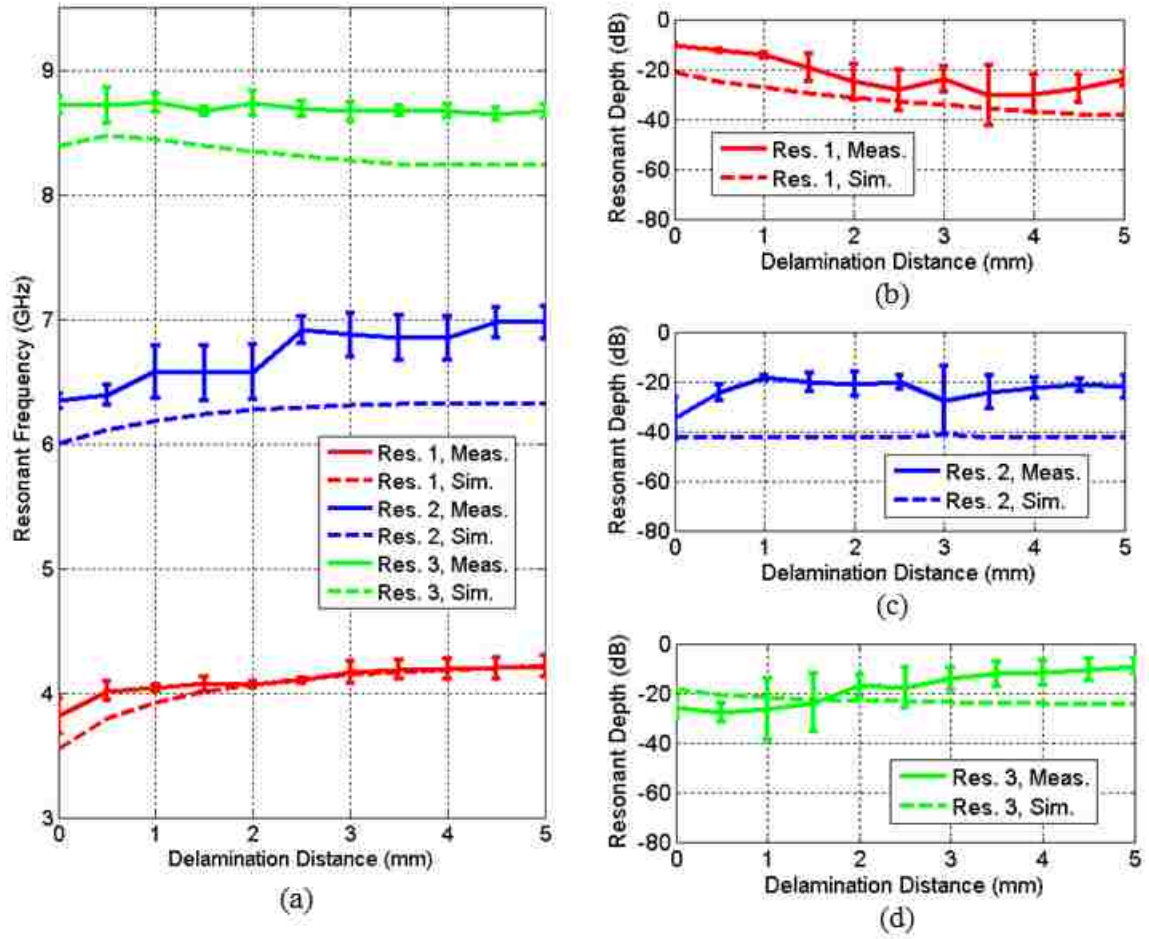
Figure 4.15. Measurement of resonant frequency (a) and resonant depth (b-d) of a multi-layer FSS-integrated stackup as a function of delamination distance for Delam 3 (Figure. 4.7 (c)).
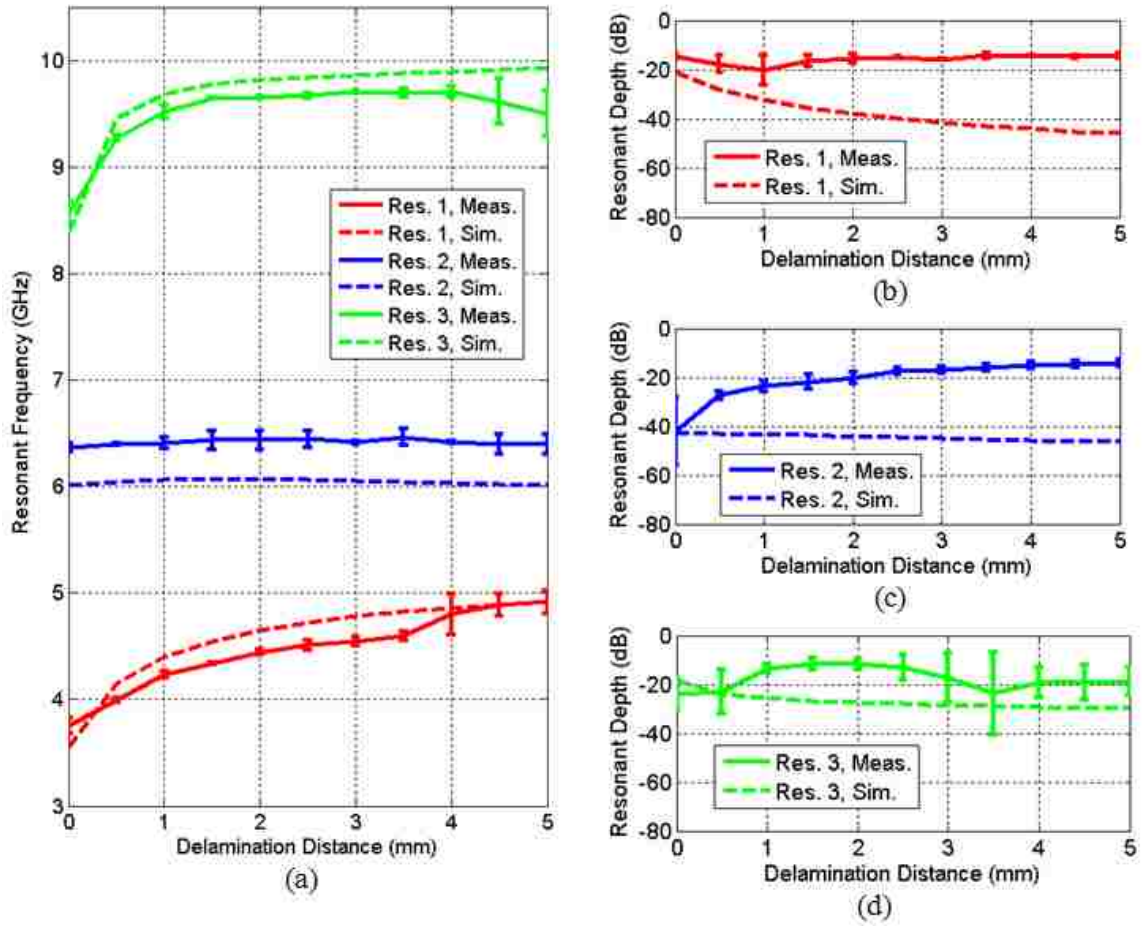
Figure 4.16. Measurement of resonant frequency (a) and resonant depth (b-d) of a multi-layer FSS-integrated stackup as a function of delamination distance for Delam 4 (Figure. 4.7 (d)).
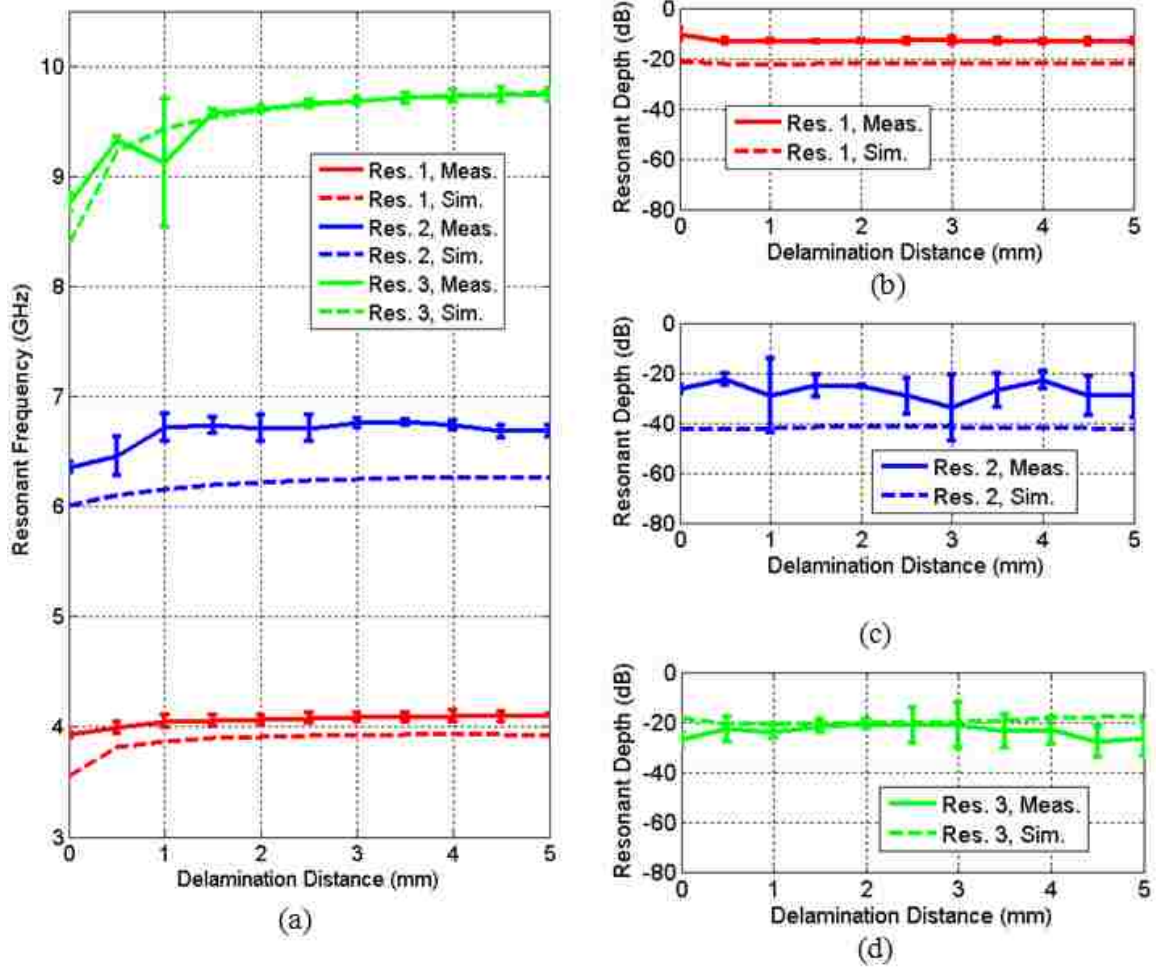
Figure 4.17. Measurement of resonant frequency (a) and resonant depth (b-d) of a multi-layer FSS-integrated stackup as a function of delamination distance for Delam 5 (Figure. 4.7 (e)).

Overall, the trends in measured resonant frequencies for all delamination cases match quite well with simulation. However, the measured resonant frequencies differ from the simulated resonant frequencies, with a difference of up to 0.5 GHz for the crossed-dipole FSS. This may be due to the FSS's physical dimensions not matching those used in simulation as a result of minor errors in individual elements introduced during the production process (such as conductor width and length being smaller than intended due to over-etching). Additionally, variations in delamination distance due to

sagging of the dielectric sheets and irregular sizing in the applied spacers (observed to have 0.2 mm of deviation or more) may have contributed to this difference. Furthermore, minor errors in measurement (such as unintended variation in incident angle) may also have contributed. Additionally, there was minimal deviation in resonant frequency (<0.3 GHz for most datasets) between measurement sets (for a given Delam.), with the crossed-dipole FSS resonance exhibiting the most variation (0.8 GHz for 3.5 mm of delamination in Figure 4.12), potentially due to this FSS having a higher sensitivity to incident angle [3]. For resonant depth, however, significant deviations from the simulation results occurred (~20 dB of difference for the worst cases). This deviation was especially noticeable for the crossed-dipole resonance, again potentially due to higher incident angle sensitivity. Furthermore, the measured resonant depths tended to be inconsistent between datasets, with the individual data points varying significantly (up to 30 dB) for each delamination distance. This variability may be due to minor alignment errors between the horn antennas leading to radiation losses between antennas. In addition, the VNA's limited number of frequency acquisition points may have affected measured resonant depth for the deeper resonances. That is, a given resonance may not have been measured at its deepest point if it occurred in between the frequency points measured by the VNA. Ultimately, however, this result indicates that measurement of transmission resonant depth may be an unreliable indicator of delamination distance for practical delamination detection, leaving resonant frequency as a better choice for quantifying delaminations.

4.2. DETERMINATION OF EFFECTIVE PERMITTIVITY THROUGH CONFORMAL MAPPING

Thus far, full-wave simulation-based investigations of an FSS's sensitivity to the presence of one or more delaminations have been limited to specific cases. However, if this method is to be generalized for an arbitrary FSS integrated within an arbitrary dielectric structure, the use of full-wave simulation to design the FSS and study its subsequent response may become computationally intensive due to the wide variety of possible delamination scenarios and FSS elements. As such, analytical methods may be needed to determine an FSS's response to delamination. Additionally, analytical calculations of an FSS's response in the presence of dielectrics can facilitate initial FSS design and analysis prior to utilizing full-wave simulation for more detailed studies. This

design approach reduces the need for computationally intensive full-wave simulation-based FSS design optimization, and instead only uses full-wave simulation for more robust and detailed verification and/or study of the final FSS design. In general, to design an FSS for delamination sensing in an arbitrary layered dielectric structure, three main steps are necessary. First, the FSS's inductance and capacitance must be calculated in the absence of dielectrics (i.e., freestanding) to determine the freestanding impedance of the FSS. This can be accomplished by using the modified Marcuvitz strip grating equations given in Section 2.2 [16]. Next, the effective permittivity ($\varepsilon_{\mathrm{r},\mathit{eff}}$) relevant to the FSS must be calculated. $\varepsilon_{\mathrm{r},\mathit{eff}}$ is related to how multiple surrounding dielectrics alter the impedance of an FSS, and is determined based on electric field coupling between FSS elements within the dielectrics. By modifying the wavelength of Marcuvitz's equations by $\varepsilon_{\mathrm{r},\mathit{eff}}$, the resulting dielectrically-loaded impedance of the FSS can be found. Lastly, the frequency response of the entire FSS-integrated dielectric structure must be determined. This can be obtained by using a transmission line model in which the FSS impedance acts as a load (in shunt) between a series of transmission lines that represent each surrounding dielectric layer. This model can determine not only the response of the FSS, but also any reflections inherent to the dielectric structure. To date, analytical approximation equations are available for finding the freestanding impedance of a variety of different FSS elements [13], [16], as well as for calculating the response of a transmission line model [44], meaning that these calculations can be easily implemented into an efficient computation engine, such as Matlab [45]. However, existing equations to approximate $\varepsilon_{\mathrm{r},\mathit{eff}}$ for an FSS are based on curve-fitting of known FSS examples, with poor consideration for varying dimensions of an FSS [46]. Additionally, these models are limited to FSSs with a single dielectric layer. As such, a new form of analytical approximation based on conformal mapping was developed to extend the above model for layered dielectric structures [53].

Conformal mapping is the process of transforming a given coordinate system into a different coordinate system that preserves the angles between the vertices of the two coordinate systems [49]. In the field of high-speed electronics, the capacitance of transmission line structures on printed circuit boards (PCBs) is often approximated using conformal mapping techniques. The main advantage of using a conformal map approach

for a given problem is that it can simplify the problem's geometry into a more easily solvable form. This transformation is accomplished through a series of weighting functions on the geometry's coordinate system. As an example, to determine the capacitance in a PCB transmission line system, a conformal map may be used that transforms a cross-section of the strip-line geometry into the form of two infinite parallel plates [47]. This greatly simplifies the problem, as this geometry lends itself better to an analytical solution, and the equation for the capacitance between two parallel plates is well known. While this method was originally developed for finding $\varepsilon_{r,eff}$ in PCB structures, it may also be applied for finding $\varepsilon_{r,eff}$ that corresponds to the coupling of a given FSS [53] (including one embedded in a layered dielectric). That is, since the majority of capacitive coupling between FSS elements is often between individual conducting segments of the elements, this coupling behavior can be modeled as two mutually coupled transmission lines. For this purpose, conformal maps of two common transmission line configurations are available in [47] that may be useful for finding $\varepsilon_{r,eff}$ for different FSS elements that share similar geometrical features with these transmission lines. These conformal maps are for a coplanar waveguide and coplanar line, and are illustrated in Figure 4.18 (a) and (b), respectively.
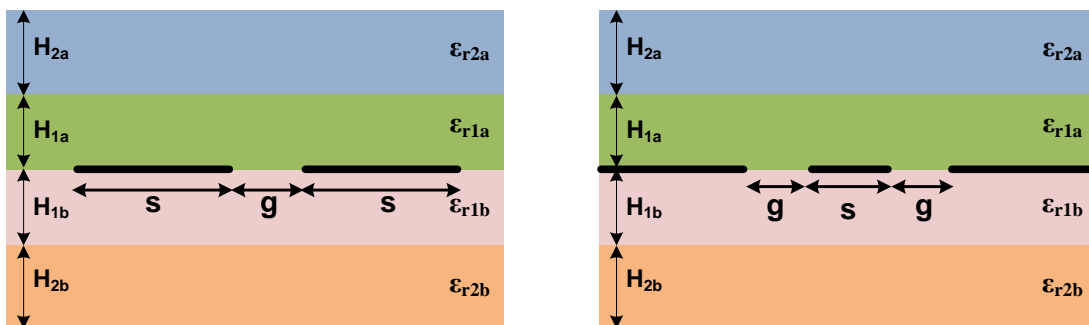
Figure 4.18. Coplanar line (a) and coplanar waveguide (b) configurations in a layered dielectric structure.

In both configurations shown in Figure. 4.17, s is the conductor segment width and g is the gap width between conductors. By applying these geometries to regions of coupling in FSS elements, the value of $\varepsilon_{r,eff}$ that corresponds to that coupling can be found. In order to do this, the capacitance of the freestanding geometry (denoted by C_0) is first determined, with additional capacitances added to account for each dielectric layer (where each capacitance is denoted as Ci, where i designates the specific layer). For the co-planar waveguide arrangement, the value of C_0 is found as [47]

$$C_0 = 4\varepsilon_0 K(k_0')/K(k_0) \tag{4.2}$$

where ε_0 is the permittivity of free space Here, K describes an elliptic integral of the first kind, and has inputs of k_0 and k_0', where $k_0 = \frac{s}{s+g}$ and $k_0' = \sqrt{1 - k_0^2}$. Next, the capacitance provided by each surrounding dielectric layer is determined as [47]

$$C_i = 2\varepsilon_0(\varepsilon_{ri} - \varepsilon_{r(i+1)})K(k_i')/K(k_i) \tag{4.3}$$

Here, ε_{ri} is the relative permittivity of dielectric layer i for which this capacitance is determined, while $\varepsilon_{r(i+1)}$ is the relative permittivity of the next farthest dielectric layer from the FSS. Meanwhile, k_i is given as [47]

$$k_i = \frac{\sinh(\pi s/2H_i)}{\sinh(\pi(s+g)/2H_i)} \tag{4.4}$$

where H_i is the combined thicknesses of all layers between the FSS and layer i. Lastly, k_i' is found as $k_i' = \sqrt{1 - k_i^2}$. Once the capacitance is found for each dielectric layer, the value of $\varepsilon_{r,eff}$ is determined by dividing the sum of all capacitance values by the freestanding capacitance C_0. A similar process can be used for the coplanar transmission line arrangement [47].

To illustrate the application of conformal mapping for approximating $\varepsilon_{r,eff}$ of an FSS, the square loop FSS element is considered. When a square loop FSS is excited by

incident radiation, surface currents are excited in the direction of polarization of the incident wave, creating electric fields (denoted as E) between the conductor segments of adjacent elements, the magnitude of which is shown in Figure 4.19. In this figure, the electric field coupling between the visible element and those adjacent (not shown) is illustrated. Additionally, fringe coupling (oriented perpendicularly to the incident wave polarization) is also evident at the element corners.
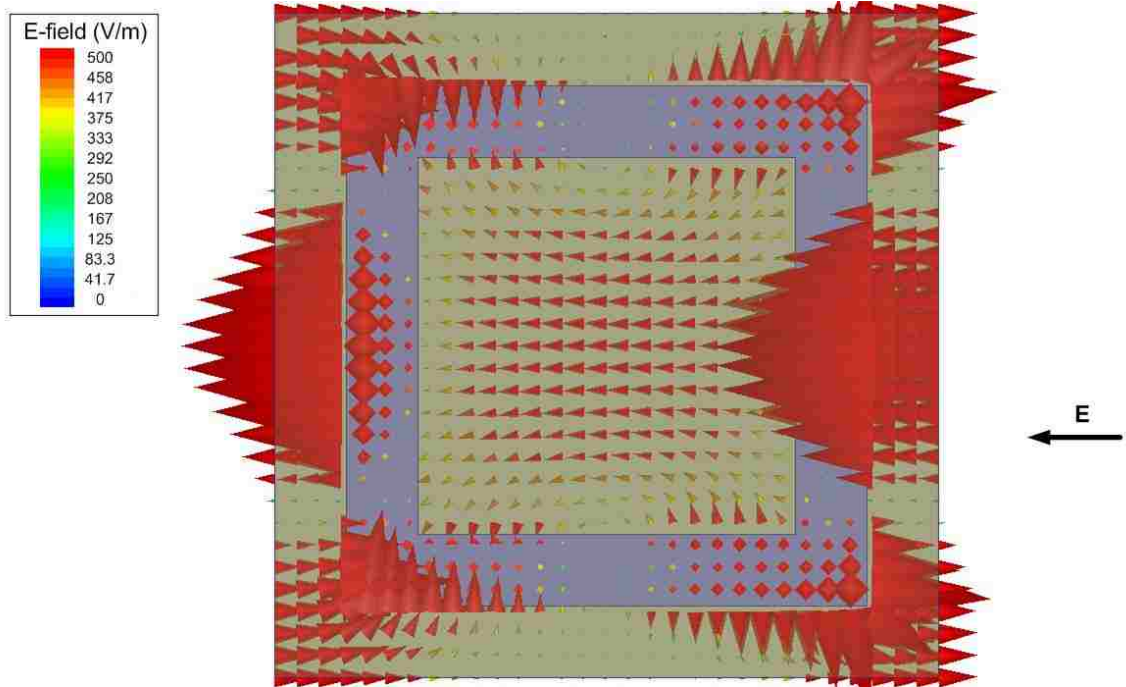
Figure 4.19. Illustration of electric field distribution between adjacent elements for a Square Loop FSS.

Since the majority of coupling occurs between parallel conductor segments (of adjacent elements), the capacitance of this structure is assumed to be equivalent to the

capacitance of the coplanar transmission line geometry previously described. While this assumption ignores minor differences in the electric field distribution including fringe coupling that occurs at the ends of these segments, this method still serves as a valid first-order approximation since fringe coupling is not the dominant contributor to the FSS's impedance. As such, $\varepsilon_{r,eff}$ is calculated for the FSS embedded in the dielectric structure of Figure 4.20 (a) and (b). Here, 'w' and 'g' define the FSS conductor and gap widths, and 'h' and 'er' define the height of (two) dielectric layers and permittivity. The value of $\varepsilon_{r,eff}$ determined from the conformal mapping approach is compared to that obtained via full-wave simulation and presented in Table 4.1 for a variety of different test cases (labeled as Cases 1 - 13) for the dimensional parameters shown in Figure 4.20. For simulation, $\varepsilon_{r,eff}$ is determined based on the difference in resonant frequency between the freestanding FSS (f_0) and embedded FSS (f), calculated as

$$\varepsilon_{r,eff} = \sqrt{f_0/f} \tag{4.5}$$

FSS dimensions were chosen for Case 1 to produce a resonance in the desired frequency region (1-10 GHz). From this, dimensions for the other cases were chosen in order to investigate the effect of the dimensional parameters shown in Figure 4.20 on $\varepsilon_{r,eff}$ by varying them above and below the individual parameters of Case 1.

Overall, the differences in $\varepsilon_{r,eff}$ calculated using the conformal mapping approach and full-wave simulation are within approximately 0.2 (a maximum error of 8%). The worst cases occur for larger gap widths and for lower permittivity dielectrics. This deviation is likely due to the conformal mapping method not accounting for the fringe coupling at the conductor ends (as mentioned above). This may be due to a reduction in the ordinary coupling between elements when the gap widths are larger or when the dielectrics have a lower permittivity, meaning that fringe coupling would have a more dominant effect for these cases. However, it is important to remember that the conformal mapping approach provides a first order approximation and as such, this error is considered acceptable for initial design work and analysis. More accurate results can be determined via subsequent full-wave simulation after the initial design is determined (if needed).

(a)   (b)
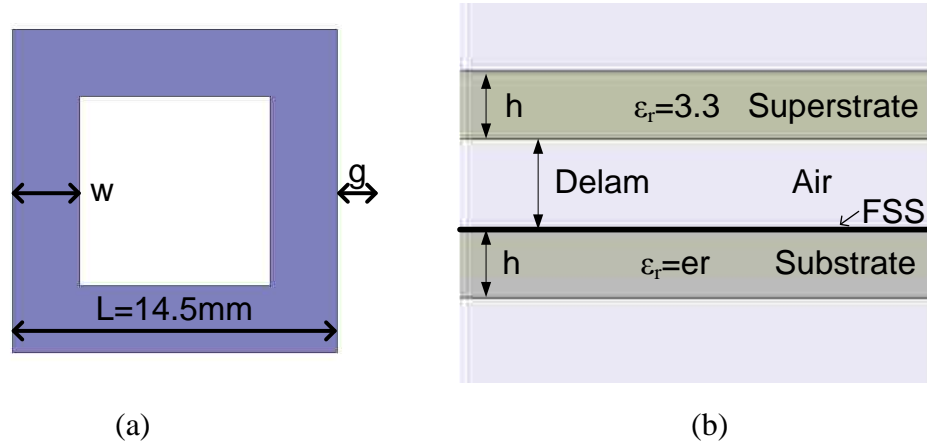
Figure 4.20. Square Loop FSS (a) and dielectric structure (b) used to demonstrate approximation of $\varepsilon_{r,eff}$.

Table 4.1. Comparison of $\varepsilon_{r,eff}$ calculated using the conformal mapping approach and full-wave simulation.

	Parameters					$\varepsilon_{r,eff}$		
	w	g	h	er	delam	Sim	Conf. Map	% Error
Case 1	3 mm	4 mm	2.54 mm	4	0 mm	2.97	2.76	6.97
Case 2	1 mm	4 mm	2.54 mm	4	0 mm	3.21	3.15	1.93
Case 3	2 mm	4 mm	2.54 mm	4	0 mm	3.09	2.93	4.99
Case 4	3 mm	5 mm	2.54 mm	4	0 mm	2.89	2.66	8.02
Case 5	3 mm	6 mm	2.54 mm	4	0 mm	2.80	2.58	7.86
Case 6	3 mm	4 mm	5.08 mm	4	0 mm	3.48	3.29	5.49
Case 7	3 mm	4 mm	7.62 mm	4	0 mm	3.61	3.47	3.96
Case 8	3 mm	4 mm	2.54 mm	1	0 mm	1.90	1.77	7.06
Case 9	3 mm	4 mm	2.54 mm	2	0 mm	2.25	2.10	6.88
Case 10	3 mm	4 mm	2.54 mm	3	0 mm	2.61	2.43	6.90
Case 11	3 mm	4 mm	2.54 mm	4	1 mm	2.41	2.46	2.41
Case 12	3 mm	4 mm	2.54 mm	4	2 mm	2.27	2.29	0.84
Case 13	3 mm	4 mm	2.54 mm	4	3 mm	2.22	2.18	1.62

Using this conformal mapping approach, the response of the square loop FSS to layered dielectrics (including delaminations) can be determined. As such, a Matlab[©] model was created that calculates the input impedance of a layered dielectric structure with one or more embedded FSSs. First, the model calculates the impedance of each dielectric and FSS layer. For the dielectric layers, the impedance is calculated as $Z_d = 377 * \sqrt{\mu_r/\varepsilon_r}$, where μ_r and ε_r are the relative permeability and dielectric constant (including both permittivity and loss factor) of the dielectric. For the FSS layers, the impedance is calculated using the inductance and capacitance of the FSS, as determined by the modified Marcuvitz equations given in Section 2.2 [16]. Next, $\varepsilon_{r,eff}$ is calculated for each FSS using the conformal mapping approach, which is subsequently used to scale the wavelength in the FSS's inductance/capacitance approximation equations. Once the impedance of each FSS or dielectric layer is determined, the ABCD transmission matrix of each layer is determined [44]. For each of the dielectric layers, the ABCD matrix is

$$\begin{bmatrix} A & B \\ C & D \end{bmatrix} = \begin{bmatrix} \cos\beta h & jZ_d\sin\beta h \\ j/Z_d \sin\beta h & \cos\beta h \end{bmatrix} \qquad (4.6)$$

where Z_d is the dielectric's impedance, h is the dielectric's thickness, and $\beta=2\pi/\lambda$, where λ is the wavelength of the incident wave. Meanwhile, the ABCD matrix of the FSS is given as

$$\begin{bmatrix} A & B \\ C & D \end{bmatrix} = \begin{bmatrix} 1 & 0 \\ 1/jZ_{fss} & 1 \end{bmatrix} \qquad (4.7)$$

where Z_{fss} is the FSS impedance, calculated from the values of inductance and capacitance found above. Once the ABCD matrix has been calculated for each layer, they are multiplied together to give the ABCD matrix of the entire structure. This matrix can be used to find the reflection and transmission response (S_{11} and S_{21}) of the structure through

$$S_{11} = \frac{A*Z_0 + B - C*Z_0^2 - D*Z_0}{A*Z_0 + B + C*Z_0^2 + D*Z_0} \tag{4.8}$$

$$S_{21} = \frac{2*Z_0}{A*Z_0 + B + C*Z_0^2 + D*Z_0} \tag{4.9}$$

where Z_0 is the background impedance surrounding the structure, generally assumed to be the free-space impedance, and A-D are the individual elements of the overall ABCD matrix [48]. One limitation of this algorithm is that since the surface resistance of the FSS cannot be determined, the FSS's resonant depth cannot be accurately modeled. This occurs because surface resistance creates losses that reduce a resonance's depth (and this reduction not included in this model). Additionally, this algorithm is inaccurate when an FSS layer is located close enough to another FSS layer such that electric field coupling occurs between the two layers, since the effects of this coupling on the FSS's inductance and capacitance are not considered in the model. In these cases, full-wave simulation will still be required to provide an accurate estimate of the structure's frequency response.

To test the accuracy of this algorithm, the Matlab model was used to calculate the resonant frequencies of the test cases provided in Table 4.1, with the results shown in Table 4.2. Additionally, the frequency response of Case 13 (see Table 4.2) calculated using the Matlab model and an HFSS full-wave simulation is shown in Figure 4.21.

Overall, the results from the Matlab model and HFSS match well, with a worst-case error (from the simulated value) of 8.5% (for Case 2). Since $\varepsilon_{r,eff}$ for Case 2 had matched well with simulation, this error is likely due to inaccuracies in the impedance calculation from Marcuvitz's equations. As noted, the resonant depth generated by the Matlab program is much deeper than that of HFSS, largely due to the lack of surface resistance in the Matlab model (since resistance reduces the resonant depth of a filter). However, despite this limitation, the quick computational speed (a few seconds, compared to full-wave simulation often taking hours) of this model renders it a powerful analysis tool. In the future, this tool can be expanded for other FSS elements by developing appropriate conformal maps for calculating $\varepsilon_{r,eff}$, as well as equations for calculating FSS inductance and capacitance.

Table 4.2. Resonant frequency for the geometry shown in Figure 4.20 as calculated from the Matlab model and HFSS.

	Parameters					Resonant Frequency (GHz)		
	w	g	h	er	delam	Sim	Conf. Map	% Error
Case 1	3 mm	4 mm	2.54 mm	4	0 mm	5.61	5.86	4.49
Case 2	1 mm	4 mm	2.54 mm	4	0 mm	3.67	3.91	6.40
Case 3	2 mm	4 mm	2.54 mm	4	0 mm	4.51	4.89	8.49
Case 4	3 mm	5 mm	2.54 mm	4	0 mm	5.70	6.03	5.88
Case 5	3 mm	6 mm	2.54 mm	4	0 mm	5.75	6.16	7.10
Case 6	3 mm	4 mm	5.08 mm	4	0 mm	5.18	5.37	3.61
Case 7	3 mm	4 mm	7.62 mm	4	0 mm	5.09	5.23	2.69
Case 8	3 mm	4 mm	2.54 mm	1	0 mm	7.01	7.33	4.56
Case 9	3 mm	4 mm	2.54 mm	2	0 mm	6.44	6.73	4.41
Case 10	3 mm	4 mm	2.54 mm	3	0 mm	5.98	6.25	4.46
Case 11	3 mm	4 mm	2.54 mm	4	1 mm	6.23	6.20	0.47
Case 12	3 mm	4 mm	2.54 mm	4	2 mm	6.41	6.43	0.28
Case 13	3 mm	4 mm	2.54 mm	4	3 mm	6.49	6.59	1.59
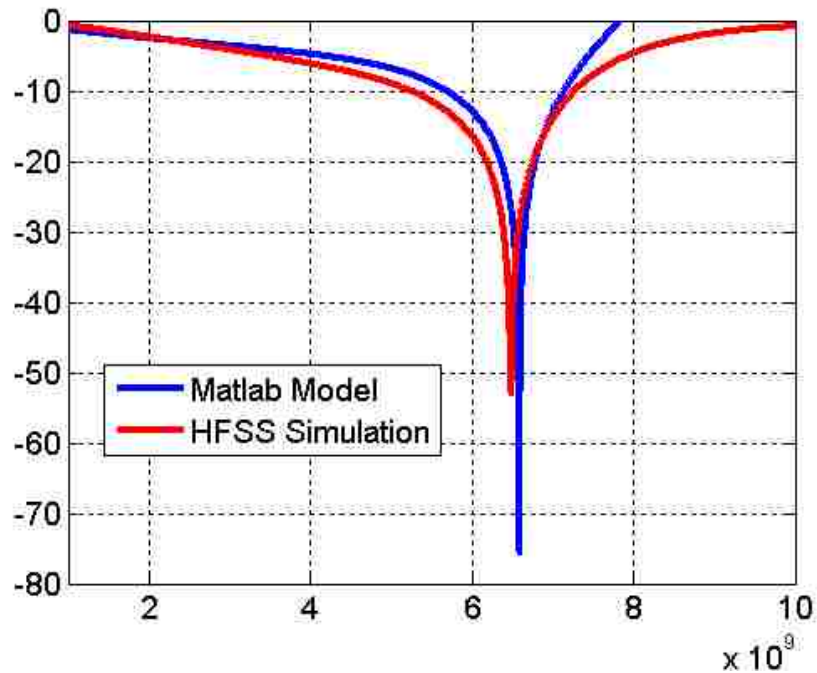
Figure 4.21. Comparison of transmission response calculated from the Matlab model and HFSS for Case 13 in Table 4.2.

To decide how to apply existing conformal maps (or when developing new maps), regions of electric field coupling within the FSS must be determined. Conformal maps can then be applied that match these coupling geometries. For instance, a crossed-dipole FSS could potentially be modeled using the coplanar waveguide conformal map. Meanwhile, inductance and capacitance approximations can be added from existing sources (such as [13] and [17]), if available, or developed. Alternatively, the capacitance and inductance of a freestanding FSS can be found using full-wave simulation, with the conformal mapping method being applied to find $\varepsilon_{r,eff}$ for the FSS when embedded within various dielectric structures.

4.3. CONCLUSION

In this section, the response of an FSS to changes in adjacent dielectric layers was analyzed for sensing structural defects, such as delaminations/disbonds. The results show that the frequency response of an FSS is sensitive to changes in surrounding dielectrics. This occurs due to the change in the FSS's capacitance as a result of the change in dielectric, thus altering its resonant frequency. Consequently, for an FSS embedded within a dielectric structure, delamination within that structure decreases the FSS's capacitance due to the air gap's lower permittivity. Additionally, when interrogating an FSS that is integrated into a dielectric structure, the depth of the FSS's reflection resonance was found to be altered due to additional reflections from the dielectric interfaces. Observation of resonant depth may provide another parameter to analyze for sensing changes in a surrounding dielectric structure, and may also be useful for distinguishing the effects of dielectrics on an FSS from other sensing concerns, such as normal strain. However, resonant depth measurements may be unreliable due to sensitivity to incident angle, which may be difficult to control for in practical measurements.

To investigate these phenomena, a series of simulations and measurements were conducted on a set of FSS samples integrated into different dielectric structures. The frequency responses of these elements were simulated when integrated into a series of dielectric layer configurations, some of which included delaminations. These FSSs and dielectric layers were subsequently constructed and measured to provide verification of

simulated results. Overall, measurements of these individual FSS samples matched well with simulation, indicating that FSSs have potential as delamination sensors. Furthermore, the results indicate that FSS's are sensitive to delaminations occurring in close proximity to the FSS. As such, additional simulations and measurements were conducted showing that multiple FSS layers (that resonant at different frequencies) could be integrated into a given dielectric structure to better determine the location of a delamination. For this study, simulation was found to match well with measurement when monitoring the effect of delaminations on each FSS's resonant frequency. However, the resonant depth of each FSS was found to be less consistent between measurement and simulation. As such, the use of resonant depth for delamination monitoring may not be reliable, while monitoring of resonant frequency remains promising.

Lastly, to better predict how delamination can affect an FSS, an algorithm was developed for approximating $\varepsilon_{\mathrm{r},eff}$ for an FSS when integrated into an arbitrary dielectric structure. To find $\varepsilon_{\mathrm{r},eff}$, a conformal mapping technique was used to model how electric fields couple between conductors within surrounding dielectric layers. Overall, $\varepsilon_{\mathrm{r},eff}$ calculated with this method for a square loop FSS were found to match well with simulation for a variety of FSS parameters and surrounding dielectric layer configurations. This analytical approximation was subsequently applied to an algorithm for solving transmission lines that found the frequency response of an FSS when integrated into a dielectric structure. Ultimately, this algorithm was also found to produce frequency responses that matched well with simulation. As such, the resonant frequency and overall trends in frequency response could be modeled quickly and reliably, making this method useful for simple analysis and design.

5. CONCLUSION/FUTURE WORK

5.1. SUMMARY/CONCLUSION

In this thesis, Frequency Selective Surfaces (FSSs) have been investigated as potential embedded Structural Health Monitoring (SHM) sensors. In Section 2, an overview of FSS theory and design principles was provided. Section 2.1 presented a brief history of FSS development. Meanwhile, Section 2.2 discussed the basic physics behind FSS operation, and provided examples of some common FSS elements, as well as methods for determining their frequency response. Finally, in Section 2.3, more advanced FSS design considerations were presented, such as the effects of incident angle, curvature, and local dielectric and conductors.

In Section 3.1, the use of FSSs for normal strain detection and characterization was studied. Normal strain is defined as a stretching or compressing deformation of a structure [39]. Since the resonant frequency of an FSS is a function of the FSS geometry (conductor length, width, etc.), this resonant frequency is shifted when the FSS's geometry undergoes some deformation, such as normal strain. The response of common FSS elements to normal strain was initially determined through full-wave electromagnetic simulation [23], where the change in resonant frequency due to normal strain were characterized for each element by a gauge factor value. Representative measurements were also conducted to verify the simulation results. In Section 3.2, a similar investigation was conducted to determine the response of FSSs to shear strain (defined as a twisting deformation of a structure [36]). Previously, it has been found that shear strain causes FSSs to cross-polarize (changing the electric field direction of the incident wave to be rotated by 90° from its original orientation) reflected radiation at the FSS's resonant frequency [35]. Conversely, shear strain is known to have a minimal effect on the co-polarized frequency response (used for normal strain detection). As such, the response of an FSS to shear strain may be easily distinguished from the FSS's response to normal strain, allowing a single FSS to sense both forms of strain simultaneously. In this work, these shear strain-sensing capabilities were verified through full-wave simulation for a variety of FSS elements. Additionally, it was found that grounded FSS elements provided the strongest cross-polarization response to shear

strain, making them more advantageous for shear strain sensing purposes. Unfortunately, however, these simulations could not be verified through measurement due to sample preparation limitations at the time of this investigation. Finally, in Section 3.3, FSS samples were applied as normal and shear strain sensors in a practical system. More specifically, two FSS samples were adhered to the hollow steel tube of a new concrete column design. These FSS samples were interrogated as the concrete columns underwent linear displacement (i.e., normal strain) and torsional (i.e., shear strain) load testing. The results showed that the normally strained FSS sample's response was found to compare well with traditional strain gauge sensors while also showing an improved sensing range. Additionally, the wireless nature of FSS sensors offers an additional advantage over traditional wired strain gauges. For the torsional load test, however, cross-polarized radiation wasn't measured from the shear-strained FSS. This implies that cross-polarization may not have occurred due to the FSS sample not being deformed as expected. Alternatively, signal losses due to the concrete column may have masked any returned cross-polarized signal.

In Section 4, the use of FSS for delamination and disbond detection was investigated. Delaminations are separations that occur in a laminate structure, creating air gaps and weakening structural integrity [43]. Meanwhile, disbonds are a form of delamination in which two bonded materials become separated. When an FSS is embedded in a dielectric, capacitive coupling between FSS elements is increased due to the presence of the dielectric. This decreases the resonant frequency of the FSS. The effectiveness of the dielectric at altering this capacitance is a function of its permittivity and its proximity to the FSS. As such, in the event of delamination, the subsequent air gap (with relative permittivity equal to 1) causes the FSS's capacitance to reduce, thus increasing the resonant frequency. Furthermore, the depth of the FSS's resonant null is altered because the delamination creates additional dielectric interfaces that cause subsequent additional reflections. This change in resonant null depth allows the effects of delamination to be differentiated from the effects of normal strain on the FSS's frequency response, as normal strain generally has a minimal effect on resonant null depth. Additionally, it was found that a delamination has a greater effect on the FSS's resonance when it occurred in close proximity to the FSS. This means that an FSS is able

to sense delaminations in the region local to the FSS. As such, in larger or more complex dielectric structures, additional FSS layers may need to be embedded throughout the structure to achieve full sensing coverage. To verify these results, a series of measurements were conducted. FSS samples were created from etched PCBs that were placed between dielectric sheets. Delaminations were created in these structures by separating the sheets using small spacers. Overall, measurement results agreed well with simulation. A second set of measurements was then carried out to test the use of multiple FSSs in a single structure. These multi-layer FSS structures were constructed in a similar manor as for the first set of measurements, with the FSS layers being spaced far enough apart to avoid mutual coupling between them. Next, delaminations were introduced in several locations throughout this structure. Ultimately, it was found that the FSS closest to a delamination is most sensitive to it (as expected). This confirmed that multiple FSSs can be used to provide distributed sensing coverage for different regions of a more complex structure. Additionally, while measurement results of resonant frequency shift for each FSS matched well with simulation, resonant null depth for this application was found to be less comparable. This is attributed to potential measurement errors such as misalignment of the interrogating antennas, or may indicate that resonant null depth may be difficult to predict through simulation. As such, resonant null depth is not suggested to be used as a primary indicator of delamination in practical measurements.

Lastly, in Section 4.2, a method was developed for estimating the effective permittivity ($\varepsilon_{r,eff}$) of an FSS when embedded into a dielectric structure using a conformal mapping approximation. $\varepsilon_{r,eff}$ is a composite value of the relative permittivities of surrounding dielectrics based on how the FSS capacitively couples within those dielectrics, and is instrumental to quantifying the response of an FSS to delamination. Previous algorithms for approximating $\varepsilon_{r,eff}$ used curve fitting methods, but were ultimately limited to specific FSS elements and could only be used when the FSS was in the presence of a single dielectric layer on either side of the FSS surface [46]. Since this method proved ineffective for analysis of FSS-integrated delaminated structures, a new method for approximating $\varepsilon_{r,eff}$ was developed using conformal mapping. This method has previously been used for calculating $\varepsilon_{r,eff}$ in PCB structures. By applying a transform to transmission line cross-sections in the PCB, these transmission lines could be modeled

as parallel plates, for which $\varepsilon_{r,eff}$ can be easily calculated. This method could be applied to FSS by modeling relevant sections of the FSS as coplanar strip or coplanar waveguide transmission lines. To test this method, a conformal mapping approximation was developed for the square loop FSS. This method was tested for a variety of FSS parameters and dielectric structures. The results were compared with simulation, and were found to match well. Using this conformal mapping model to approximate $\varepsilon_{r,eff}$ in, a Matlab [45] model was developed to calculate the frequency response of an FSS embedded within a dielectric structure. This model represented the FSS as an LC filter circuit shunted into a transmission line network that modeled the different dielectric layers, with the frequency response of this structure being calculated using ABCD parameters. The inductance and capacitance of the FSS was calculated using previously developed strip-grating equations [16] which were then modified by the approximated $\varepsilon_{r,eff}$. Resonant frequency responses generated by this model were found to also match well with simulation. As such, this model can be used to rapidly calculate the frequency response of an FSS in a dielectric structure, both with and without a delamination. Additionally, this model can be extended in the future to calculate the response of other FSS elements, once conformal maps and LC approximations for these elements are determined.

5.2. FUTURE WORK

As a result of this investigation, FSS-based sensors have been shown to have great potential for a variety of SHM applications. As such, in order to continue the development of this new sensing methodology for SHM, the following areas of future work are suggested.

5.2.1. Development of FSS-Based Sensing for Shear Strain. In this thesis, the use of FSSs for sensing normal strain, shear strain, and delamination was investigated, through both full-wave simulation and empirical representative measurements. While the measurement results of normal strain and delamination matched well with simulation, the effects of shear strain on the FSS response could not be experimentally verified. As such, further investigations of shear strain sensing, especially measurement-based, are needed.

5.2.2. Development of FSS Sensor Element Design Rules. Throughout this work, a variety of common FSS elements have been analyzed for different forms of SHM sensing. Each of these elements have been found to provide different advantages and disadvantages for different sensing applications. By extending this analysis, it may be possible to develop a set of FSS design rules for different sensing scenarios. By understanding what aspects of an FSS design provide desired sensing capabilities, FSS sensor design rules may be developed that can mitigate or enhance some of the sensing issues and traits explored throughout this work. Such characteristics of note include incident angle sensitivity, polarization sensitivity, gauge factor, shear strain response, and sensitivity to local dielectrics and closely spaced FSS and conductor layers. Additionally, FSS structures featuring multiple resonances can also be utilized for improved sensing accuracy by providing additional data or separate sensing capabilities within a single FSS layer.

5.2.3. Active FSS Element Sensing. All FSS elements discussed throughout this thesis have been entirely passive in nature. However, active electronic components, such as PIN diodes, are often integrated into FSS designs to provide electronic control of the FSS response [6]. These active FSSs provide a number of features, such as resonant frequency modulation. This allows an FSS layer to be effectively "turned off", meaning that its pass band resonance becomes a stop band, or vice versa. Alternatively, active components can be used to switch an FSS's resonance to a different frequency. Such functionality can be useful for FSS sensing applications, as it allows an FSS's response to be digitally controlled. For instance, in a multi-layer FSS structure, modulation of each FSS layer can allow the user to interrogate each layer individually. Alternatively, when the measured response is noisy or otherwise indiscernible, continuous modulation of the FSS's response can help a user to identify its resonance among the noise. Additionally, this technique may also allow a user to select only a single region of a large FSS surface, providing potential spot-checking functionality. Possible challenges that may pertain to the design and use of active elements in FSS sensing include fragility of the electronic components to strains or other stresses that might occur in an FSS-integrated structure. Furthermore, active FSS elements require external biasing, which may be difficult to integrate into structures as well as increasing the sensor cost. Despite these concerns,

however, active FSS elements may provide a host of enhanced SHM sensing capabilities that merit further investigation.

5.2.4. Optical Wavelength FSS. One of the long-term goals of FSS research is the development of optical wavelength FSSs. These are FSSs that operate in the visible light region of the electromagnetic spectrum, meaning that they can transmit, absorb, or reflect certain colors of visible light [50]. Such research has been challenging from a materials standpoint, however, due to the difficulty of producing FSS elements at the optical scale. Since the resonant frequency of an FSS is related to the size of the FSS element in relation to wavelength, an optical FSS element would be on the nanometer scale, for which advanced manufacturing techniques must be used. That being said, optical FSSs may still operate in a similar manor to the microwave scale FSSs discussed in this thesis, since the operation principles of FSS are scalable. As a result, an optical FSS may also behave similarly to a microwave FSS when deformed. This is significant, as it would imply that a normally strained optical FSS would change its color due to the shift in resonant frequency. Unlike the microwave FSSs used in this thesis, which had to be measured using specialized equipment, the response of an optical FSS can be seen purely with the human eye for a surface mounted sensor. As a result, a structure that has normal strain can be analyzed purely through human inspection by taking note of what color the optical FSS has changed to, as well as where on the FSS the color has been changed. This could make FSS sensing easily accessible to the end-user by removing the need for specialized measurement equipment. One drawback of optical FSS is that it would only be effective on the surface of a structure, or within transparent structures. Furthermore, this all assumes that optical FSSs are similar in design to microwave FSSs, which may not be the case due to the nature of manufacturing nanoscale materials. Additionally, due to these manufacturing difficulties, optical FSSs may be too expensive to produce for SHM purposes.

APPENDIX

MATLAB CODE FOR EMBEDDED FSS FREQUENCY RESPONSE CALCULATION

 (File names denoted in bold)

<u>Stackup_Response_Simulator.m (Main Function)</u>

```matlab
close all;
clear classes;
clc;

% This is a script to solve for the S-parameters of an arbitrary
dielectric
% stackup which includes the presence of Frequency Selective Surfaces
and
% ground planes. This script was written by Dustin Pieper, with
equations
% and knowledge developed both from general theory as well as a the
% following papers:


% Simulator Parameters

startFreq=1*10^9;    %Start frequency (Hz)
stopFreq=10*10^9;     %Stop frequency (Hz)
numPoints=2001;      %Number of frequency points
bckEr=1;             %Background relative dielectric constant
bckMr=1;             %Background permeability;
gnd=0;               %Set to 1 to simulate ground plane at bottom layer
(currently un-implemented. Keep at 0)
angle=0;             %Incident Angle (currently un-implemented. Keep at
0)


%Define Layers
%Define each layer according to the following templates. Layers can be
%either material layers or FSS layers.
%Template:
%   Material: sheet(layer,'Mat',thickness,dielectric
constant,permeability,null (set to 0),null);
%   FSS:      sheet(layer,'FSS',type,p1,p2,p3,p4);
%             p1-p4 are dependant on the FSS element type.
%             For the 'Square Loop' type FSS, p1=conductors width (m),
p2=gap
%             width (m), p3=conductor length (m), and p4=element edge
%             length (m)
%Each layer must be numbered in order
%from 1 to the number of layers. All layers after the first layer must
%include "l" at the end of the sheet function. An example is provided
below
%of a stackup.

%%%%%%%%%%%%%%%%%%%%%%
```

```
%EXAMPLE STACKUP:
% l(1)=sheet(1,'Mat',1*2.54*10^-3,4,1,0,0);
% l(2)=sheet(2,'Mat',2.54*10^-3,3.3-1i*0.0132,1,0,0,l);
% l(3)=sheet(3,'FSS','Square_Loop',3*10^-3,4*10^-3,14.5*10^-3,18.5*10^-
3,l);
% l(4)=sheet(4,'Mat',3*10^-3,1,1,0,0,l);
% l(5)=sheet(5,'Mat',1*2.54*10^-3,3.3,1,0,0,l);
%%%%%%%%%%%%%%%%%%%%%%%%

l(1)=sheet(1,'Mat',1*2.54*10^-3,4,1,0,0);
l(2)=sheet(2,'Mat',2.54*10^-3,3.3-1i*0.0132,1,0,0,l);
l(3)=sheet(3,'FSS','Square_Loop',3*10^-3,4*10^-3,14.5*10^-3,18.5*10^-
3,l);
l(4)=sheet(4,'Mat',3*10^-3,1,1,0,0,l);
l(5)=sheet(5,'Mat',1*2.54*10^-3,3.3,1,0,0,l);

%Run simulation
stack=stackup(startFreq,stopFreq,numPoints,bckEr,bckMr,angle,gnd,l);
```

stackup.m (Class definition. Must be in separate folder with same name as class)

```
classdef stackup
    % This class defines a material stackup with
    % dimensions and emag properties of all layers.
    % Using these, the transmission and reflection responses of the
    % structure are found using ABCD parameters

    properties (Constant)
        res=10^-5;
        c=3*10^8;
    end

    properties
        layers
        x
        xer
        xmr
        gnd
        Zin
        ref
        trans
        angle
        bckgnder
        bckgndmr
        bckgndimp
        freq
    end
    methods
        function
obj=stackup(minfreq,maxfreq,points,bckgnder,bckgndmr,angle,gnd,mats)
            %Loads in parameters
            obj.freq=minfreq:(maxfreq-minfreq)/points:maxfreq;
            obj.bckgnder=bckgnder;
            obj.bckgndmr=bckgndmr;
            obj.angle=angle;
            obj.bckgndimp=377*sqrt(bckgndmr/bckgnder);
```

```matlab
                obj.gnd=gnd;
                obj.layers=length(mats);
                for n=1:obj.layers
                      if n==1
                          mats(n).minloc=0;
                      else
                          mats(n).minloc=mats(n).Prev.maxloc;
                      end
                      mats(n).maxloc=mats(n).minloc+mats(n).thickness;
                      if strcmp('Mat', mats(n).type)
                      obj.x=[obj.x mats(n).minloc:obj.res:mats(n).maxloc];
                      obj.xer=[obj.xer
mats(n).er.*ones(1,mats(n).thickness/obj.res)];
                          obj.xmr=[obj.xmr
mats(n).mr.*ones(1,mats(n).thickness/obj.res)];
                      end
                end
                %Calculates ABCD Parameters of structure
                for n=obj.layers:-1:1;
                      %Finds input impedance of last layer
                      if n==obj.layers
                          if ~obj.gnd
                              %Calculate ABCD Paramaters for FSS layer
                              if strcmp('FSS', mats(n).type)

mats(n).impedance=sheet.Z(mats(n).layer,mats(n).element,mats,obj.freq,m
ats(n).s,mats(n).g,mats(n).d,mats(n).p);
                              end

obj.Zin=mats(n).impedance.*(obj.bckgndimp+1i*mats(n).impedance.*...

tan(2*pi.*obj.freq.*sqrt(mats(n).er*mats(n).mr)*mats(n).thickness./obj.
c))./...

(mats(n).impedance+1i*obj.bckgndimp.*tan(2*pi.*obj.freq.*sqrt(mats(n).e
r*mats(n).mr)*mats(n).thickness./obj.c));

obj.Zin=mats(n).impedance.*obj.bckgndimp./(mats(n).impedance+obj.bckgnd
imp);

trans_matrix_A=[cos(2*pi.*obj.freq.*sqrt(mats(n).er*mats(n).mr)*mats(n)
.thickness./obj.c)];

trans_matrix_B=[1i*mats(n).impedance.*sin(2*pi.*obj.freq.*sqrt(mats(n).
er*mats(n).mr)*mats(n).thickness./obj.c)];

trans_matrix_C=[1i./(mats(n).impedance).*sin(2*pi.*obj.freq.*sqrt(mats(
n).er*mats(n).mr)*mats(n).thickness./obj.c)];

trans_matrix_D=[cos(2*pi.*obj.freq.*sqrt(mats(n).er*mats(n).mr)*mats(n)
.thickness./obj.c)];
                              A=trans_matrix_A; B=trans_matrix_B;
C=trans_matrix_C; D=trans_matrix_D;
                          elseif obj.gnd
                              if strcmp('FSS', mats(n).type)
```

```matlab
mats(n).impedance=sheet.Z(mats(n).layer,mats(n).element,mats,obj.freq,m
ats(n).s,mats(n).g,mats(n).d,mats(n).p);
                        end

obj.Zin=1i*mats(n).impedance.*tan(2*pi.*obj.freq.*sqrt(mats(n).er*mats(
n).mr)*mats(n).thickness./obj.c);
                    end
            %Finds input impedance of all other layers layer
            else
                    %Calculate ABCD Paramaters for FSS layer
                    if strcmp('FSS', mats(n).type)

mats(n).impedance=sheet.Z(mats(n).layer,mats(n).element,mats,obj.freq,m
ats(n).s,mats(n).g,mats(n).d,mats(n).p);

obj.Zin=mats(n).impedance.*obj.Zin./(mats(n).impedance+obj.Zin);
                            trans_matrix_A=[1]; trans_matrix_B=[0];
trans_matrix_C=[-1i./mats(n).impedance]; trans_matrix_D=[1];
                            An=A.*trans_matrix_A+B.*trans_matrix_C;
Bn=A.*trans_matrix_B+B.*trans_matrix_D;
                            Cn=C.*trans_matrix_A+D.*trans_matrix_C;
Dn=C.*trans_matrix_B+D.*trans_matrix_D;
                            A=An; B=Bn; C=Cn; D=Dn;
                    end
                    %Calculate ABCD Paramaters for Mat layer
                    if strcmp('Mat', mats(n).type)

trans_matrix_A=[cos(2*pi.*obj.freq.*sqrt(mats(n).er*mats(n).mr)*mats(n)
.thickness./obj.c)];

trans_matrix_B=[1i*mats(n).impedance.*sin(2*pi.*obj.freq.*sqrt(mats(n).
er*mats(n).mr)*mats(n).thickness./obj.c)];

trans_matrix_C=[1i./(mats(n).impedance).*sin(2*pi.*obj.freq.*sqrt(mats(
n).er*mats(n).mr)*mats(n).thickness./obj.c)];

trans_matrix_D=[cos(2*pi.*obj.freq.*sqrt(mats(n).er*mats(n).mr)*mats(n)
.thickness./obj.c)];
                            An=A.*trans_matrix_A+C.*trans_matrix_B;
Bn=B.*trans_matrix_A+D.*trans_matrix_B;
                            Cn=A.*trans_matrix_C+C.*trans_matrix_D;
Dn=B.*trans_matrix_C+D.*trans_matrix_D;
                            A=An; B=Bn; C=Cn; D=Dn;
                        end
                end

            %Calculate overall structure reflection/transmission
response
            obj.ref=20*log10((A*obj.bckgndimp+B-C*obj.bckgndimp^2-
D*obj.bckgndimp)./(A*obj.bckgndimp+B+C*obj.bckgndimp^2+D*obj.bckgndimp)
);

obj.trans=20*log10(2*(obj.bckgndimp)./(A*obj.bckgndimp+B+C*obj.bckgndim
p^2+D*obj.bckgndimp));
```

```
            end

            %Plot Frequency Responses
            figure()
            plot(obj.freq,obj.ref,'r-')
            ylim([-60,0])
            xlim([min(obj.freq), max(obj.freq)])
            title('Reflection')
            figure()
            plot(obj.freq,obj.trans)
            ylim([-60,0])
            xlim([min(obj.freq), max(obj.freq)])
            title('Transmission')
        end

    end
end
```

sheet.m (Class definition. Must be in separate folder with same name as class)

```
classdef sheet < dlnode
    % This class defines an FSS layer with its
    % type,dimensions, and emag properties

    properties
        layer
%Position in stackup (input)
        type                                          %FSS
element type (input)
        element
        loc
        ereff
%Effective Permittivity (calculated from function)
        mreff
%Effective Permeability (calculated from function)
        thickness                                     %Thickness of layer
        minloc                                         %Bottom geometrical
location
        maxloc                                        %Top geometrical
location
        er                                             %Permittivity
        mr                                             %Permeability
        angle
%Angle of Incidence (unused)
        lambda
%Wavelength (output)
        impedance
%Impedance of FSS (output)
        x
        s
        g
        d
        p
        X1
```

```matlab
            B1
            c=3*10^8
        end

    methods
        function obj=sheet(layer,type,p1,p2,p3,p4,p5,l)
            obj=obj@dlnode(layer);
            obj.layer=layer;
            obj.type=type;
            switch type
                case 'FSS'
                obj.element=p1;
                obj.thickness=0;
                switch obj.element
                    %Define FSS element parameters here
                    case 'Square_Loop'
                    obj.s=p2;
                    obj.g=p3;
                    obj.d=p4;
                    obj.p=p5;
                end
                case 'Mat'
                obj.thickness=p1;
                obj.er=p2;
                obj.mr=p3;
                obj.impedance=377*sqrt(obj.mr/obj.er);
            end
                if layer>1
                obj.insertAfter(l(obj.layer-1))
                end
        end
    end
    methods(Static)
        function imp=Z(layer,element,l,f,s,g,d,p)
            switch element
                %Define FSS element impedance calculations here
                case 'Square_Loop'
                l(layer).ereff=Ereff_F('Strips', layer, l, s, g );
                l(layer).lambda=3*10^8./(f)./sqrt((l(layer).ereff));
                l(layer).X1=d/p*kern_F(p, 2*s, l(layer).lambda, 0);
                l(layer).B1=4*d/p*kern_F(p, g, l(layer).lambda, 0);
                imp=(377)*(1j.*l(layer).X1+1./(1j.*l(layer).B1));
                otherwise
                    imp=l(layer).impedance;
            end
        end
    end
end
```

dlnode.m (Class definition. Must be in separate folder with same name as class.

Provided by Matlab for object oriented program usage)

```matlab
classdef dlnode < handle
 % dlnode A class to represent a doubly-linked list node.
 % Link multiple dlnode objects together to create linked lists.
```

```matlab
properties
Data
end
properties(SetAccess = private)
Next = dlnode.empty;
Prev = dlnode.empty;
end

methods
function node = dlnode(Data)
% Construct a dlnode object.
if nargin > 0
node.Data = Data;
end
end

function insertAfter(newNode, nodeBefore)
% Insert newNode after nodeBefore.
removeNode(newNode);
newNode.Next = nodeBefore.Next;
newNode.Prev = nodeBefore;
if ~isempty(nodeBefore.Next)
nodeBefore.Next.Prev = newNode;
end
nodeBefore.Next = newNode;
end

function insertBefore(newNode, nodeAfter)
% Insert newNode before nodeAfter.
removeNode(newNode);
newNode.Next = nodeAfter;
newNode.Prev = nodeAfter.Prev;
if ~isempty(nodeAfter.Prev)
nodeAfter.Prev.Next = newNode;
end
nodeAfter.Prev = newNode;
end

function removeNode(node)

% Remove a node from a linked list.
if ~isscalar(node)
error('Input must be scalar')
end
prevNode = node.Prev;
nextNode = node.Next;
if ~isempty(prevNode)
prevNode.Next = nextNode;
end
if ~isempty(nextNode)
nextNode.Prev = prevNode;
end
node.Next = dlnode.empty;
node.Prev = dlnode.empty;
end
```

```matlab
function clearList(node)
% Clear the list before
% clearing list variable
prev = node.Prev;
next = node.Next;
removeNode(node)
while ~isempty(next)
node = next;
next = node.Next;
removeNode(node);
end
while ~isempty(prev)
node = prev;
prev = node.Prev;
removeNode(node)
end
end
end % methods

methods (Access = private)
function delete(node)
% Delete all nodes
clearList(node)
end
end % private methods
end % classdef
```

Ereff_F.m (function)

```matlab
function [ F ] = Ereff_F( type, Layer, l, s, g )

%Calculates effective dielectric constant using conformal maps for
different conductor
%configurations. Currently works with Coplanar Strips ('Strips') and
%Coplanar Waveguides ('WG'). New conformal maps can be added as
different
%cases in the following switch case statement.
switch type
% if strcmp(type, 'Strips')
    case 'Strips'
   g=g/2;
   k0=sqrt(1-(g/(s+g))^2);
   kp0=sqrt(1-k0^2);

   h=0;
   ka=[];
   kpa=[];
   era=[];

   for n=Layer:-1:1
       if strcmp(l(n).type, 'Mat')
          h=h+l(n).thickness;
          k=sqrt(1-
((sinh(pi*g/(2*sum(h))))^2/(sinh(pi*(s+g)/(2*sum(h))))^2));
          ka=[ka, k];
```

```matlab
            kpa=[kpa, sqrt(1-k.^2)];
            era=[era, l(n).er];
        end
    end

    h=0;
    kb=[];
    kpb=[];
    erb=[];

    for n=Layer:1:length(l)
        if strcmp(l(n).type, 'Mat')
            h=h+l(n).thickness;
            k=sqrt(1-
((sinh(pi*g/(2*sum(h))))^2/(sinh(pi*(s+g)/(2*sum(h))))^2));
            kb=[kb, k];
            kpb=[kpb, sqrt(1-k.^2)];
            erb=[erb,l(n).er];
        end
    end

    qa=ellipke(kpa)*ellipke(k0)./(ellipke(ka)*ellipke(kp0));
    qb=ellipke(kpb)*ellipke(k0)./(ellipke(kb)*ellipke(kp0));

    Ereffa=1;
    for n=1:1:length(qa)
        if n<length(qa)
            Ereffa=Ereffa+qa(n)*(era(n)-era(n+1));
        end
        if n==length(qa)
            Ereffa=Ereffa+qa(n)*(era(n)-1);
        end
    end
    Ereffb=1;
    for n=1:1:length(qb)
        if n<length(qb)
            Ereffb=Ereffb+qb(n)*(erb(n)-erb(n+1));
        end
        if n==length(qb)
            Ereffb=Ereffb+qb(n)*(erb(n)-1);
        end
    end
    F=(Ereffa+Ereffb)/2;

% elseif strcmp(type, 'WG')
    case 'WG'
    s=s/2;
    k0=s/(s+g);
    kp0=sqrt(1-k0^2);
    h=0;
    ka=[];
    kpa=[];
    era=[];

    for n=Layer:-1:1
        if strcmp(l(n).type, 'Mat')
```

```matlab
        h=h+l(n).thickness;
        k=sinh(pi*s/(2*sum(h)))/sinh(pi*(s+g)/(2*sum(h)));
        ka=[ka, k];
        kpa=[kpa, sqrt(1-ka.^2)];
        era=[era, l(n).er];
    end
end
era=[era,1];

h=0;
kb=[];
kpb=[];
erb=[];

for n=Layer:1:length(l)
    if strcmp(l(n).type, 'Mat')
      h=h+l(n).thickness;
      k=sinh(pi*s/(2*sum(h)))/sinh(pi*(s+g)/(2*sum(h)));
      kb=[kb, k];
      kpb=[kpb, sqrt(1-ka.^2)];
      erb=[erb,l(n).er];
    end
end
erb=[erb,1];

qa=ellipke(ka).*ellipke(kp0)./(ellipke(kpa).*ellipke(k0));
qb=ellipke(kb).*ellipke(kp0)./(ellipke(kpb).*ellipke(k0));

Ereff=1;
for n=length(qa):-1:0
    Ereff=Ereff+qa(n)*(era(n)-era(n-1));
end
for n=length(qb):-1:0
    Ereff=Ereff+qb(n)*(erb(n)-erb(n-1));
end
F=Ereff;

end

end
```

BIBLIOGRAPHY

[1]   B. Munk, "Frequency Selective Surfaces: Theory and Design," John Wiley and Sons Inc.,   2000.

[2]   B. Munk, R. Kouyoumjian, L. Peters, "Reflection Properties of Periodic Surfaces of Loaded Dipoles", IEEE Trans. on Antennas and Prop., vol. 19, no. 5, Sept. 1971.

[3]   E.A. Parker, "The Gentleman's Guide to Frequency Selective Surfaces", Q.M.W. Antenna Symposium, London, U.K., Apr. 1991.

[4]   S.M.A. Hamdy, E.A. Parker, "Current Distribution on the Elements of a Square Loop Frequency Selective Surface", Electron. Lett., Vol. 18, no. 14, 1982.

[5]   A.K. Rashid, B. Li, Z. Shen, "An Overview of Three-Dimensional Frequency-Selective Structures." IEEE Antennas and Prop. Magazine, Vol. 56, Iss. 3, June 2014, pp. 43-67.

[6]   T.K. Chang, R.J. Langley, E.A. Parker, "Active Frequency-Selective Surfaces," IEE Proceedings, Microwaves, Antennas, and Propagation, Vol. 143, Iss. 1, Feb. 1996.

[7]   F. Costa, A. Monorchio, G. Manara, "Analysis and Design of Ultra Thin Electromagnetic Absorbers Comprising Resistively Loaded High Impedance Surfaces," IEEE Trans. on Antennas and Prop., Vol. 58, Iss. 5, Mar. 2010, pp. 1551-1558.

[8]   J. Romeu, Y. Rahmat-Samii, "Fractal FSS: A Novel Dual-Band Frequency Selective Surface," IEEE Trans. on Antennas and Prop., Vol. 48, Iss. 7, Jul. 2000, pp. 1097-1105.

[9]   R. Mittra, C. Chan, T. Cwik, "Techniques for Analyzing Frequency Selective Surfaces-A Review," IEEE Procedings, Vol. 76, Iss. 12, Dec. 1988, pp. 1593-1615.

[10]   P. Harms, R. Mittra, W. Ko, "Implementation of the Periodic Boundary Condition in the Finite-Difference Time-Domian Algorithm for FSS Structures," IEEE Trans. on Antennas and Prop., Vol. 42, Iss. 9, Sept. 1994, pp. 1317-1324.

[11]   I. Bardi, R. Remski, D. Perry, Z. Cendes, "Plane Wave Scattering from Frequency Selective Surfaces by the Finite-Element Method," IEEE Trans. on Mag., Vol.38, Iss. 2, Mar. 2002, pp. 641-644.

[12]   R.B. Kieburtz, A. Ishimaru, "Scattering by a Periodically Apertured Screen," Trans. on Antennas and Prop., Vol. 9, Iss. 6, Nov. 1961, pp. 506-514.

[13]   R.J. Langley, A.J. Drinkwater, "Improved Empirical Model for the Jerusalem Cross," IEE Proc. H on Micro., Optics, and Ant., Vol. 129, Iss. 1, Feb. 1982, pp. 1-6.

[14]   N. Marcuvitz, "Waveguide Handbook," McGraw-Hill, New York, 1951.

[15]   I. Anderson, "On the Theory of Self-Resonant Grids," The Bell System Technical Journal, Vol. 54, Iss. 10, Dec. 1975, pp. 1725-1731.

[16]   R.J. Langley, E.A. Parker, "Equivalent Circuit Model for Arrays of Square Loops," Electron. Lett., Vol. 18, no. 7, 1982.

[17]   R.J. Langley, E.A. Parker, "Double-Square Frequency Selective Surfaces and their Equivalent Circuit," Electron. Lett., Vol. 19, no. 17, 1983.

[18]   D. Singh, A. Kumar, S. Meena, V. Agarwala, "Analysis of Frequency Selective Surfaces for Radar Absorbing Materials," Prog. in Electromagnetics Research, Vol. 38, 2012, pp. 297-314.

[19]   P. Callaghan, E.A. Parker, and R.J. Langley, "Influence of Supporting Dielectric Layers on the Transmission Properties of Frequency Selective Surfaces," Microwave, Antennas, and Prop. IEEE Proceedings H, Vol 138, no. 5, Oct. 1991, pp. 448-454.

[20]   F. Costa, A. Monorchio, G. Manara, "Efficient Analysis of Frequency-Selective Surfaces by a Simple Equivalent-Circuit Model," IEEE Ant. and Prop. Magazine, Vol. 54, No. 4, Aug. 2012, pp. 35-48,

[21]   T.K. Wu, "Frequency Selective Surface and Grid Array," John Wiley and Sons Inc., 1995.

[22]   C.K. Lee, R.J. Langley, C. Eng, "Equivalent-Circuit Models for Frequency-Selective Surfaces at Oblique Angles of Incidence," IEE Proc., Vol. 132, No. 6, Oct. 1985, pp. 395-399.

[23]   ANSYS HFSS, http://www.ansys.com/, accessed Mar. 2015.

[24]   Z. Sipus, M. Bosiljevac, "Efficient Analysis of Curved Frequency Selective Surfaces," 3rd European Conf. on Ant. and Prop. 2009, Berlin, Germany, Mar. 2009, pp. 2726-2730.

[25]   B. Philips, E.A. Parker, R.J. Langley, "Finite Curved Frequency Selective Surface," Electron. Lett., Vol. 29, no. 10, May 1993, pp. 882-883.

[26]   T. Cwik, R. Mittra, "The Effects of the Truncation and Curvature of Periodic Surfaces: A Strip Grating," IEEE Trans. on Antennas and Prop., Vol. 36, Iss. 5, May 1988, pp. 612-622.

[27]   S.B. Savia, E.A. Parker, B. Philips, "Finite Planar and Curved-Ring-Element Frequency Selective Surfaces," Microwave, Antennas, and Prop. IEEE Proceedings, Vol. 146, No. 6, Dec. 1999, pp. 401-406.

[28]   F. Costa, A. Monorchio, G. Manara, "An Equivalent-Circuit Modeling of High Impedance Surfaces Employing Arbitrarily Shaped FSS," Electromagnetics in Advanced Applications 2009, Torino, IT, Sept. 2009, pp. 852-855.

[29]   M.W.B. Silva, L. C. Kretly, S. Barbin, "Practical Guidelines for the Design and Implementation of Microwave Absorber Using FSS-Frequency Selective Surfaces," 2014 International Conference of Microwaves, Radar, and Wireless Communications, Gdansk, PM, June 2014.

[30]   R. Hall, R. Mittra, K. Mitzner, "Analysis of Multilayered Periodic Structures Using Generalized Scattering Matrix Theory," IEEE Trans. on Antennas and Prop., Vol. 36, Iss. 4, April 1988, pp. 511-517.

[31]   B.J. Arritt, A.F. Starr, D.R. Smith, "Electromagnetic Performance of Mechanically Loaded Composite Metamaterials," International Conference on Composite Materials (ICCM) 17, July 2009.

[32]   B. Arritt, B. Adomanis, T. Khraishi, D. Smitt, "Parametric Analysis of the Strain-Dependant Behavior of a Metamaterial Electric Resonantor," App. Physics Letters, Vol. 97, Iss. 19, 2010.

[33]   R. Melik, E. Unal, N.K. Perkgoz, C. Puttlitz, H.V. Demir, "Flexible Metamaterials for Wireless Strain Sensing," App. Physics Letters, Vol. 95, Iss. 18, 2009.

[34]   S.D. Jang, B.W. Kang, J. Kim, "Frequency Selective Surface Based Passive Wireless Sensor for Structural Health Monitoring," Smart Materials and Structures, Vol. 22, No. 2, 2013.

[35]   E. Kinzel, K. Donnell, K. Chandrashekhara, "Structural Health Monitoring and Remote Sensing of Transportation Infrastructure Using Embedded Frequency Selective Surfaces," Missouri S&T, Rolla, MO, Tech. Rep. NUTC R365, Jul. 2014.

[36]   E. Kinzel, "Design of a Frequency-Selective Surface Strain Sensor," IEEE APS, Memphis, TN, July 2014, pp. 2074-2075.

[37]   C. Farra, K. Worden, "An Introduction to Structural Health Monitoring," Phil. Trans. Soc. A, Vol. 365, Dec. 2006, pp. 303-315.

[38]   O. Abdelkarim, A. Gheni, S. Anumolu, S. Wang, M. ElGawady, "Hollow-Core FRP-Concrete-Steel Bridge Columns under Extreme Loading," Missouri S&T, Rolla, MO. Tech. Rep. cmr 15-008, Jan. 2015.

[39]   D.W.A. Rees, "Basic Engineering Plasticity: An Introduction with Engineering and Manufacturing Applications", Elsevier Ltd., 2006.

[40]   A. Foudazi, K.M. Donnell, M.T. Ghasr, "Application of Active Microwave Thermography to Delamination Detection," Proceedings of the International Instrumentation and Measurement Technology Conference (I2MTC), Montevideo, Uruguay, pp. 1567-1571, May 2014.

[41]   K.M. Donnell, R. Zoughi, "Application of Embedded Dual-Loaded Modulated Scatterer Technique (MST) to Multilayer Structures," Inst. and Meas, IEEE Trans,Vol. 61, no. 10, pp. 2799-2806, Oct. 2012.

[42]   Martin Barth, Frank Schubert, and Bernd Koehler, "Where X-ray imaging fails – delamination, crack, and micro-pore detection using ultrasonic reflection tomography in a scanning acoustic microscope," Nuclear Science Symposium (NSS), Dresden, Germany, pp. 577-581, Oct. 2008.

[43]   Mary J. Mathews, "Study of Delamination in Fiber Reinforced Composite Laminates," Ph.D Dissertation, Dept. of Mech. Eng., Univ. of Utah, Salt Lake City, UT, Dec. 2007.

[44]   Masataka Ohira, Hiroyuki Deguchi, Mikio Tsuji, Hiroshi Shigesawa, "Analysis of Frequency Selective Surfaces with Arbitrarily Shaped Element by Equivalent Circuit Model," Electronics and Communications in Japan, Part 2, Vol. 88, No. 6, pp. 9-17, 2005.

[45]   Mathworks MATLAB, http://www.mathworks.com, accessed Dec. 2015.

[46]   F. Costa, A. Monorchio, G. Manara, "An Equivalent Circuit Model of Frequency Selective Surfaces Embedded within Dielectric Layers," Ant. and Prop. Society Int. Symposium, Charleston, SC, pp. 1-4, June 2009.

[47]   E. Chen, S. Chou, "Characteristics of Coplanar Transmission Lines on Multilayer Substrates: Modeling and Experiments," IEEE Trans. on Microwave Theory and Tech., vol. 45, no. 6, pp. 939–945, June 1997.

[48]   Dean A. Frickey, "Conversions Between S, Z, Y, h, ABCD, and T Parameters which are Valid for Complex Source and Load Impedances," IEEE Trans. on Microwave Theory and Tech, vol. 42, no. 2, pp. 205-221, Feb. 1994.

[49]   Roland Schinzinger, Patricio A. A. Laura, "Conformal Mapping: Methods and Applications," Dover Publications Inc, Mineola, New York, 1991.

[50]   Fei Cheng, Jie Gao, Ting S. Luk, Xiaodong Yang, "Structural Color Printing Based on Plasmonic Metasurfaces of Perfect Light Absorption," Scientific Reports, vol. 5, June 2015.

[51]   Shih-Chi Liu, Masayoshi Tomizuka, Galip Ulsoy, "Strategic Issues in Sensors and Smart Structures," Struct. Control Health Monit., Vol. 13, Nov. 2006, pp. 946-957.

[52]   D. Uttamchandani, "Fibre-optic sensors and Smart Structures: Developments and Prospects," Elect. and Comm. Eng. Journal, Oct. 1994, pp. 237-246.

[53]   D. Pieper, K. Donnell, "Approximation of Effective Dielectric Constant for FSS in Layered Dielectrics using Conformal Mapping," 2015 Internation Symp. on Ant. and Prop. & USNC/URSI Nat. Radio Science Meeting, Vancouver, BC, July 2015, pp. 991-992.

[54]   D. Pieper, K. Donnell, "Application of Frequency Selective Surfaces for Inspection of Layered Structures," 2015 IEEE International Instrum. and Meas. Tech. Conf. (I2MTC), Pisa, IT, May 2015, pp. 1204-1209.

[55]   Wai Lee Ko, Raj Mittra, "Implementation of Floquet Boundary Condition in FDTD for FSS Analysis," Ant. and Prop. Society Intern. Symposium, 1993, Ann Arbor, MI, USA, June 1993, pp. 14-17, Vol. 1.

VITA

Dustin Franklin George Pieper was born in St. Charles, MO on May 17, 1991, and lived in Troy, MO throughout his childhood. After graduating from Troy Buchanan High School, he attended the Missouri University of Science and Technology in 2009, where he received a B.S. in Electrical Engineering in 2013. He subsequently started his master's program, also at Missouri S&T, focusing in Electromagnetics at the Applied Microwave Non-destructive Testing Lab (*amntl*), graduating with his M.S. in Electrical Engineering in May 2016.

While at the *amntl*, Dustin studied the use of Frequency Selective Surfaces for Structural Health Monitoring purposes. During this time, he also worked as a lab tutor for the Electronics 1 lab course. In addition, throughout his education, Dustin participated in a number of internships, including work at Sandia National Labs and T.E. Connectivity. Dustin is currently working as a radar engineer with Defense contractor Dynetics in Huntsville, AL.